



Evaluation of Residual Stresses by Microscale FIB-DIC Ring-Core Milling and Other Techniques for Beam Dump Application at CERN

Master's Thesis

Francesco Fagnoni

ffagno17@student.aau.dk

Department of Materials and Production Engineering
Master's in Materials Technology
Aalborg University

Supervisors:

Mikael Larsen, Aalborg University
Ana Teresa Perez Fontenla, CERN EN-MME
Josep Busom Descarrega, CERN EN-MME

June 2, 2019

Acknowledgements

This Master's thesis would not have been possible without the help of many people involved in it. I'm extremely grateful for the first class guidance and support received during the project, that made possible to achieve the presented results in the allotted time-frame.

In particular, I'd like to express my most sincere gratitude to:

Alexander Lunt, for proposing the FIB-DIC approach to the group and the specific guidance provided in both FIB operation and DIC processing;

Edmundo Lopez Sola, for providing the BDF prototypes used and support with the FEM simulations;

Oscar Sacristan De Frutos, for providing the aluminum sample used and the support with macroscopic blind-hole drilling;

Elisa Garcia-Tabares Valdivieso and **Adrienn Baris** for the support with FIB operation;

Ana Teresa Perez Fontenla, as head of the Microscopy Team at CERN-MME, for the general supervision of the project and specific support with EBSD analysis;

Josep Busom Descarrega, for being my main reference during the project, for the outstanding support received, and for the specific support with XRD analysis.

Further, I'd like to express a special thank to **Raino Mikael Larsen**, for having accepted the not-easy task supervising a student abroad, and to **Jens Christian Moesgaard Rauhe** as Head of the Study Board at Aalborg University for approving the presented Master's thesis project.

Finally I would like to acknowledge **Marco Calviani** as head of Sources, Targets & Interactions (STI) group at CERN for seeing the importance of in depth residual stresses evaluation within the Beam Dump Facility (BDF) project.

Abstract

In the framework of the CERN R&D activities for the Beam Dump Facility (BDF), different target prototypes were fabricated. They are cylinders made of refractory metals, clad with a tantalum layer by means of Hot Isostatic Pressing (HIP).

High residual stresses resulting from the HIP cycle are expected and its assessment is indispensable to validate the targets thermo-mechanical simulations. Techniques such as hole drilling, X-ray diffraction and microscale Focused Ion Beam (FIB) ring-core milling followed by Digital Image Correlation (DIC) analysis were employed to determine and understand the residual stress distribution in those parts.

The presented Master's thesis has been developed at CERN Engineering department (EN), in the Materials and Metrology group (MME) under the direct supervision of Josep Busom Descarrega (CERN) Ana Teresa Pérez Fontenla (CERN) and Raino Mikael Larsen (Aalborg University).

Contents

Acknowledgements	iii
Abstract	v
1 Introduction	1
1.1 Context	2
1.1.1 CERN	2
1.1.2 EN-MME Group	4
1.1.3 Search for Hidden Particles (SHiP) project	4
1.1.4 Beam Dump Facility (BDF) target design	6
1.1.5 Hot Isostatic Presssing (HIP) process	10
1.2 Residual stresses	11
1.2.1 Shot penning induced residual stresses	13
1.2.2 Thermal stresses	13
1.2.3 Machining residual stresses	14
1.3 Residual stresses measurement techniques	15
1.3.1 Hole-drilling strain-gauge method	15
1.3.2 X-Ray diffraction	16
1.3.3 FIB-DIC ring core analysis	17
1.4 Goals of the project	18
1.4.1 Assessment of residual stresses in BDF (as with ISIS)	19
1.4.2 Validation of FIB-assisted ring-drilling residual stresses evaluation as standard analysis technique	20
2 Methodology	21
2.1 Hole-drilling strain-gage methodology	21
2.2 X-Ray Diffraction (XRD) Methodology	23
2.3 FIB-DIC ring-core analysis	28

2.3.1	Patterning and surface decoration	29
2.3.2	SEM imaging optimization	30
2.3.3	Milling procedure	31
2.3.4	Digital Image Correlation (DIC)	33
2.3.5	Data analysis	36
3	Residual stresses in shot-penned aluminum sample	41
3.1	Prototype description	41
3.1.1	Material properties	41
3.1.2	Sample extraction and workplan	42
3.2	Residual stresses analysis	44
3.2.1	Macroscopic hole drilling	44
3.2.2	XRD analysis	44
3.2.3	FIB-DIC analysis	47
3.3	Discussion	49
4	Residual stresses analysis in BDF prototypes	51
4.1	Prototype description	51
4.1.1	Materials properties	52
4.1.2	Production process (HIP)	56
4.1.3	Sample extraction and workplan	59
4.1.4	Mechanical and chemical polishing	59
4.2	Residual stresses analysis	62
4.2.1	Preliminary FEM simulations	62
4.2.2	Macroscopic hole drilling	66
4.2.3	XRD	66
4.2.4	FIB-DIC analysis	71
4.3	Discussion	75
4.3.1	Residual stresses induced by sample preparation	76
4.3.2	Residual stresses due to turning operation after HIP	76
4.3.3	Incomplete annealing during HIP	77
4.3.4	Artifact due to the crystal orientation	77

CONTENTS	ix
5 Conclusions	81
Bibliography	83
A Used acronyms	A-1
B Notes on thermo-mecanical stresses in BDF	B-1
C FIB-DIC operator's manual	C-1
C.0.1 Milling	C-1
C.0.2 DIC	C-2
D Hardness measuremetns of Al, Ta and Ta2.5W materials	D-1
E BDF targhet prototypes technical drawings	E-1

Introduction

With the goal of expanding the range of sub-atomic particles and interactions observable at the European Laboratory for Particle Physics (CERN), a new Beam Dump Facility (BDF) is in the design phase.

A beam dump consists of a fixed target aimed at absorbing the majority of incident protons and containing most of the cascade generated by the beam interaction.

The BDF is intended to be placed at the Super Proton Synchrotron (SPS) particle accelerator. Civil works are expected to start in 2024 and the first Beam On Target (BOT) event is expected in 2027.

The SPS beam is expected to deliver 2.3 MJ of energy¹ to the target every 7.2 seconds. The thermo-mechanical stresses at the beam impact region constitute a major design challenge.

To cope with all the physic and engineering requirements, the current design of the BDF target consist of several co-linear cylinders of refractory metals (molybdenum - Mo - and tungsten - W - based) of 250 mm in diameter and variable thickness, actively cooled by flowing demineralised water.

To protect the target cylinders from the erosion-corrosion phenomena caused by the water cooling, Tantalum (Ta) based cladding was considered.

The clad is 1.5 mm thick and is joined to the core material by means of Hot Isostatic Pressing (HIP) assisted diffusion bonding technique.

The coupling of different materials at joining temperature different from the operation temperature cause residual stresses due to their difference in Coefficient of Thermal Expansion (CTE).

In targets based on similar design, pre-mature failure at the clad level has been observed and attributed to the presence of residual stresses.

The knowledge of residual stresses distribution plays a crucial role in the expected fatigue life during service.

¹Roughly equivalent to the kinetic energy of an average-size car traveling at 130 km/h

Goal of the presented project is the experimental evaluation of residual stresses in the clad material of several BDF target prototypes, representative of the final design.

To evaluate the stress condition in the complete thickness of the clad material, an innovative measurement protocol for the analysis of residual stress distribution on a micron-scale (FIB-DIC methodology) has been employed on cross-sections of the prototypes.

The technique is based on incremental Focused Ion Beam (FIB) milling, combined with high-resolution in situ Scanning Electron Microscopy (SEM) imaging and full field strain analysis by digital image correlation (DIC).

The FIB-DIC method has never been applied before at CERN laboratories. To test and validate the methodology, the technique has been applied to on the cross-section of a shot-peened aluminium sample of known residual stresses profile.

In both alluminum and BDF prototypes the residual stresses obtained applying the FIB-DIC methodology have been compared with the ones obtained by more conventional techniques such as X-Ray Diffraction (XRD) and incremental blind-hole drilling.

The presented master's thesis project has been developed in a collaboration between Aalborg University and CERN under direct supervision of J.B. Descarrega (CERN), A.T. Perez Fontenla (CERN) and Dr. R.M. Larsen (Aalborg University).

1.1 Context

The framework in which the presented work is inserted is covered in the following sections.

1.1.1 CERN

The European Organization for Nuclear Research (CERN) is the largest particle physics research laboratory in the world. CERN is an international institution with 23 member states active since 1954. It covers six square kilometers scattered over 12 sites either side of the Frech-Swiss border near Geneva and runs a network of six accelerators and a decelerators over more than 34 km of tunnels.

At CERN, proton particles generated by stripping the electron from hydrogen particles by an electric field are accelerated at increasingly high energy using a sequence of particle accelerators², as illustrated in figure 1.1:

²In some experiments, Pb ions can also be used

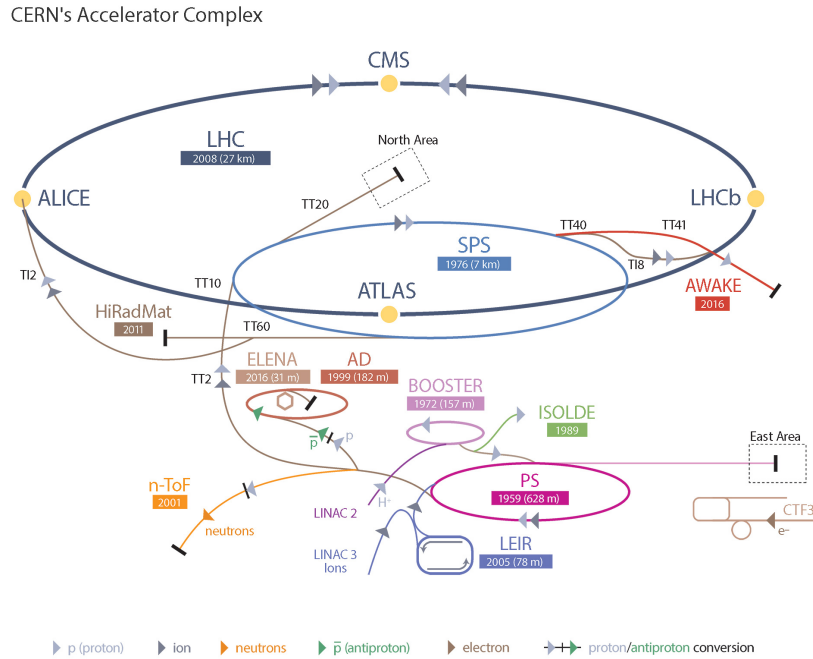


Figure 1.1: Accelerator complex at CERN

- Linac 2, to 50 MeV;
- Synchrotron Booster (PSB), to 1.4 GeV;
- Proton Synchrotron (PS), to 25 GeV;
- Super Proton Synchrotron (SPS), to 450 GeV;
- Large Hadron Collider (LHC), until the final record energy of 6.5 TeV.

Experiment halls are located along all the accelerator complex, to explore the particle interactions obtainable in the full range of energies.

Since its institution, CERN enabled several important achievements in particle physics, contributing to 5 nobel prizes between 1973 and modern days, the most recent of which is the confirmation of the Higgs boson in 2012 which lead to the Nobel Prize in Physics 2013 awarded jointly to François Englert and Peter W. Higgs "for the theoretical discovery of a mechanism that contributes to our understanding of the origin of mass of subatomic particles, and which recently was confirmed through the discovery of the predicted fundamental particle, by the ATLAS and CMS experiments at CERN's Large Hadron Collider." [1].

The presented beam dump facility will produce secondary particles for the Search for Hidden Particles (SHiP) experiment, operational in 2026 in a new SPS

beamline. The primary goal of the SHiP project is to explain the predominance of matter over antimatter in the universe by detecting weakly interacting particles predicted by certain extensions of the Standard Model, a potential Nobel Prize discovery. [2]

1.1.2 EN-MME Group

The CERN institution hosts about 12,000 users per year and 2,500 scientific, technical, and administrative staff members.

The presented project is conducted within the CERN Engineering department (EN), mechanical and materials engineering group (EN-MME) materials and metrology section (EN-MME-MM).

The purpose of the MME group is to provide specific engineering solutions to the CERN community, combining mechanical design, fabrication, and material science. [3]

The section is divided in three teams according to their specific mission:

Metrology - providing dimensional measurements for quality control in precision components;

NDT - with the primary goal of ensuring quality control for components, applying non-destructive techniques such as X-ray tomography, ultrasonic testing, dye penetrant testing and other techniques.

Metallurgy - mainly focused on providing support for characterization of all types of materials concerned by CERN needs, from development to failure analysis applying techniques as metallography, electronical and optical microscopy and mechanical testing are employed.

The presented project is developed within the Metallurgy team.

1.1.3 Search for Hidden Particles (SHiP) project

With the discovery of the Higgs boson, all the predicted constituents of the standard model (SM) have been observed. However, the non-zero neutrino mass, the existence of dark matter (DM), and the baryon asymmetry of the universe (BAU) show that the SM still needs to be extended.

A large number of models Beyond the Standard Model (BSM) have been proposed, some which rely on the presence of "hidden particles" not detected by previous experiments because of their very small couplings (hidden sector in figure 1.2). [4]

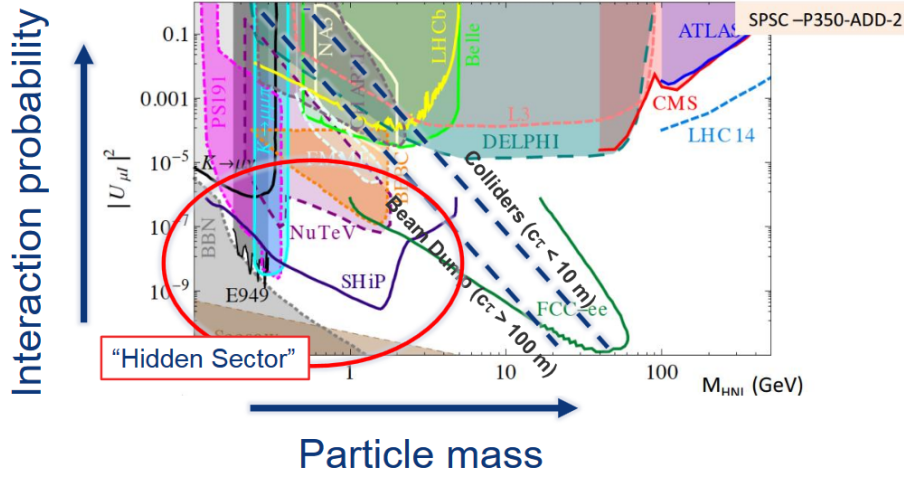


Figure 1.2: Sub-atomic particle and probability maps with highlighted the region achievable with the current accelerators and detector complex and the foreseen improvement of the SHiP project in the "hidden sector" [5].

New data at the low energy, high intensity frontier could be key factor in exploring models with light weakly interacting new physics, and in searching for Majorana neutrinos. [6]

To achieve the SHiP goals, a new general purpose fixed target at the Super Proton Synchrotron (SPS) accelerator is in the designing phase. The target is going to be installed in a new beamline to be constructed in the north area of the SPS, in the Preveessin site (in figure 1.3).

Since many of the hidden particles are result of the heavy hadrons decay, the facility must maximize the hadrons production while minimizing the background.

Electrons, and photons must be stopped, the production of neutrinos from light hadron decays must be minimized, and the detector must be shielded from the residual muon flux. The small coupling implies that the objects are very long-lived compared to the bulk of the unstable Standard Model particles, hence a distant detector with relatively large aperture angles is required to maximise the acceptance.

The SHiP setup is expected to make possible measurements of tau neutrinos with three orders of magnitude more statistics than available than in previous experiments combined [6].

Civil works and excavation of the cavern is scheduled to start in 2024 and the first Beam On Target (BOT) event is expected in 2027.

The total cost of the new fixed-target facility is estimated to be around 150 million CHF (~1 billion DKK), with the target and target complex infrastructure covering 1/3 of the total figure.



Figure 1.3: BDF facility complex [7]

The presented project is considered a part of the Comprehensive Design Phase (CDP) of the Beam Dump Facility (BDF) target component, scheduled to be completed in the second quarter of 2019.

1.1.4 Beam Dump Facility (BDF) target design

In the particle accelerator context, a beam dump is a fixed target designed to absorb the proton bunches circulating inside an accelerator when they are no longer usable for experiments.

A beam can also be directed to a beam dump facility specifically to study the resulting interactions with the target. Detectors at beam dumps allow to study the interactions generated by the full beam impact (in the order of ~ 100.000 million protons per BOT event), as opposed to beam crossing where fewer than 20 collisions are generally expected at every event.

Due to the high deposited energy in high radiation environment, the Beam Dump production target assembly design is one of the most challenging aspects of the BDF.

For the SHiP requirements, the target needs to be designed with a material with the shortest possible nuclear interaction length in order to maximize the production of heavy mesons while minimizing the production of neutrinos.

Therefore, the very high beam power (350 kW on average, with peak power during the spill of 2.56 MW - more data is presented in figure 1.4) has is stopped in a relatively small volume, with consequent generation of high temperatures and high localized thermo-mechanical stresses.

These requirements have been the subject of a detailed conceptual study

Baseline characteristics	
Proton momentum [GeV/c]	400
Beam intensity [p^+ /cycle]	$4.0 \cdot 10^{13}$
Cycle length [s]	7.2
Spill duration [s]	1.0
Beam dilution pattern [-]	Circular
Beam sweep frequency [turns/s]	4
Dilution circle radius [mm]	50
Beam sigma (H,V) [mm]	(8,8)
Average beam power [kW]	356
Average beam power deposited on target [kW]	305
Average beam power during spill [MW]	2.3

Figure 1.4: Baseline beam parameters of the BDF target operation [8]

[9], which has demonstrated that the target is feasible by the combined usage of different materials, target internal cooling channels and beam dilution techniques to keep the heat generated under control [7].

The proposed target design is constituted by 18 collinear cylinders of 250 mm in diameter and variable thickness as illustrated in table 1.5a and in figure 1.5b. The first 13 blocks are constituted by TZM alloy (0.08% titanium - 0.05% zirconium - molybdenum alloy), whereas the subsequent 5 blocks are constituted by pure tungsten (W).

The total length of the target is 130 cm. The target cylinders length and core material was iteratively adjusted to reduce the level of temperatures and stresses reached (figure 1.6a), while keeping the interaction volume to a minimum, as required by the physics application.

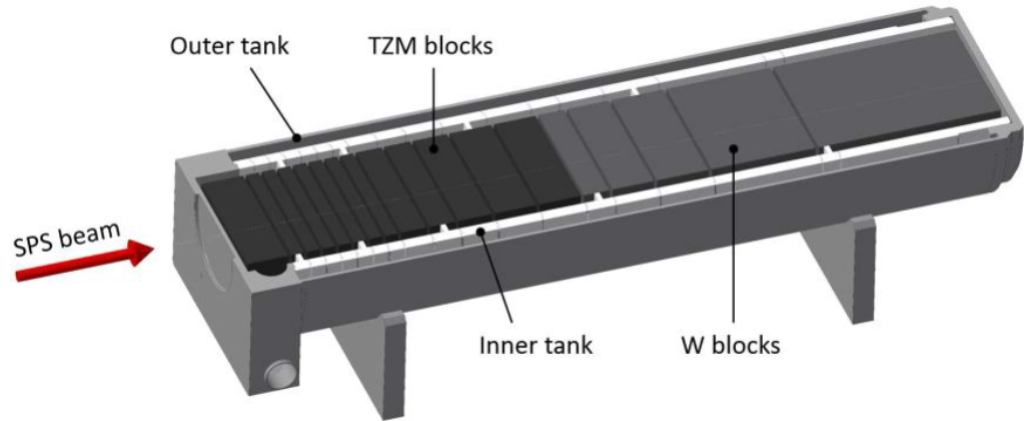
The target needs to be actively cooled by water. The cooling system design is based on the circulation of a high velocity water stream through 5 mm gaps between the different target blocks. To avoid undesired corrosion-erosion effects, all the target needs to be clad with a Tantalum-rich alloy (Ta or Ta2.5W), selected for its high-Z, corrosion resistance and radiation resistance.

The bonding between clad and core material is achieved by means of Hot Isostatic Pressing (HIP) method.

The difference in the coefficient of thermal expansion (CTE) and the conditions at which the bond is achieved cause residual stresses in the clad material, that needs to be evaluated to avoid premature failure of the component.

Block number	Core material	Length (mm)	Weight (kg)
1	TZM	80	40
2	TZM	25	12.5
3	TZM	25	12.5
4	TZM	25	12.5
5	TZM	25	12.5
6	TZM	25	12.5
7	TZM	25	12.5
8	TZM	25	12.5
9	TZM	50	25
10	TZM	50	25
11	TZM	65	33
12	TZM	80	40
13	TZM	80	40
14	W	50	47
15	W	80	76
16	W	100	95
17	W	200	190
18	W	350	330

(a)



(b)

Figure 1.5: Summary of the BDF final target cylinders longitudinal thickness and materials [8] (a), and BDF target assembly [7] (b)

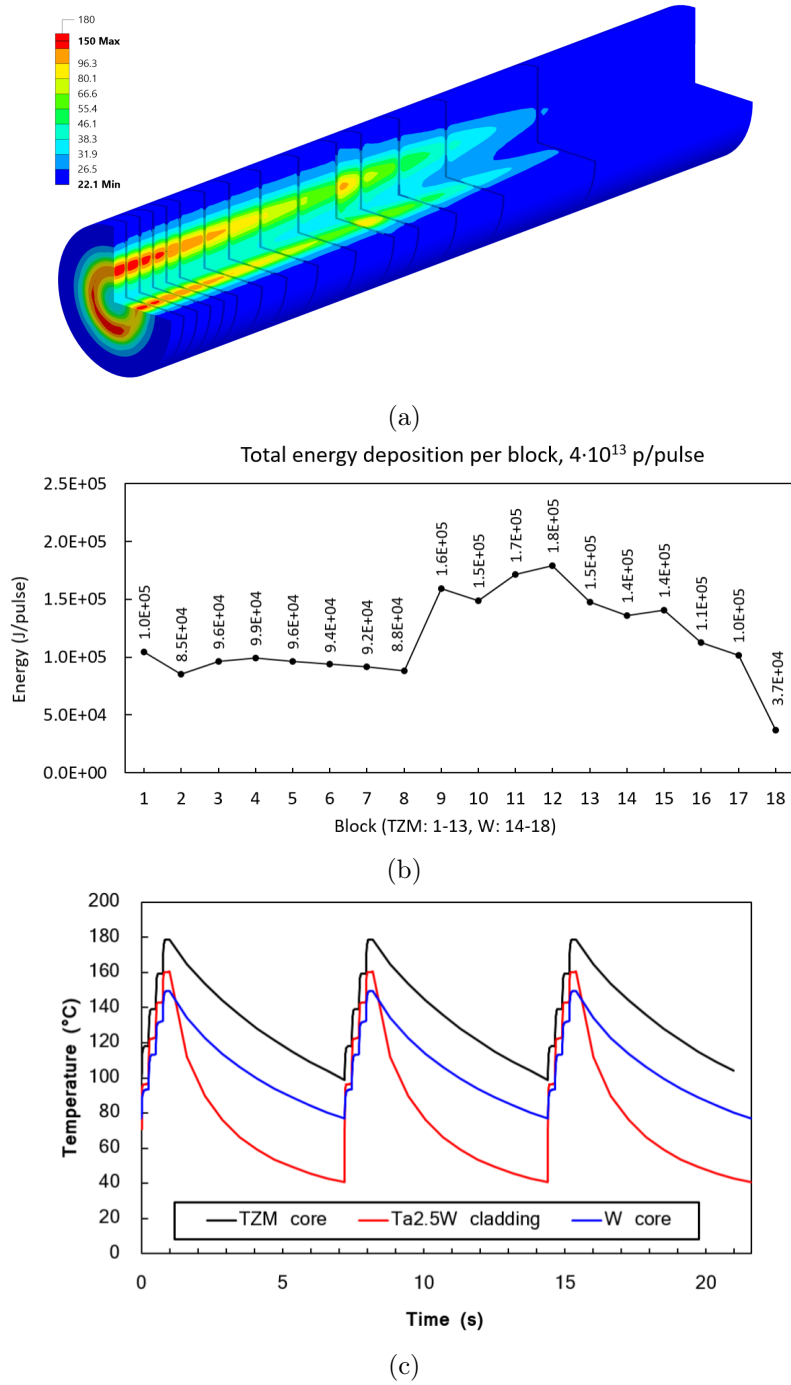


Figure 1.6: Simulated temperature distribution in the BDF target during operation (a), total energy in every block of the BDF target (b), and maximum temperature evolution during 3 beam pulses for the most loaded target blocks (block 4 for the Ta2.5W cladding, block 9 for the TZM cores and block 14 for the W core) (c). [8]

1.1.5 Hot Isostatic Presssing (HIP) process

In the BDF target cylinder, the bond between clad and core material was achieved by Hot Isostatic Pressing (HIP).

During HIP process, materials are placed together in a chamber which allows continuous and controlled application of high gas pressures (up to 2000 bar) and high temperatures (up to 2000 °C).

Different steps of the HIP assisted diffusion bonding are schematised in figure 1.7. The physical bonding process can be divided in four stages [10]:

- First contact: when pressure is applied, the asperity of the opposing surfaces get in contact;
- Plastic deformation: by effect of pressure, time and temperature, the contact area increases through plastic deformation and creep;
- Grain boundary diffusion: atoms diffuse to the remaining voids in order to reduce the surface free energy. In parallel interfacial grain boundary migrates out of the plane of the joint to a lower energy equilibrium;
- Volume diffusion: The remaining intra-granular voids are eliminated through atom diffusion through the volume of the grain.

More specific details of the thermomechanical cycle applied for the production of the BDF target prototypes analyzed in this report are presented in section 4.1.2.

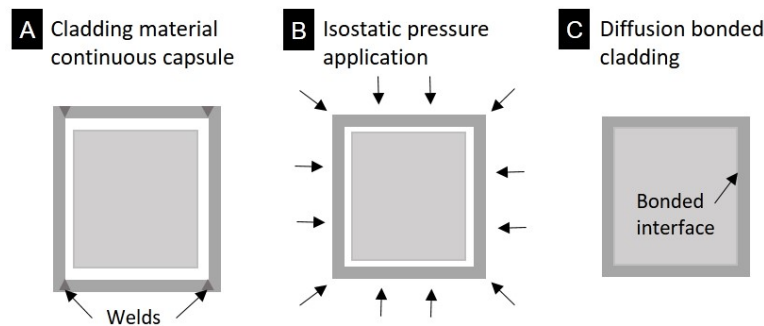


Figure 1.7: Schema of the different stages of the HIP assisted diffusion bonding a) welding a continuous and hermetic clad material capsule over the target material, b) application of isostatic pressure and temperature to bring two surfaces together and start diffusion bonding c) resulting geometry after the HIP cycle, with a diffusion bonded clad

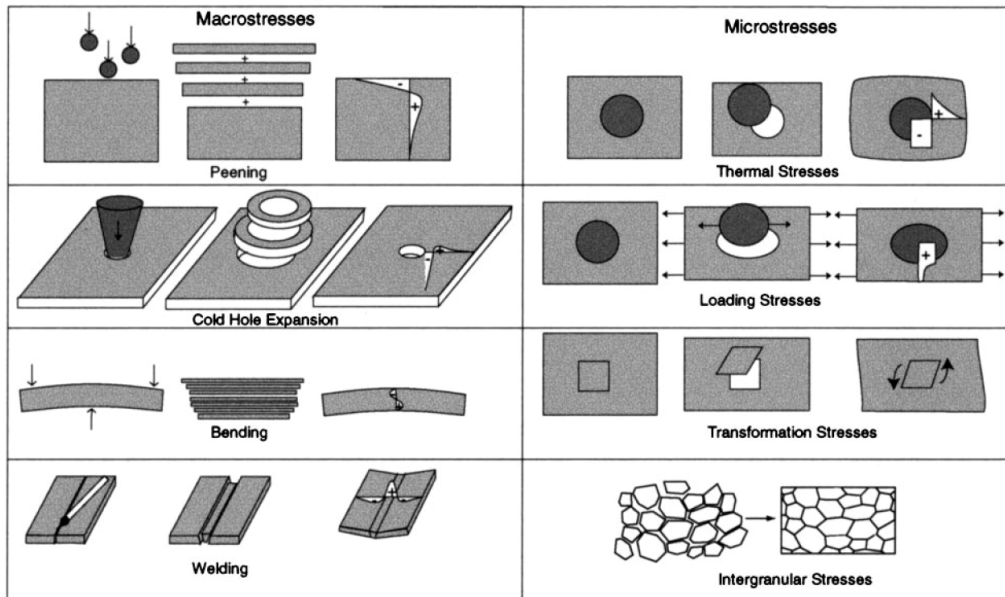


Figure 1.8: Residual stresses possible origin, as reported in [11]

1.2 Residual stresses

Residual stresses can be defined as the elastic stresses that remain in a body after manufacturing or processing in the absence of external forces or thermal gradients (figure 1.8).

Residual stresses can be categorized according to the origin or by the scale at which they self-equilibrate.

Macro residual stresses are referred as Type I, whereas micro-residual stresses acting at grain size are referred as Type II and the ones that are acting at atomic scale as Type III (figure 1.9).

Type II and Type III residual stresses are of particular importance for the general mechanical performance of a component as they might cause crack initiation [12], whereas the Type I residual stresses often determines crack growth.

When not correctly taken into consideration, residual stresses can cause premature failure of a component and high efforts have been devoted in their study, especially in aerospace and nuclear industries.

Residual stresses can also be beneficial, like in the case of shot-peening and the toughening of glass, where a compressive state is purposely induced near the surface. [11]

The most common cause of residual stresses are [11, 13]

- Thermal mismatch (due to different thermal expansion during cooling or

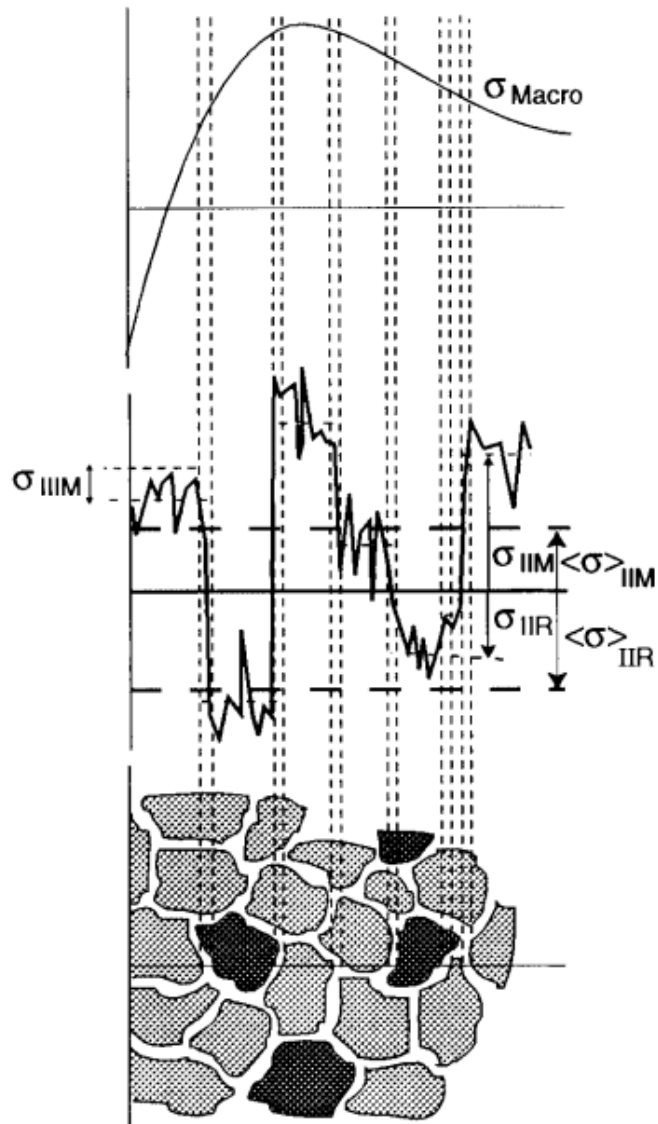


Figure 1.9: Schematic representation of residual stresses in a generic polycrystalline material, as reported by [11]

heating);

- Elastic mismatch (e.g. in composites);
- Non-uniform plastic deformation (e.g. bending);
- Sharp thermal treatments (e.g. welding);
- Chemical treatments (e.g. nitriding of steel);
- Mechanical constrains (e.g. prestressed concrete).

In the presented report, the analyzed residual stresses are generated by non-uniform plastic deformation by means of shot peening and differences in coefficient of thermal expansion, described in the following sections 1.2.1 and 1.2.2.

Grinding and machining operation can also induce large compressing superficial stresses. As they are also of interest in the present report they are described in section 1.2.3.

1.2.1 Shot peening induced residual stresses

Shot peening is an established cold-working technique to improve fatigue life and mechanical performances of a metallic component by inducing a compressive state near the surface of the component.

The shot-peening process consist in bombarding a surface with a high number of hard beads. The induced plastic deformation cause eigenstrains that induce compressive state on the surface and small tensile state in the bulk of the material, as shown in figure 1.10a.

The magnitude and thickness of the compressive layer generated depends on the target material, penning material, and the parameters used (like surface coverage and peening intensity), but is usually in the order of 50% the yield strength of the material. Higher residual stresses, approaching the yield strength of the material, can be achieved with strain penning, which consist of penning the surface as it is strained in tension. [14]

1.2.2 Thermal stresses

Thermal stresses are generated when two or more materials are joined together at temperature different than the one of operation, due to the different coefficient of thermal expansion that the joined materials posses.

If we consider two materials with different coefficient of thermal expansion, we can define T_{esf} (Effective Stress Free Temperature), as the temperature at

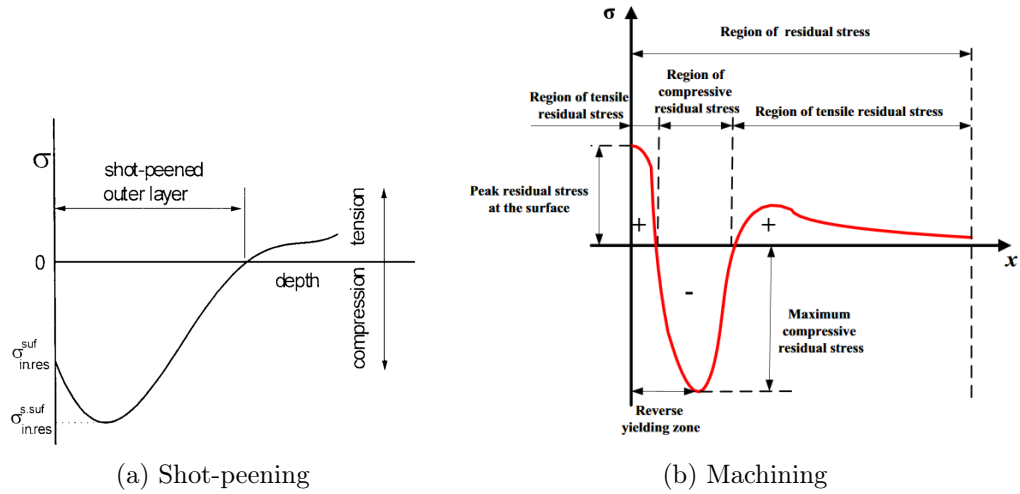


Figure 1.10: Typical residual stress distribution in the surface layer after shot-peening treatment [16] (a), and schematic representation of a typical residual stress profile induced by machining, as reported by [15] (b)

which the couple would be stress free if the thermal expansion misfit $\Delta\alpha\Delta t$ was accommodated elastically.

At any temperature different than T_{esf} the joined material will be subjected to residual stresses proportional to the difference of the operation temperature to the stress-free temperature ($T_{op} - T_{esf}$), the difference in CTE of the joined materials and the respective thickness and geometry. [13]

1.2.3 Machining residual stresses

Machining operations can induce residual stresses on the resulting surfaces which are not easy to control and predict.

As a general rule, gentle milling is known to induce compressive stresses on the machined surface, whereas tensile stresses can be generated by abusive milling, but it is difficult to obtain consistent results.

During cutting action, plastic deformation and compressive state is induced in the workpiece. After the cutting action, spring back occurs near the machined surface. The resulting residual stress profile induced by machining follows the shape presented in figure 1.10b, where a tensile (or small compressive) peak at the machined surface is followed by a more compressive area, followed again by a small tensile region [15].

1.3 Residual stresses measurement techniques

Residual stresses can be difficult to measure accurately and caution is advised when comparing residual stresses measurement techniques with different sampling size, as strong fluctuations and variations can exist between residual stresses of Type I, II and III, as showed in figure 1.9.

In general, residual stresses measurements can be divided into diffraction-based and material removal based.

In the first type, the stresses are evaluated by measuring the change in the crystalline lattice using Bragg's law, as introduced in 1.3.2 and more thoroughly explained in section 4.2.3.

For the latter, the method involves removal of material through machining and subsequent measurement of surface strain relief. If stress-relief can be measured with sufficient accuracy, the pre-existing residual stresses can be calculated by applying Hooke's law.

The macroscopic hole drilling technique introduced in section 1.3.1 and detailed in section 2.1 constitute the most common material-removal based technique.

The novel microscale FIB-DIC ring core milling technique presented in section 1.3.3 and detailed in section 2.3 is an alternative material removal method that utilizes the focused ion beam (FIB) to mill a ring into the material and analyze the deformation of the obtained ring core by means of digital image correlation (DIC) to measure the strain relief.[12]

1.3.1 Hole-drilling strain-gauge method

At the metrology department, measurements of residual stresses according to the standard ASTM E837-13a "Standard Test Method for Determining Residual Stresses by the Hole-Drilling Strain-Gage Method" [17] are routinely performed. The macro-scale blind Hole drilling method was originally developed by Schajer in 1988 [18].

In the hole-drilling strain-gage method, the residual stresses of a linear-elastic material can be determined by attaching a strain rosette to the surface, drilling a hole at the geometric center and measuring the resulting relieved strains, as shown in figure 1.11.

The method is considered as semi-destructive, as the damaged area is reasonably localized and can be neglected for the applications where a shallow hole will not affect the overall performance of the sample.

A special drilling apparatus capable of drilling a hole concentric with the strain gauge rosette within a precision of $\pm 0.004D$ and to control depth of the

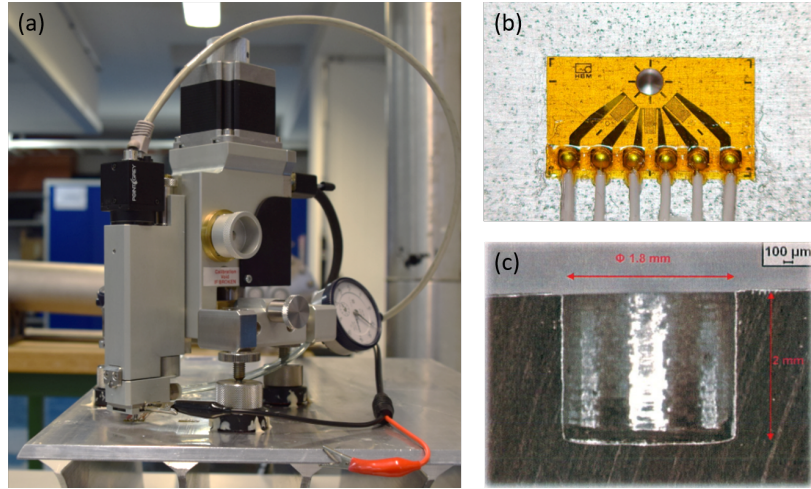


Figure 1.11: Hole-drilling apparatus (a), strain gauge (b) and obtained cross-section (c).

hole with the same precision ($\pm 0.004D$) is required. High speed drilling at 20k to 400k rpm is advised to reduce the generation of residual stresses at the hole boundary.

The relieved strains are mostly influenced by the near-surface residual stresses. The method is therefore diminishing reliable with the depth, and is accurate up to depths in the order of the diameter of the drill bit. Moreover, the first data-point can be affected by surface features and fine alignment of the drill-bit. As an example, using a drill-bit of 1.5 mm in diameter, the technique is considered accurate in the depth range 0.1 mm – 1.0 mm. [11]

Finally, the center of the strain gage rosette should be at least 1.5D from the nearest edge.

1.3.2 X-Ray diffraction

Elastic strain within a crystalline material changes the inter-planar distance between specific crystal planes.

The angle θ at which a specific wavelength λ diffract is correlated inter-planar spacing d by the Bragg law (see figure 1.12):

$$n\lambda = 2d \sin \theta \quad (1.1)$$

Therefore, diffraction methods can be used to determine the elastic stress state of a crystalline material by detecting the change in constructive interference angle caused by the variation in spacing of the lattice plane.

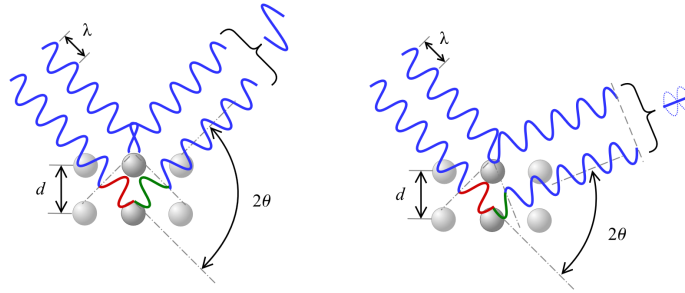


Figure 1.12: Representation of the Bragg condition in equation 1.1 [19].

The precision of the measurement is highly influenced by the measure of d_0 , defined as the stress-free spacing.

A good estimation of d_0 can be obtained by measuring the inter-planar distance in direction normal to the surface, assuming plane stress conditions in the probed volume (good approximation in materials with small penetration depth).

By conducting different measurements at θ values corresponding to planes more oriented away from the normal, the shift in peak corresponds to the varied inter-planar spacing and can be linked to the tensile state inside the material by combining it with the Elastic modulus and Poisson's ratio.

By rotating the sample on its axis (Φ) in at least 2 additional directions, the principal stresses present on the surface of the sample can be fully determined.

Shift in the peak obtained by X-ray measurements give information about the type I and type II stresses, whereas type III stresses can be assessed by advanced techniques based on broadening of the peak, not used in the presented report.

1.3.3 FIB-DIC ring core analysis

Measurement of residual stresses by means of ring-core drilling has been first developed by Keil in 1992 [20] for surface measurements at the macro-scale.

In 2009, Korsunsky et al. [21] proposed an adaptation of the technique to micro-scale measurement of residual stresses by using Focused Ion Beam (FIB) milling to induce stress-relieve and Digital Image Correlation (DIC) to track the resulting deformation. An example is provided in figure 1.14.

In the FIB, high energy ions are used to remove atoms from the sample surface through sputtering process.

The milling process is monitored through co-focal Scanning Electron Microscopy (SEM) imaging. A typical FIB-SEM configuration is visible in figure 1.13.

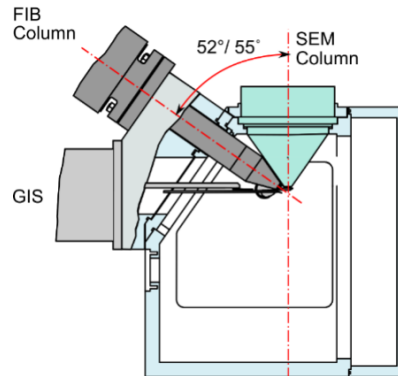


Figure 1.13: Typical FIB-SEM double column configuration, adapted from [12]

The spatial resolution obtainable by FIB milling is in the order of 10 nm. However, the milling rate is quite modest (in the order of few $\mu\text{m}^3/h$). A single ring-core milling measuring 3-4 μm in diameter takes about 2h of FIB milling time to obtain full stress relaxation on the surface of the pillar.

Strain relief is detected by digitally tracking high-contrast features in SEM pictures acquired during the milling procedure.

The technique is of particular interest for evaluating residual stresses where more standard techniques such as macroscopic hole drilling and X-ray diffraction are not applicable or do not provide enough spatial resolution.

The FIB-DIC ring core technique for the measurement of residual stresses is not yet a recognized standard. The primary goal of the presented project (section 1.4.2) is to develop the FIB assisted ring-core analysis of residual stresses within the CERN labs.

1.4 Goals of the project

As a part of the Comprehensive Design Phase (CDP) of the Beam Dump Facility (BDF) target component, primary goal of the presented project is to aid the designing team by evaluating the residuals stresses in some beam dump target prototypes.

The secondary goal, and the novel element, is to implement an innovative FIB-assisted methodology with capability of measuring residual stress at the microscale in the CERN-EN-MME.

More details are presented in the following sections.

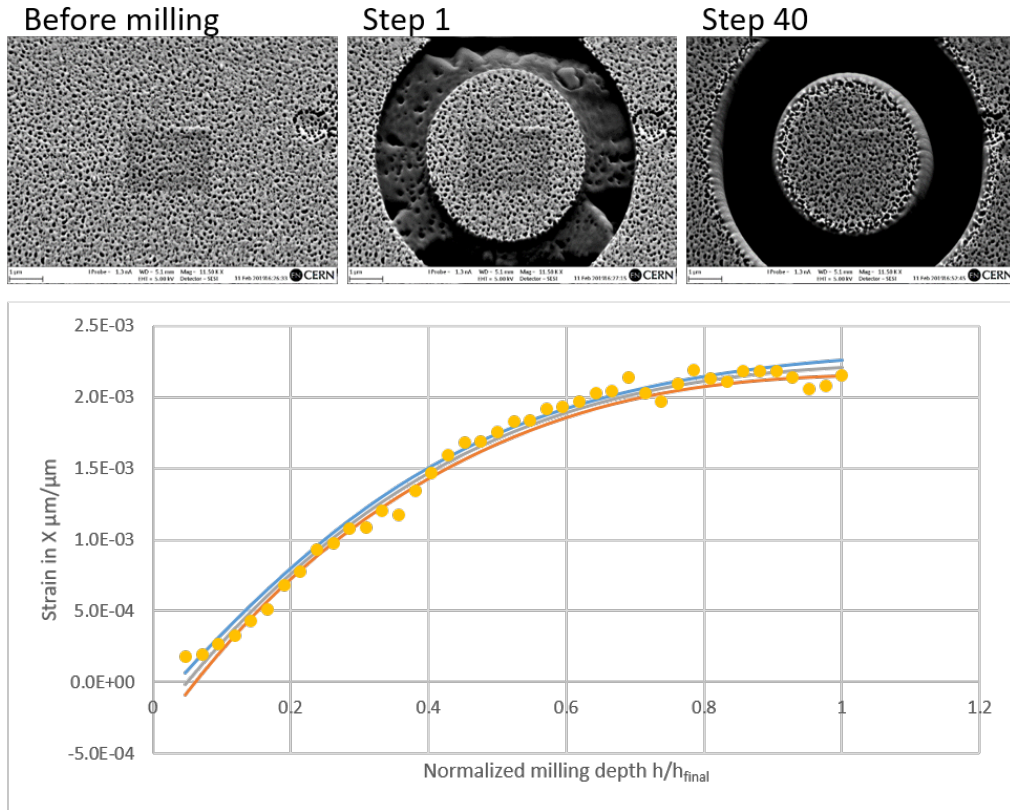


Figure 1.14: Example of an FIB-DIC procedure for local strain relaxation measurements performed on cross-section of shot-peened aluminum sample at $200\ \mu\text{m}$ from shot-peened surface as part of the presented study.

1.4.1 Assessment of residual stresses in BDF (as with ISIS)

The BDF beam target (presented in section 1.1.4) is subject to severe thermo-mechanical stress field due to the energy dissipation from the incoming beam.

High reliability of the component for the expected duration of the experiment (5 years as reported in [8] and [22]) is of crucial importance, as replacements of a damaged component during operation can only be done after complex and expensive operations of movement of heavy concrete shielding blocks and involving remote handling by robot due to the highly radioactive environment.

As mentioned in section 1.2, the average stresses of a component subjected to fatigue cycle is important in determining the lifetime of that component as expressed by the Gerber and Goodman relations for which the fatigue life of a component is inversely proportional to the mean stress for a given level of alternating stress [11].

The design of the presented BDF target is based on the experience gained with the target station 1 (TS1) target design at the ISIS spallation neutron source in the UK, where tantalum-clad tungsten has been used as proton target since 2001 [23].

Studies on stress levels and residual strain distribution on tantalum-clad tungsten targets has been published in [23] and [24] respectively, partially motivated by premature failure of several targets. Residual stress values are in the same order of magnitude than the stress field due to the beam impacts, thus, its assessment is mandatory for the target design.

The ISIS TS1 target consists of 12 plates and operates at 160 kW beam power, whereas the BDF target is designed to operate at 350 kW of average beam power, making the study on residual stresses even more important.

1.4.2 Validation of FIB-assisted ring-drilling residual stresses evaluation as standard analysis technique

Focused ion beam ring drilling for residual stress evaluation is a relatively new technique for residual stresses evaluation, reported the first time in literature by Korsunsky et al. in 2009 [21].

The technique is in the process of being standardized under the european-founded project iSTRESS (Pre-standardisation of incremental FIB micro-milling for intrinsic stress evaluation at the sub-micron scale, EU Contract NMP.2013.1.4-2 [25]) .

The technique is best suited to measure residual stresses at the micro-scale ($1 \mu m$ - $10 \mu m$).

In the iStress framework [12], the technique has been validated on a range of metallic coatings and alloys including Au, Pt, Ti, TiW, a nickel-based superalloy (CMSX-6), TiN and Si₃N₄ ceramic coatings, bulk metallic glasses and diamond-like carbon coatings.

It is of interest for the department to add the FIB-DIC analysis technique to the sets of techniques applicable with the instruments present in the materials analysis lab.

Most of the actual microscopy capabilities (imaging, elemental micro-analysis, microstructure quantification...) are focused on the microstructure observation in the micrometer scale. A mechanical testing method in the same scale range would conveniently complement the microscopy analysis and provide new insights into the materials.

Methodology

In the following chapter, the methodology adopted for the residual stresses evaluation is presented.

For each analysis technique adopted (macroscopic blind-hole drilling, X-ray diffraction, and micro FIB-DIC milling) is presented how data is acquired and how the measured strain values are treated to obtain the stress measurement.

Practical problems that have been encountered in the experimental practice and adopted solutions to minimize impact on the results are also discussed.

2.1 Hole-drilling strain-gage methodology

In the hole-drilling strain gauge method, a hole is drilled in a series of steps at the geometric center of a strain gauge rosette, as introduced in 1.3.1.

Measurements have been conducted according to the standard ASTM E837-13a "Standard Test Method for Determining Residual Stresses by the Hole-Drilling Strain-Gage Method" [17] utilizing SINT Technology MTS3000 – Restan stress analyzer. The setup is visible in figure 2.1.

The stress profile among the depth of the hole can then be determined from the measured surface strains as:

$$\begin{aligned} \epsilon_j = & \frac{1 + \nu}{E} \sum_{k=1}^j \bar{a}_{jk} ((\sigma_x + \sigma_y)/2)_k + \\ & \frac{1}{E} \sum_{k=1}^j \bar{b}_{jk} ((\sigma_x - \sigma_y)/2)_k \cos 2\theta + \\ & \frac{1}{E} \sum_{k=1}^j \bar{b}_{jk} (\tau_{xy})_k \sin 2\theta \end{aligned} \quad (2.1)$$

where a_{jk} and b_{jk} are calibration constants indicating the relieved strains in

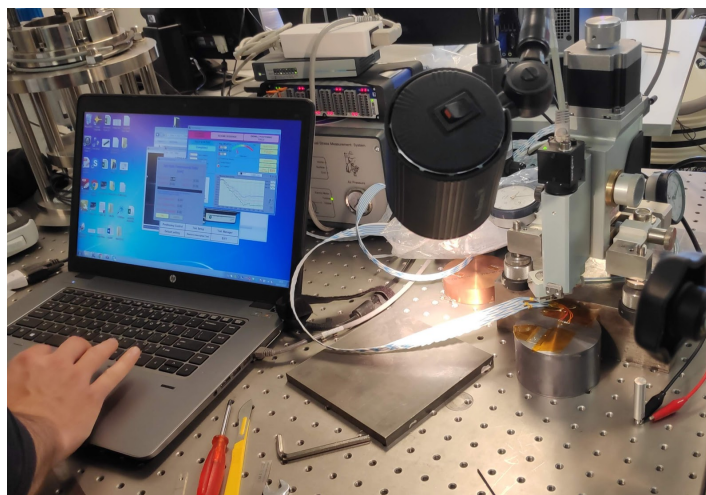


Figure 2.1: Hole-drilling setup utilized for the presented analysis. Picture from first hole drilling attempt on BDF #18 prototype.

a hole J steps deep, due to unit stresses within hole step k . Values of those constants for standard strain rosette patterns can be found in the standard [17].

In the experimental practice, new 1.5 mm inverted cone drill bits have been utilized for every analysis, to ensure dimensional accuracy, and step size of $50 \mu\text{m}$ has been used. Given the extremely low material removal rate (1 hole in about 1 h of machining time), the heat generated by drilling activity is considered negligible and no lubrication is required.

The step-drilling was endured until a minimum of 1 mm of depth is reached.

A flat uniform surface area far from the edges is selected to perform the hole drilling test. The selected location is then de-greased with acetone and lightly sanded to improve glue adhesion. Strain gauge is finally attached using X60 cold-curing methylmetacrylate-based adhesive.

The selected standardized strain gauge rosette used for the presented experiments belongs to the "type B" series in the standard [17].

The zero-position is determined by electrical contact between drill-bit and sample. The first data point might be influenced by surface roughness and by the alignment drill-sample surface.

High stiffness of the drill-sample assembly is ensured usage of methylmetacrylate glue to to fix the sample to the workbench without inducing stresses due to clamping.

As the hole drilling technique is diminishingly sensible to residual stresses the further the distance from the surface, the obtained stress distribution is considered reliable up to 1 mm of depth from the measuring surface.

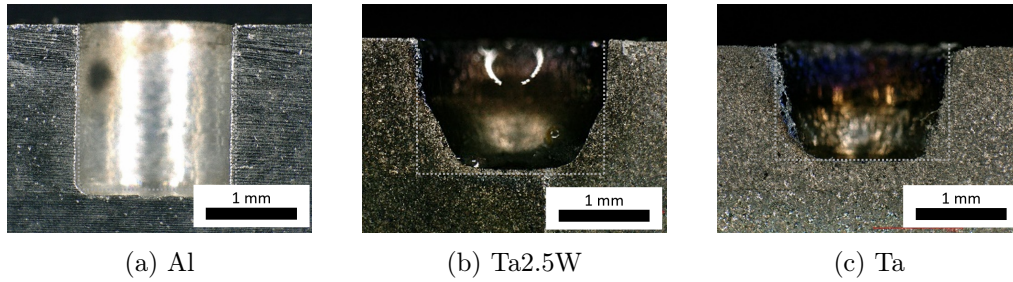


Figure 2.2: Cross-section image of the hole drilled in the aluminum sample (a), in the Ta2.5W of the BDF prototype #14 (b) and in the pure Ta of the BDF prototype #18 (c)

Hardened steel drill bits have been used for the hole drilling in the aluminium sample with good results.

Drilling in Tantalum revealed to be more challenging. Tantalum is reported to be a difficult material to machine [26], as it work harden quite easily and has a strong tendency to galling.

During the hole drilling procedure on pure tantalum and Ta2.5W, several tips broke and a dimensionally accurate hole was impossible to obtain for the target depth of 1 mm, as is shown in figure 2.2.

The results presented in 4.2.2 have been obtained by further reducing the drilling speed and step size and by using diamond drill bits. Due to the poor dimensional accuracy obtained, residual stress measurements obtained in the tantalum clad of BDF targets can only be considered qualitatively.

2.2 X-Ray Diffraction (XRD) Methodology

X-Ray diffraction can be used to accurately measure the inter planar distance in a specific crystal orientation, as introduced in section 1.3.2.

In XRD, X-rays are collimated and directed toward a sample at an angle θ and reflected at an angle 2θ by the crystalline planes oriented in such way that respect the bragg's condition $n\lambda = 2d \sin \theta$ and collected by a detector. A typical XRD setup is illustrated in figure 2.3.

During the analysis the sample can be rotated among its vertical and horizontal axis. The rotation in the plane of the analysis is defined as ϕ , while the rotation in the vertical plane is defined as ψ , as illustrated in figure 2.4

The lattice strain ϵ for a given (hkl) plane can be determined as a function

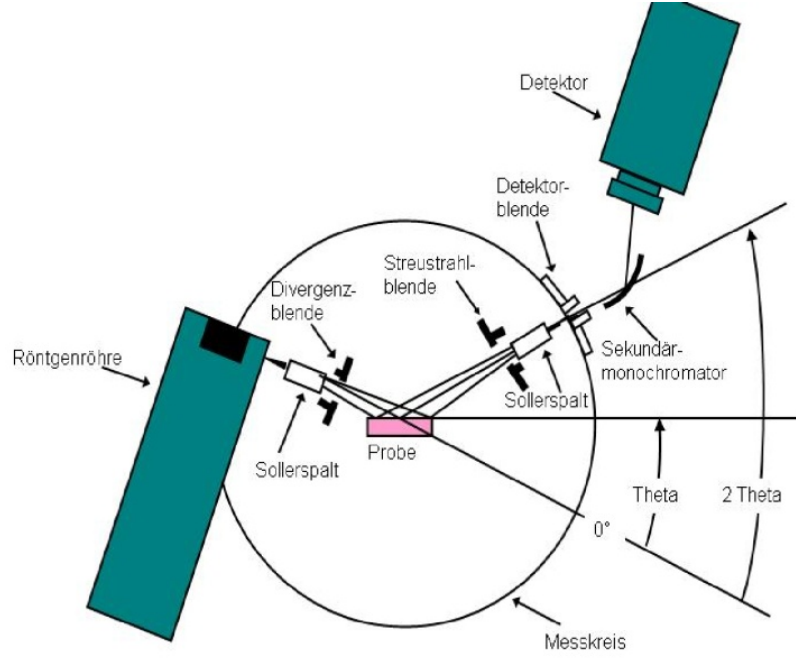


Figure 2.3: Schematic representation of the geometry of the XRD machine. θ is the angle of incidence of the x-rays respect to the sample, 2θ is the detector angle [19].

of the diffraction angles ϕ and ψ as :[15]

$$\begin{aligned} \epsilon_{\phi\psi}^{(hkl)} = \frac{d_{\phi\psi} - d_0}{d_0} = & -\frac{\nu}{E}[\sigma_{11} + \sigma_{22} + \sigma_{33}] + \frac{\nu + 1}{E}\sigma_{33} \cos^2 \psi + \\ & \frac{\nu + 1}{E}[\sigma_{11} \cos^2 \phi + \sigma_{22} \sin^2 \phi + \tau_{12} \sin^2 \phi] \sin^2 \psi + \\ & \frac{\nu + 1}{E}[\tau_{13} \cos \phi + \tau_{23} \sin \phi] \sin 2\psi \end{aligned} \quad (2.2)$$

with notation consistent with the coordinate system defined in figure 2.4.

For near-surface measurements, plane stress conditions can be assumed, and the equation 2.2 can be simplified to:

$$\epsilon_{\phi\psi}^{(hkl)} = -\frac{\nu}{E}[\sigma_{11} + \sigma_{22} + \frac{\nu + 1}{E}\sigma_{\phi} \sin^2 \psi] \quad (2.3)$$

The full strain state of the target material can be determined by conducting a minimum of 3 measurements ad different $\phi \psi$ combinations, but more measurements are usually required to have good fitting.

This method is known as $\sin^2 \psi$ method to determine and is mostly used to determine stress in thin films.

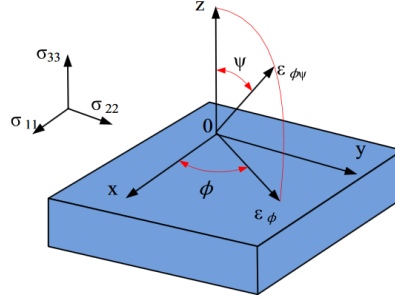


Figure 2.4: Coordinate system used in XRD analysis, reproduced from [15]

In the presented report, XRD has been employed to determine the residual stresses in both the shot-peened aluminum sample and the Tantalum clad in the BDF prototypes.

Diffraction peak position was determined at ψ equal to 0, 10, 20, 30 and 38 degrees and 6 different ϕ angles, for a total of 27 independent measurements for each sample as shown in table 2.1.

	ψ				
	0	10	20	30	38
0	#3	#8	#14	#20	#26
45	#1	#5	#10	#16	#23
90	#2	#4	#12	#18	#22
180		#9	#15	#21	#27
225		#6	#11	#17	#24
270		#7	#13	#19	#25

Table 2.1: ψ and ϕ angles utilized for residual stresses determination in the presented report. The sequence number of the measurement is indicated in the table.

The diffractometer employed for the presented measurement is the Siemens D5000 XRD (in figure 2.5) equipped with $Cu K\alpha$ radiation tube emitting x-rays with $\lambda=1.5406 \text{ \AA}$ and energy of 8.048 keV. Nickel filter and 0.2mm collimator slit complete the setup.

The machine have been calibrated using the standard ASTM-E915-2010 "Standard Test Method for Verifying the Alignment of X-Ray Diffraction Instrumentation for Residual Stress Measurement" [27].

As explained in [28], the expected changes in the d-spacing due to the strain in the sample are in the order of the third decimal place percent.

As the diffraction is dependant on the sin of the incident angle, the change in position of a diffraction peak $\Delta\theta$ is obtained by differentiating Bragg's Law,



Figure 2.5: Siemens D5000 XRD diffractometer utilized during the presented analysis

which gives:

$$\frac{\Delta d}{d} = -\Delta\theta \cot\theta \quad (2.4)$$

As a consequence, at lower angles strains due to residual stresses would result in differences in θ too small to be measured, and using peaks with reflection angle greater than 130 degrees is recommended [28].

For both Al and Ta, a sharp peak present at 2θ around 137° have been employed in the residual stresses analysis.

The divergence slit and receiving slit have been selected to have an analysis area of about 1.5×3 cm at this angle, and have been checked by a phosphor screen, as can be seen in figure 2.6. A picture of the final setup is provided in figure 2.7 for the analysis on the BDF target prototypes.

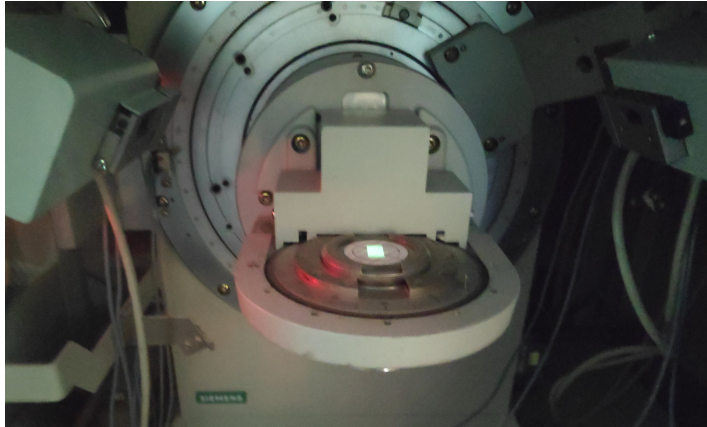


Figure 2.6: phosphor screen mounted in the analysis condition. The area covered by the X-ray beam is about 1.5x2.5 cm.

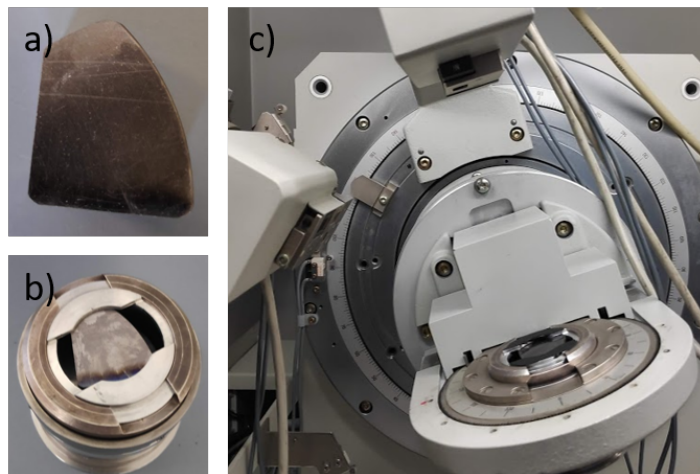


Figure 2.7: Section of the BDF target prototype cut to size to fit in the XRD sample holder (a), Sample fitted in the XRD sample holder (b) and complete setup for the XRD residual stresses analysis on BDF prototypes (c).

2.3 FIB-DIC ring-core analysis

The methodology adopted for residual stresses analysis with FIB-DIC technique in the presented project is derived from the best practices identified in the framework of the iSTRESS pre-standardization of incremental FIB micro-milling for intrinsic stress evaluation at the sub-micron scale [12].

The technique consists of milling a micro-ring and measuring the variation in the shape of the core caused by the stress relieve.

Focused Ion Beam (FIB) is used for the milling, and Scanning Electron Microscope (SEM) is used for the image acquisition necessary to obtain the strain values by mean of Digital Image Correlation (DIC).

The required steps for the FIB-DIC approach for measuring residual stresses are the following :

- Establish patterning and imaging conditions:
 - Apply surface patterning to increase imaging contrast for DIC analysis;
 - Optimize SEM imaging conditions.
- Milling:
 - Define milling geometry;
 - Minimize FIB-induced damage and artifacts;
 - Full automation of FIB-SEM experiments.
- DIC analysis:
 - Optimization of DIC parameters;
 - Subtract large displacements due to image drifting;
 - Calculate displacement and strains;
 - Post-processing to remove badly-tracked points and outliers;
 - Fit data with master-curve;
 - Determine residual stresses.

Every relevant aspect of each of the listed steps is described in the following sections. A a step-by-step practical guide for the milling and post-processing process is presented in appendix C.

The instrumentation adopted for the analysis is the Zeiss XB540 FIB-SEM, recently acquired by the MME group, visible in figure 2.8.



Figure 2.8: Zeiss XB540 FIB-SEM installed in the CERN MME laboratories.

2.3.1 Patterning and surface decoration

In order to perform DIC on the SEM images, the sample surface must present surface features with sufficient contrast. In most of the cases it is required to artificially introduce surface patterns which can be easily recognised by DIC. Texture in the scale of tens of nm is ideal.

As the DIC algorithm recognize unique light intensity levels in a sampling area, the patterns should be rather random. Local deposition of platinum or carbon speckles directly inside the FIB chamber prior to milling can be applied to create the needed pattern, but the technique tend to be local, expensive and time consuming. Other techniques for surface decoration are yttria-stabilized zirconium (YSZ) particle deposition, gold layer remodelling and collidal silica etching.

In the presented work, the gold layer remodelling was used. According to the method, a thin (few nm) layer of gold is deposited uniformly over the surface using external sputtering system. Then, the FIB beam is scanned over the coating surface at low intensity (100-300 pA) to coalescence the gold and form a distinct speckle pattern, as in figure 2.9.

In the presented experiments, the gold layer was obtained by electroplating using the gold sputter coater Edwards S150A. Following the procedure in [29], gold deposition have been conducted in Ar atmosphere of 0.3 atm applying 20 mA of current for 2.5 min.

The obtained gold layer thickness can vary slightly on the geometry and conductivity of the sample. Depending on the gold layer thickness, the exposure

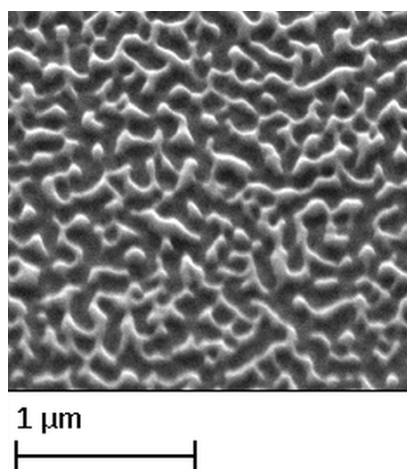


Figure 2.9: SEM image of the sample pattern obtained by gold deposition and subsequent FIB scanning

time required to obtain the right contrast might vary. Starting with low dwell time (100 ms) and repeating the operation until the correct contrast is reached is advised. In figure 2.10b an example of under-exposed and correctly exposed sample is presented.

The textured area needs to be big enough to cover the entire field of view that will be used during the FIB milling. As 11.5k magnification has been used during the milling image acquisition, a magnification of 11k was used for texturing. The sputtered gold layer must be kept as small as possible ($< 50nm$) as an excessive thickness of the film is unnecessary and might induce some residual stresses and influence the measurement.

2.3.2 SEM imaging optimization

FIB-SEM configurations are usually designed to have the SEM column vertical and the FIB at an angle (figure 2.11).

To correctly perform the FIB milling required by the technique, the sample has to be mounted flat and then tilted to be orthogonal to the FIB gun.

Focus and working distance had to be adjusted to have both ion and electrons beams aligned and focused on the same spot.

Due to the incident angle of the electrons, the side walls of the milled geometry are visible and the milling process can be effectively monitored.

To reliably track the feature in the DIC, having a SEM image of high quality is of primary importance. Focus and astigmatism needs to be adjusted to have the best possible contrast.

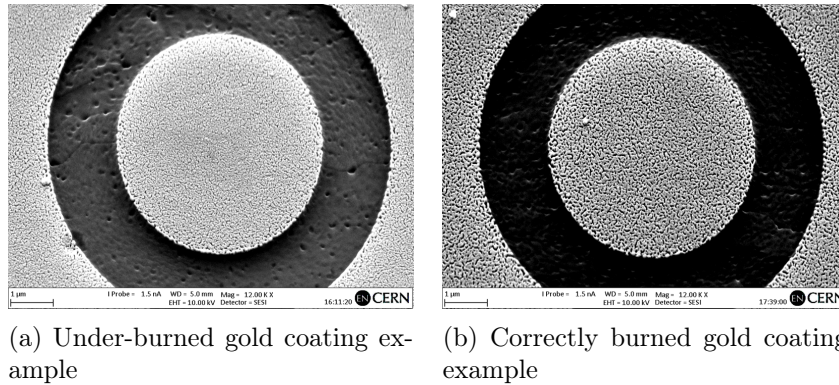


Figure 2.10: Example of under-burned (2.10a) and correctly burned (2.10b) gold-coated aluminum sample. the first image did not have contrast enough to correctly perform DIC

As the sample is tilted 54° , tilt correction has to be applied to ensure dimensional accuracy. Dynamic focusing proved to be unnecessary at the high magnification used for the analysis.

Prior to milling, contrast and brightness of the SEM images has to be adjusted to have the widest possible Gaussian distribution of light intensity in the image, without over-exposed or under-exposed areas.

Once the parameters are set, no change must be applied until the end of the milling procedure for the DIC to work correctly.

2.3.3 Milling procedure

During milling process, high energy ions impact the surface and the energy is dissipated in a series of inelastic scattering events, causing material removal.

Milling rate is proportional to the density of the material. Higher density materials are reported to be easier to mill, as the lower interaction volume cause the ions to give up their energy closer to the surface. FIB intensity of 30 KV, 300 pA and 30 KV, 150 pA have been used for Al and Ta samples respectively.

For the residual stresses analysis, a ring-core geometry was selected.

The inner radius utilized in the following experiments has been $2.5 \mu m$ for the inner radius, and $4 \mu m$ for the outer.

The milling movement needs to be set to spiral from the external to the internal diameter to limit the re-deposition of the milled material on the sides of the pillar.

As rule of thumb, multiple milling passes with low ion dose per pass is preferable, as this strategy tend to produce fewer artifacts and less re-deposition effects.

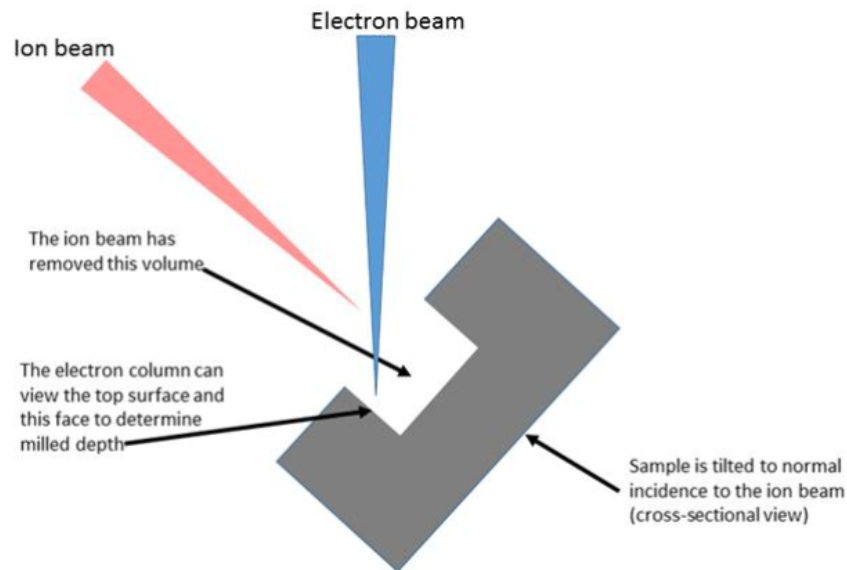


Figure 2.11: Schematic representation of the beam path impacting the sample [12]

The final milling depth must be enough to fully relieve the stresses in the sample. A milling depth approximately equal to the pillar diameter generally suffice, and is considered reached when is not possible to distinguish the bottom of the trench by SEM imaging.

In the presented experiments, full stress relief have been obtained in between 40 and 80 passes for each pillar (depending on material and crystal orientation).

If depth scaling is required, milling rate calibration is needed to obtain depth resolution. However, milling rate depends also on other parameters like crystalline orientation and milling depth due to the effects of re-deposition and partial screening of the beam.

As the stresses are thought to be constant in the depth of the milled materials, and since is difficult to establish the milling rate with an acceptable degree of certainty, depth profiling of the residual stresses has not been performed in the presented experiments.

Due to the Gaussian shape of the beam, the edge quality of the milled shape can also be affected, as visible in figure 2.13.

The milling rate depends on the crystal orientation. If ring-core milling is performed across a grain boundary, the different milling rate can cause not-uniform stress relieve, making the measurements obtained unreliable.

An example of the effect of non-uniform milling across a grain boundary is shown in figure 2.12.

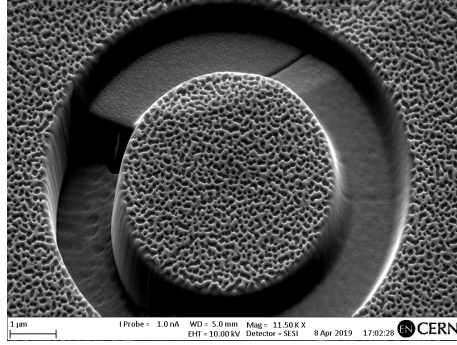


Figure 2.12: Example of SEM image of FIB ring-core milling executed on the intersection between 3 grain boundaries in Ta sample.

Ion exposure can induce damage and amorphisation of the material in the region confined between 10 and 100 nm from the edge of the milled trenches.

When a crystalline material undergoes amorphization, it usually increase in volume. This effect has the same magnitude (i.e. nm per mm^2) than the expected movement from residual stresses relaxation detected by FIB-DIC analysis, and constitute a limit of the spatial resolution of the DIC-FIB method.

2.3.4 Digital Image Correlation (DIC)

Digital Image Correlation (DIC) is a full-field non contact strain measurement technique firstly developed in 1983 by Sutton et al. [30].

By DIC, displacements are determined based on a set of images of the specimen surface.

Features in the image are digitally tracked and the obtained displacements are used as a virtual strain gauge.

In the DIC software used, features in the images are recognized by the unique light intensity distribution inside subset (by default 20x20 pixel). The movement of the subsets is tracked with sub-pixel accuracy, and a strain field can be calculated, as schematized in figure 2.15.

Image quality (well-focused, free of noise, with a large range of contrast and brightness) is of key importance for the DIC algorithm to work properly.

During the milling the samples are perpendicular to the FIB beam hence tilted with respect to the SEM beam. Therefore tilt correction is needed to correct the SEM images prior to DIC.

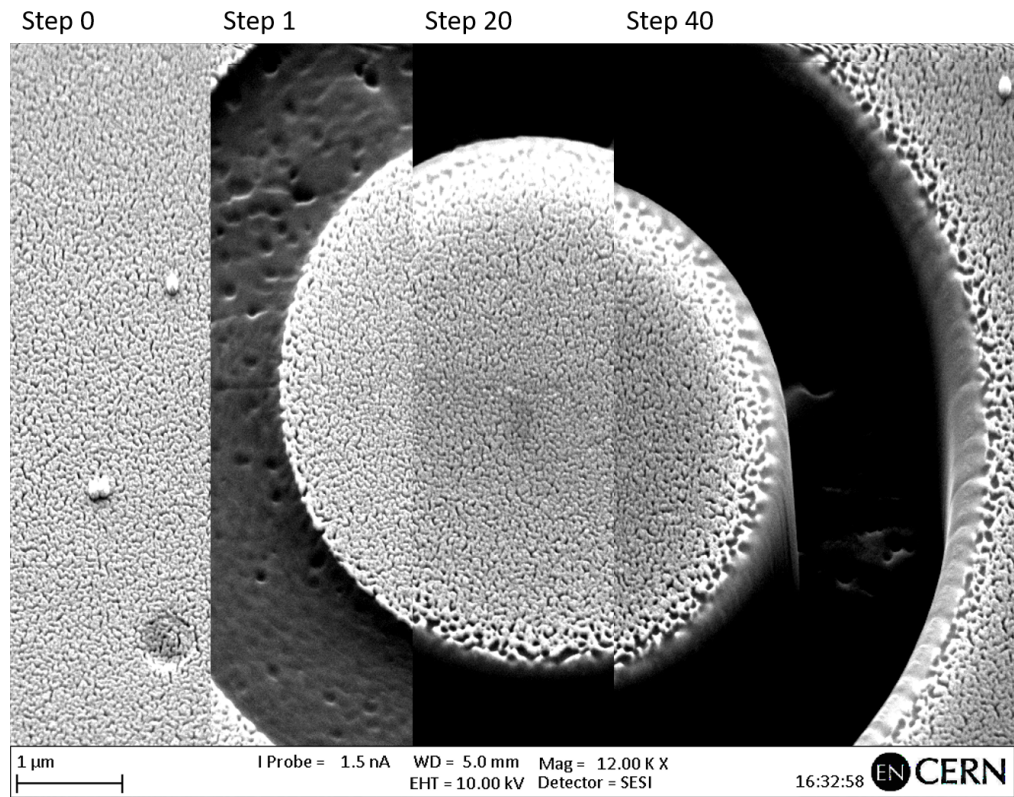


Figure 2.13: Picture composed by multiple snapshots taken before FIB milling procedure (step 0) and after 20 and 40 passes respectively. The drifting and damage phenomena caused by the FIB beam on the edges is evident.

Good calibration and aberration control of either columns is needed to archive good results.

DIC analysis is scale-independent, meaning that it will give a strain value independently on the scale of the picture.

In the presented application, images at 11.500 magnification obtained by SEM secondary electrons have been used for the DIC analysis, and the gold pattern applied as described in section 2.3.1 is used to provide the required random distribution of high contrast features.

It is of primary importance that the SEM images remain stable and do not degrade significantly during FIB milling operation. Charging of the sample, unstable clamping and beam instability can cause heavy variation in the image quality that might jeopardize the image recognition.

Rigid-body translation (drifting) caused by sample charging and beam instability must be minimized.

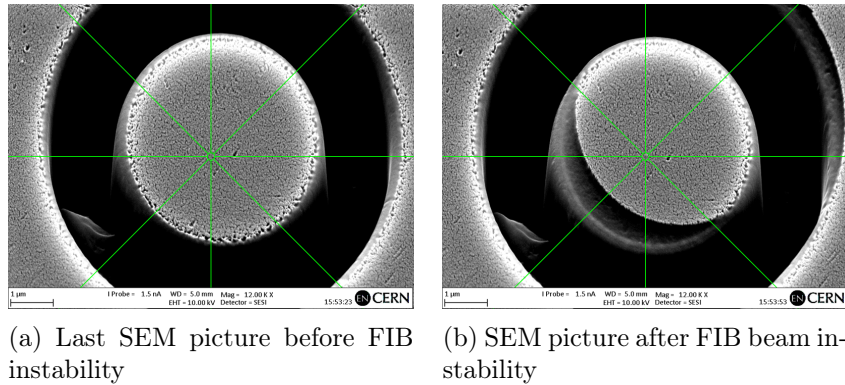


Figure 2.14: Effect of beam instability on FIB ring-core milling process in gold-coated shot peened aluminum sample

Small drift can be corrected by tracking features in un-affected area of the sample and subtract then the obtained field to the movement of the tracked features on the pillar to obtain the strain field.

However, if the drift is excessive, the image correlation software can fail to correctly track the displacements. In extreme cases, the area in which the displacements are calculated by DIC can move out of the field of view.

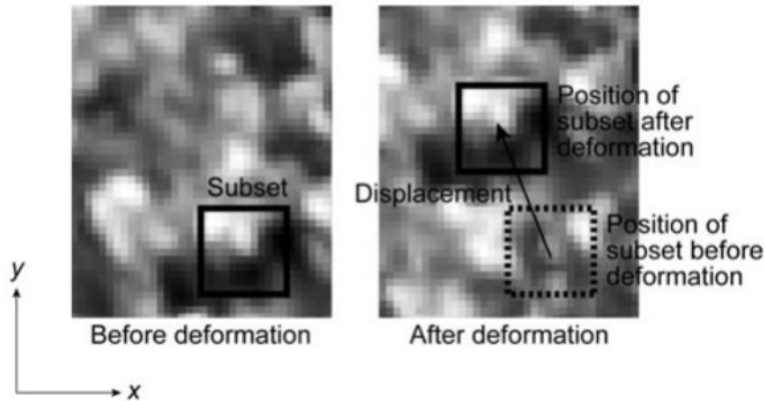


Figure 2.15: Basic principle of digital image correlation [12]

Due to the scale at which the DIC technique is applied, some noise in the measurements is expected. In the FIB-DIC ring core milling, the accuracy of the measurement is improved in 2 ways:

- It has been demonstrated [31] that the stress is uniform in the pillar, therefore by tracking multiple features and averaging the displacements the noise can be reduced;

- Accuracy can be greatly improved by performing the DIC analysis at incremental milling depth and fitting the recorded strains with a "master-curve" obtained by FEM analysis.

After DIC analysis, the displacement of every subset is outputted. Badly-tracked features can be removed in post-processing.

2.3.5 Data analysis

For ring-core geometry, the general form of the strain relief profile ("master curve") has been determined through FE simulations of the milling process. The functional representation of the strain-relief profile obtained is shown to be [32]:

$$f(\Delta\epsilon_{\infty,z}) = 1.12\Delta\epsilon_{\infty} \cdot \frac{z}{1+z} \left[1 + \frac{2}{(1+z^2)} \right] \quad (2.5)$$

where $z = h/(0.42 \cdot d)$, h is the milled depth, d is the core diameter and $\Delta\epsilon_{\infty}$ is the full strain relief at infinite milling depth.

A plot of the strain relief curve is provided in figure 2.16.

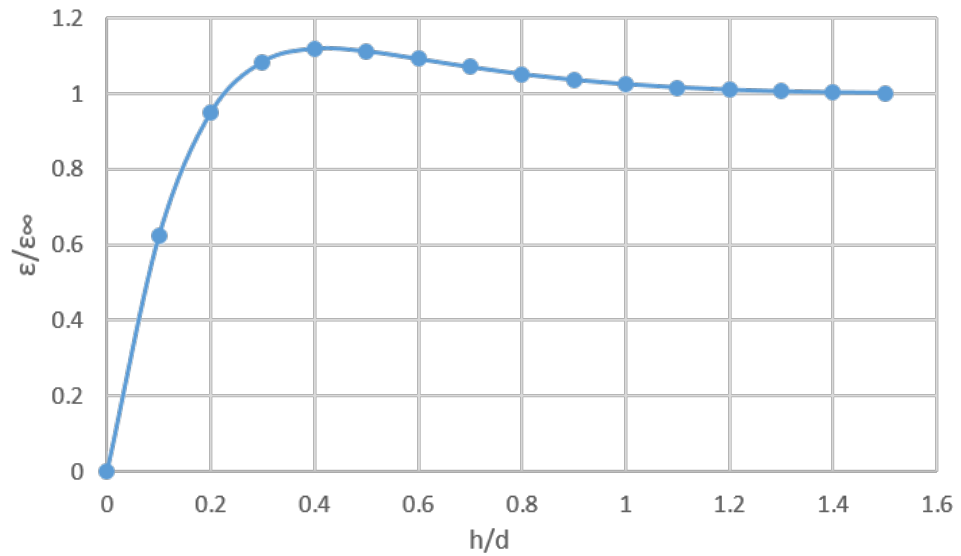


Figure 2.16: FE modelled normalised stress relief as a function of normalised drilling depth, as calculated using the equation 2.5. The represented strain relief is normalised with respect to the modulus $[E/(1-\nu)]$ and trench depth is normalized with respect to the core diameter $[h/d]$

Commenting on the figure 2.16, the following considerations can be derived:

- Most of the strain relief occurs in the early stages of milling close to the surface ($h/d < 0.3$);
- The profile present a "pinch like" peak at $h/d = 0.4$, and then tend toward a plateau for $h/d > 0.6$;
- Full stress relief is considered achieved when the trench depth is equal to its diameter ($h/d = 1$).

For calculating the residual stresses it is strictly necessary to measure the displacements when all the stresses has been relieved.

As the milling rate is difficult to estimate with precision, the exact depth of the trench has to be considered unknown, but it is safe to assume that the milling rate will remain reasonably constant during the milling process (e.g. $h = \eta I$, with η an experimental constant and I the milling step) .

From strain to residual stresses

During ring-core milling, the stress gets locally relieved in both the in-plane directions.

Elastic modulus and Poisson's ration are the two elastic constants necessary to calculate the strain measurements from the displacement field.

Due to the proximity to the free surface, the out of plane stresses are assumed to be equal to zero (plain stress condition).

Assuming homogeneous and isotropic material, the expression of the principal stresses in the surface for the ring-core milling geometry are:

$$\sigma_x = -\frac{E}{(1-\nu^2)}[\Delta\epsilon_\infty^x + \nu\Delta\epsilon_\infty^y] \quad (2.6)$$

and

$$\sigma_y = -\frac{E}{(1-\nu^2)}[\Delta\epsilon_\infty^y + \nu\Delta\epsilon_\infty^x] \quad (2.7)$$

where $\Delta\epsilon_\infty$ represents the level of strain achieved at the maximum milling depth, evaluated by fitting the "master curve" (equation 2.5, plotted in figure 2.16).

Sample sectioning compensation

The FIB-DIC method is intrinsically a surface analysis technique, but in many cases the most relevant residual stresses are located below the surface.

In order to access the region of interest, sample sectioning has to be performed. The sectioning process relieves the stresses in the direction normal to the new surface.

To fully understand the consequences of cross-sectioning in a generic tensile state, consider the case of a long body with stresses acting perpendicular to its length (plane strain).

As a consequence of the cross-sectioning, the plane strain state ($\tilde{\sigma}_x, \tilde{\sigma}_y, \tilde{\sigma}_z, \tilde{\epsilon}_x, \tilde{\epsilon}_y, \tilde{\epsilon}_z = 0$ in figure 2.17) originally present becomes plane stress on the cross-section plane ($\hat{\sigma}_x, \hat{\sigma}_y, \hat{\sigma}_z = 0, \hat{\epsilon}_x, \hat{\epsilon}_y, \hat{\epsilon}_z$, in figure 2.17).

The cross-sectioning effect is effectively equal to the application of virtual stress equal and opposite to $\tilde{\sigma}_z$.

The applied force causes out-of-plane stresses to reach zero, but will also modify the in-plane stress and strain values due to the added shear stress components ($\tilde{\sigma}'_x = -\sigma_z/\nu$ and $\tilde{\sigma}'_y = -\sigma_z/\nu$).

In figure 2.18, the plane stress condition induced by cross-sectioning is derived from the initial plane strain condition by de-coupling and then combining the effect of $\tilde{\sigma}_x$ and $\tilde{\sigma}_y$. [33].

In the most generic case, ϵ_z is not equal to zero prior to sectioning due to external forces and residual stresses also acting also in the z direction.

Only from analysis on the xy cross-section plane is possible to determine the residual stresses acting in the x and y direction due to the $\tilde{\sigma}_x$ and $\tilde{\sigma}_y$.

Besides the intrinsic modification of the tensile state, the sample sectioning operation can also induce superficial residual stresses build-up during sample preparation.

Low-speed machining (via diamond wire or diamond wafering) followed by incremental fine diamond polishing or electropolishing can reduce the affected region and have been employed during the sample preparation, as described later in the experimental section 3.1.2 and 4.1.3.

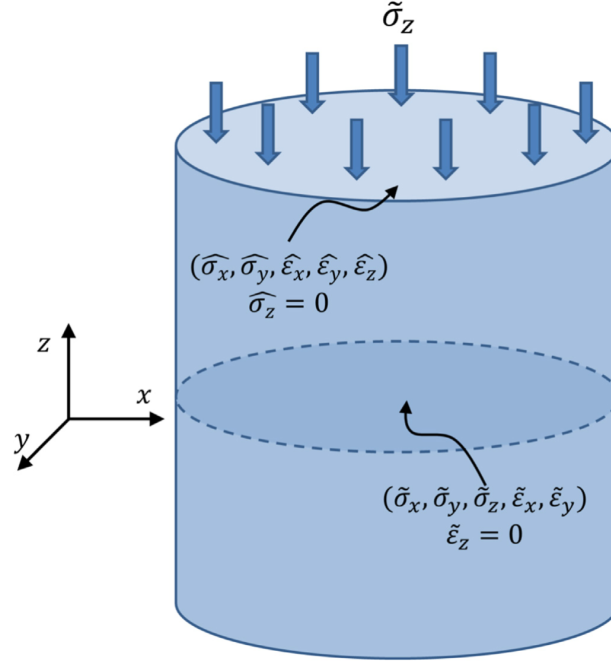


Figure 2.17: Schematic representation of the plane strain conditions present prior to sectioning and plane stress conditions induced after sectioning [33]

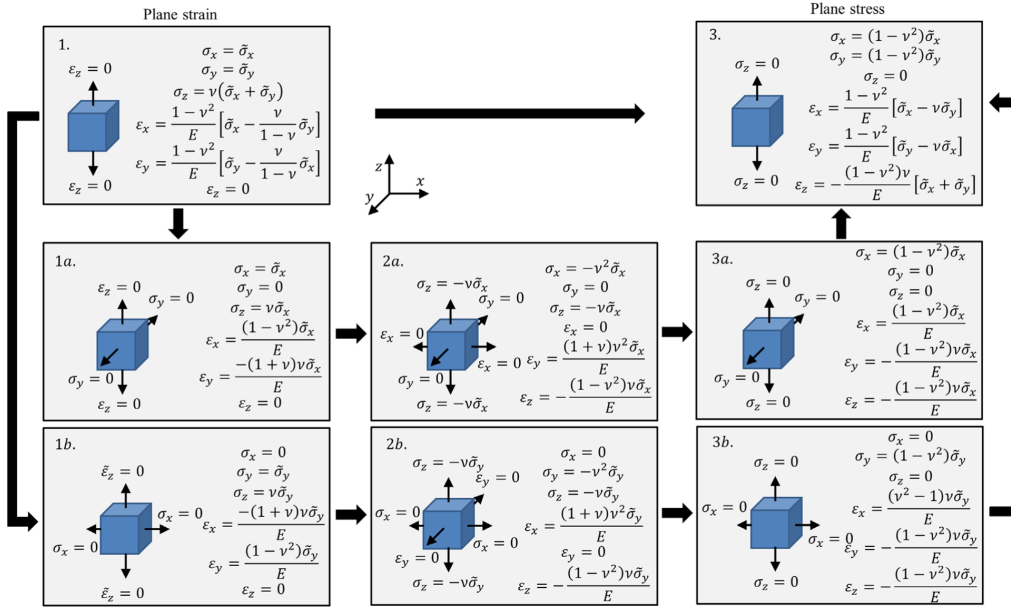


Figure 2.18: Derivation of the plane stress condition present on the surface of a cross-sectioned sample from the original plane strain condition present in the bulk. All relationships are written in terms of the in-plane stresses originally present ($\tilde{\sigma}_x$ and $\tilde{\sigma}_y$) [33]

Residual stresses in shot-penned aluminum sample

To verify the methodology, the three presented techniques for measuring residual stresses (macroscopic hole drilling, XRD and FIB-DIC analysis) have been applied to a sample of shot peened aluminium.

3.1 Prototype description

The sample selected for the analysis was a shot peened aluminum sample traditionally used in the metrology department to calibrate the macroscopic hole drilling apparatus.

The process parameters used during the shot-penning of the aluminium sample used in this report are unknown. However, from Vickers hardness test of on the surface (affected region) and far from the surface (non-affected region), an increase in the HV1 hardness of 18% (from 176 to 217 HV1) was measured. Measurement data is provided in the appendix [D.1](#).

Relevant material properties are described in section [3.1.1](#), whereas the sample preparation and sectioning performed prior to each technique is described in section [3.1.2](#).

3.1.1 Material properties

Aluminum is a metallic material with face-centered cubic (FCC) crystalline structure and lattice constant of 4.046 Å.

The specimen under analysis was made of 3003 aluminum alloy (EN AW-3003), belonging to the 3xxx-series of aluminum alloys designed for cold-working.

The composition of 3003 aluminum is: [\[34\]](#)

- 0.05% to 0.20% Copper;

- 0.00% to 0.70% Iron;
- 1.0% to 1.5% Manganese;
- 0.0% to 0.6% Silicon;
- 0.0% to 0.1% Zinc;
- Remaining: Aluminum.

The density of this material is $2.8 \frac{g}{cm^3}$. The penetration depth of the X-rays into the material was calculated with the software AdsorbX for the beam and material combination. Absorption rate in function of the depth is presented in figure 3.1, where is shown that 90% of the signal is coming from the first $80 \mu m$.

From the supplier specifications [35], the yielding point is 145 MPa, elastic modulus is 70 GPa and Poisson's ratio is 0.33.

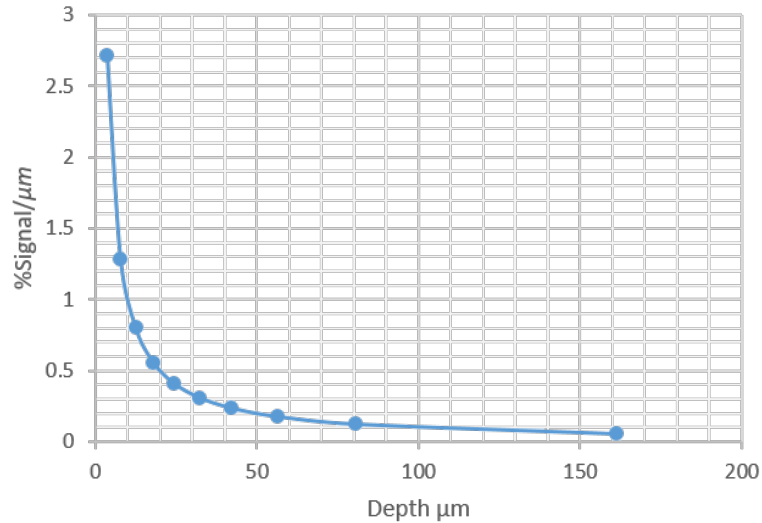


Figure 3.1: X-rays penetration in aluminum as determined by the software Absorb-x for the radiation source used in the experiments and Bragg's condition. 90% of the signal is coming from the first $80 \mu m$

3.1.2 Sample extraction and workplan

The sample allotted for the test has dimensions of 50x50x10 mm shot panned uniformly on all the surfaces.

Macroscopic hole drilling analysis has been performed on 3 different locations of the sample "as is" prior to any sectioning or surface preparation. Results are presented in section 3.2.1.

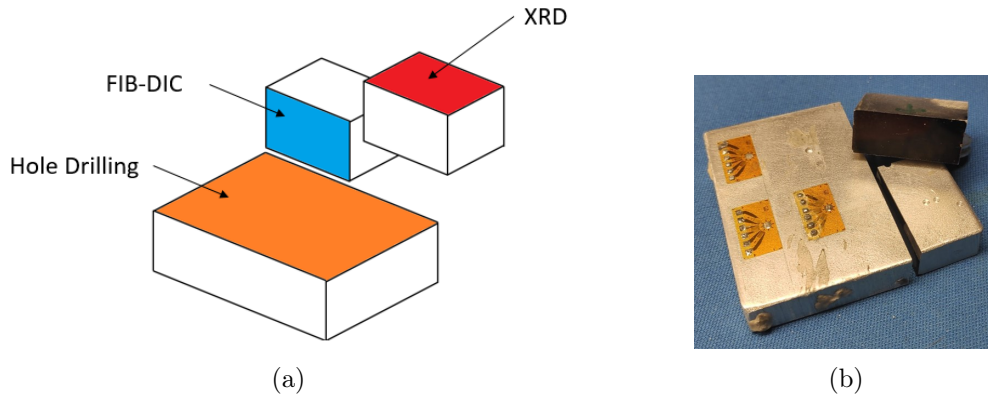


Figure 3.2: Schematic representation of sample sectioning an measurement plane for each of the residual stresses measurements adopted (a) and picture of the final sample after sectioning and testing (b)

For subsequent XRD and FIB-DIC analysis, sectioning was necessary. Two parts of roughly 1.5x2.5 cm have been extracted from the specimen for the purpose. XRD analysis has been performed on the shot-peened surface of one of the small extracted samples, whereas FIB-DIC analysis has been conducted on one of the freshly revealed cross-sectional areas, as shown in figure 3.2.

The sectioning planes have been selected to reveal a cross-sectional view of the one of the drilled holes to check the dimensional consistency (image presented in section 2.1, figure 2.2a).

As the FIB-DIC analysis has to be conducted on a cross-sectioned surface, it is of paramount importance not to induce residual stresses during the necessary machining operation. For that purpose, cross-sectioning have been conducted using low speed diamond wire cutter (3242 Precision Vertical Diamond Wire Saw) in order to reduce to a minimum the affected layer.

The cross-section area to be analyzed with FIB-DIC technique has been then carefully prepared with conventional metallographic procedures using grinding paper from 2000 GRT to 4000 GRT followed by fine polishing up to 1 μm until mirror surface is reached. Electroplating with gold using gold sputterer coater "Edwards S150A" followed, in order to obtain the optimal surface texture required by DIC analysis, as described in section 2.3.1

As the gauged material by FIB-DIC analysis is in the order of few μm^3 , to fully evaluate the stress profile of the shot peening several ring-cores have been milled on the cross-section area at 100 μm , 200 μm , 300 μm , 600 μm and 1000 μm from the shot-peened surface. A minimum of 5 ring-cores have been milled at each location.

3.2 Residual stresses analysis

Results of the residual stresses analysis performed are presented in the following sections.

3.2.1 Macroscopic hole drilling

The macroscopic hole drilling measurement revealed a compressive state varying from -150 MPa close to the surface to a maximum of about -300 MPa at 180 μm from the surface and reaching 0 or small positives (<20 MPa) for depths over 500 μm . Results are presented in figure 3.3.

The measurement derived from the three holes drilled are well aligned with a maximum variation between different measurements within ± 26 MPa and an average standard deviation of 10 MPa.

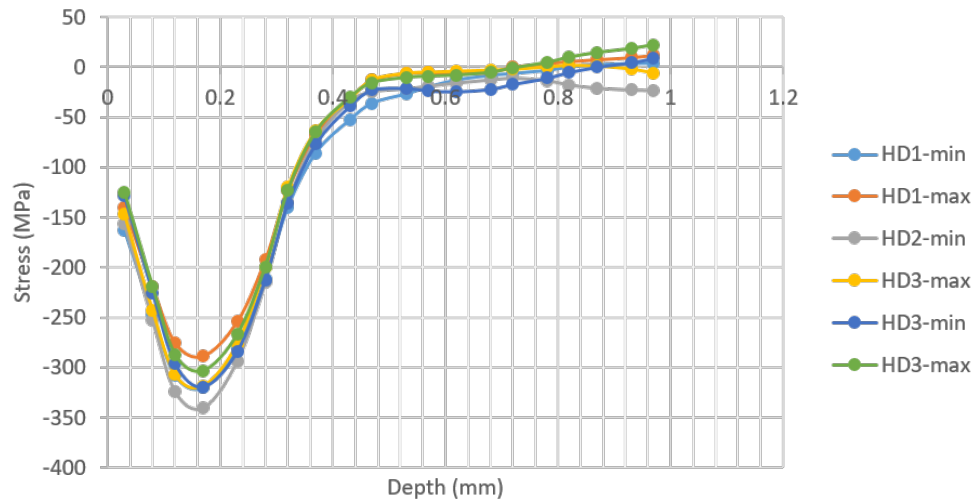


Figure 3.3: Residual stresses measurements obtained with the hole macroscopic hole drilling technique. Depth resolution (used drilling step-size) of 50 μm . The maximum and minimal principal stresses obtained by 3 independent measurement are plotted. The average standard deviation of the measurements is within 10 MPa

3.2.2 XRD analysis

A preliminary scan in a wide 2θ range (60 to 150 degrees) was performed to determine which peak to utilize for the residual stresses analysis. The resulting scan is visible in figure 3.4. The diffraction peak between 130 and 140 degrees has been selected as it was reasonably sharp and isolated, and high angles allow better resolution, as discussed in section 4.2.3.

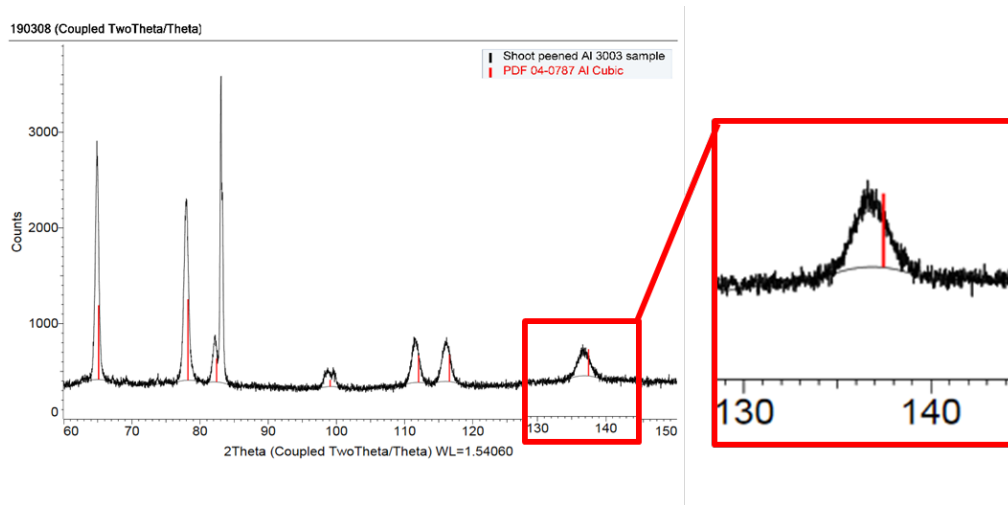


Figure 3.4: XRD scan in the 2theta range 60-150 degrees. The red lines indicates the predicted peak position in un-stressed conditions

The selected peak at 137.5° is also recommended in [28] for aluminum X-ray analysis. The peak corresponds to the $\{422\}$ plane in the FCC aluminum lattice.

27 scans have then been performed at the angles indicated in table 2.1 section 4.2.3, in the 2θ range of 133° to 141° . The results are presented in figure 3.5 for the first scan.

The analysis has been repeated two times on the same sample.

The residual stresses as calculated from the shift in peak position with the " $\sin^2 \psi$ " method reported in section 4.2.3. An example of peak-fitting with and without stresses applied is reported in figure 3.6.

Results of the analysis are reported in table 3.1 A bi-axial compressive state of $-250[MPa]$ with a standard deviation of $17[MPa]$ is recorded by the technique in the X-ray interaction volume.

	Measurement 1	Measurement 2
Minimum principal	-265 MPa	-269 MPa
Maximum principal	-238 MPa	-229 MPa

Table 3.1: XRD measurement of residual stresses on surface of shot-peened aluminium sample. Results show the presence of a biaxial tensile state of $-250[MPa]$ with a standard deviation of $17[MPa]$

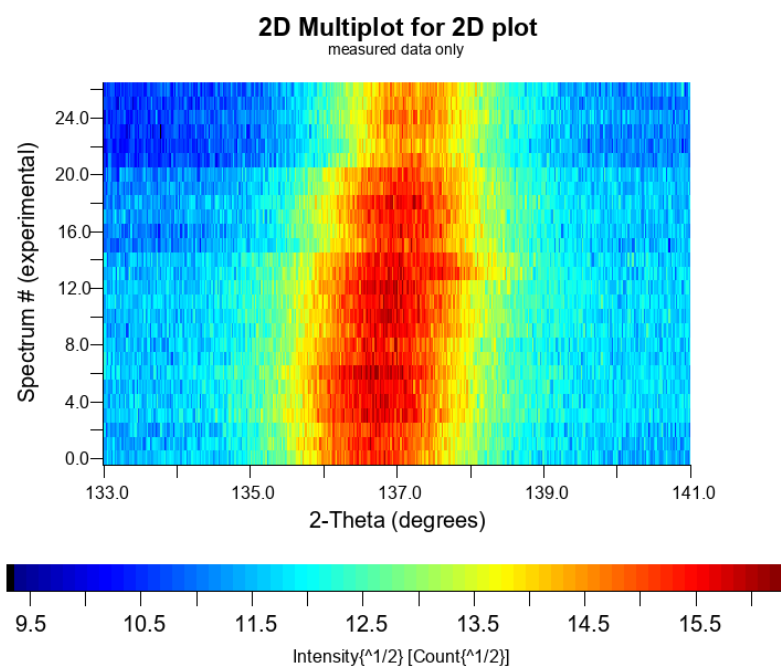


Figure 3.5: XRD scan in the 2theta range 133 to 141 degrees and incidence angles as described in table 2.1, section 4.2.3.

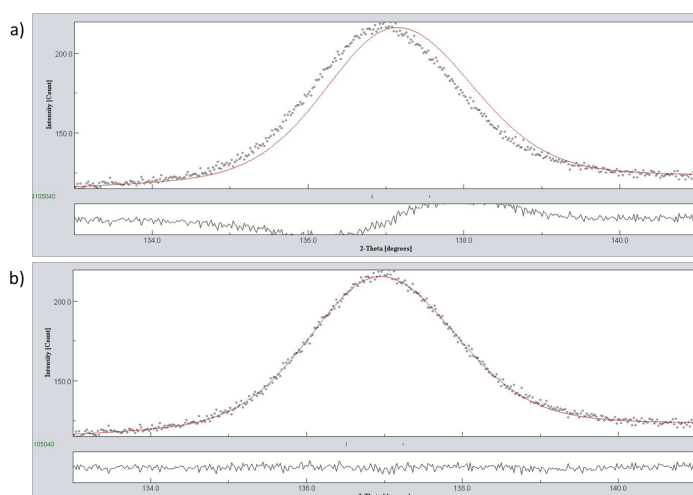


Figure 3.6: Peak at 137 prior (a) and after (b) compensating for the lattice distortion caused by residual stresses

3.2.3 FIB-DIC analysis

FIB-DIC analysis was conducted on the cross-section of the shot-peened sample applying the methodology described in chapter 2.3.

Ring-cores have been milled in the cross-section at $100\ \mu\text{m}$, $200\ \mu\text{m}$, $300\ \mu\text{m}$, $600\ \mu\text{m}$ and $1000\ \mu\text{m}$ from the shot-peened surface. A minimum of 5 ring-cores have been performed for each location.

An example of the strains obtained by DIC analysis for a single ring core can be seen in figure 3.7, where the measured strain is plotted against the milling depth.

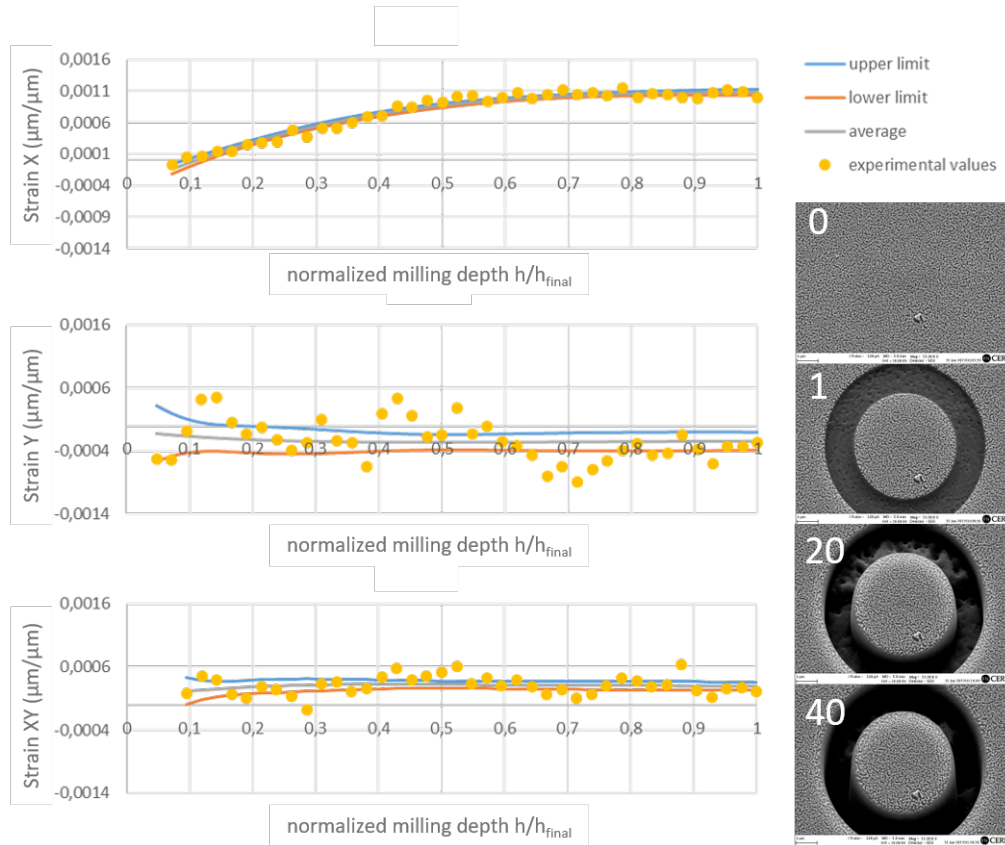


Figure 3.7: Recorded strain (ϵ) from DIC tracking in the 3 in-plane directions. In ring-core analysis, X direction is considered parallel to the shot-peened surface and Y direction is considered orthogonal to the shot-peened plane. Result presented over the normalized milling depth.

The residual stresses are present mostly in the direction parallel to the shot-peened surface (X). No relevant strain relaxation recorded in the transverse direction (Y) have been recorded.

The residual stress values obtained from each of the ring cores are plotted against the distance from the shot peened surface in figure 3.8.

The recorded scattering is most likely due to differences in residual stresses present in the different grains as the scale of the technique is smaller than the average grain size in the material, as it is the case for the depth of 200 μm .

A further indication that the scatter in the data is due to actual differences within the material rather than errors of measurement is given by the fact that the recorded scatter seems to be lower as the recorded stresses approach the yield value of the material.

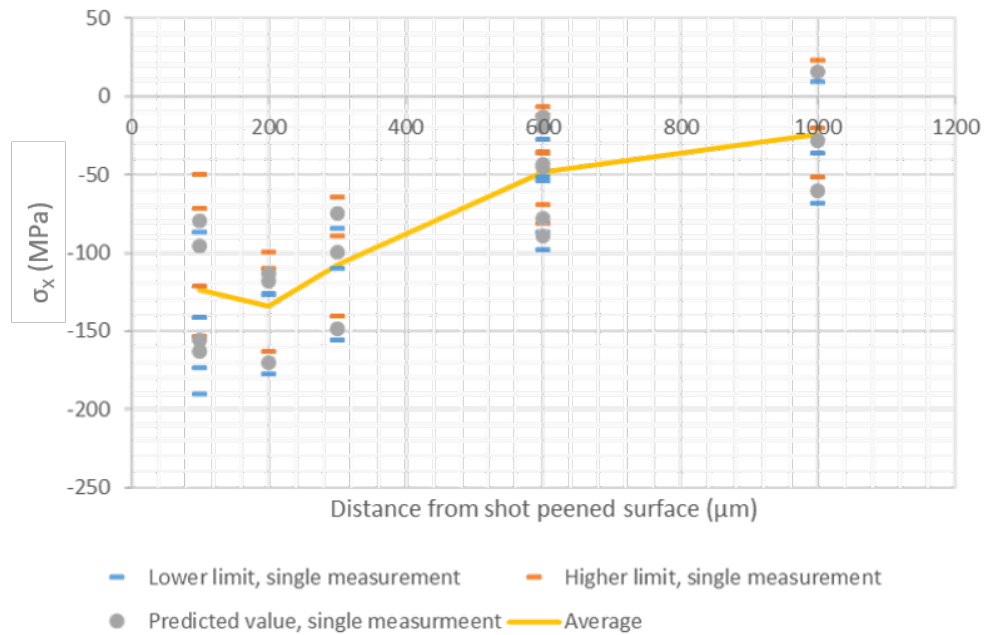


Figure 3.8: FIB-DIC analysis of shot-peened aluminum sample. Recorded stresses in the X direction in the plane stresses condition (prior to cross section compensation)

It is important to note that the stresses in figure 3.8 are obtained in plane stress condition, considering the cross-sectional plane. The stresses in the direction normal to the perpendicular cross-sectional plane were removed by the cross-sectioning process by the creation of a free surface.

As known from the theory, and confirmed by both the XRD and the macroscopic hole drilling techniques, the residual stresses obtained from shot peening are expected to be biaxial.

As a consequence, the stress component revealed by the cross section operation (out-of-plane Z in the frame of reference selected for FIB-DIC analysis) is

not negligible, as it is expected to have the same magnitude as the the stresses recorded in the direction parallel to the shot peened surface (X direction is the selected frame of reference for the analysis).

After taking into account the mentioned out-of-plane component the residual stresses present before the sectioning can be estimated, and are presented in figure 3.9.

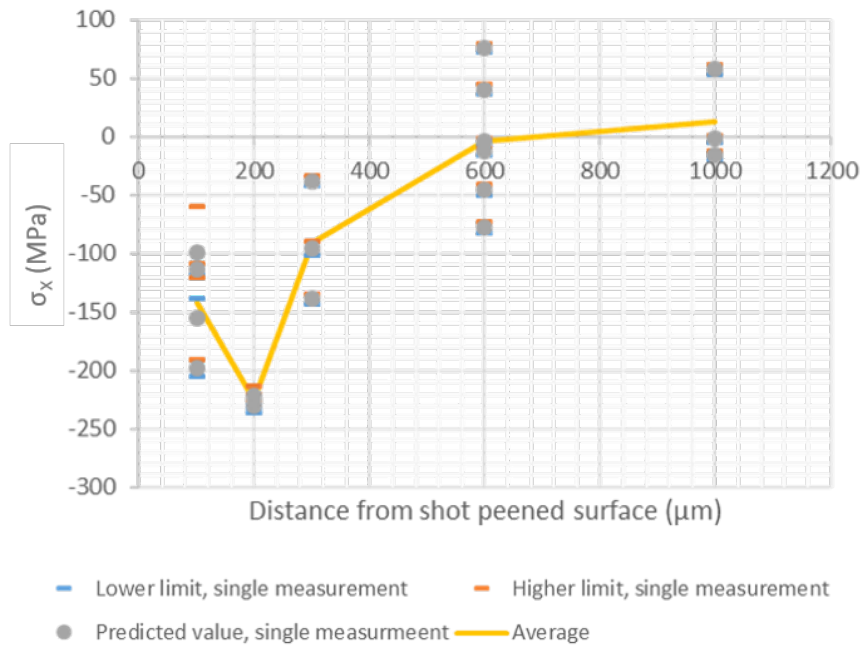


Figure 3.9: FIB-DIC analysis of shot-peened aluminum sample. Recorded stresses in the X direction in the plane strains condition after cross sectioning effect compensation

3.3 Discussion

The residual stresses obtained by the three techniques are compared in figure 3.10. The measurements obtained by the three technique are in good agreement, with deviations within $\pm 75 \text{ MPa}$.

The relative error between measurements is in the same order of magnitude of the one obtained in similar studies, where different technique of residual stresses are evaluated and copared. As an example, in [36], strain-gage hole drilling, ESPI (Electronic Speckle Pattern Interferometry) hole drilling and X-ray diffraction methods have been applied to un-blasted and blasted samples of carbon steel. The results obtained show similar variation between the techniques.

In conclusion, the FIB-DIC methodology applied to residual stresses evaluation in cross-sectioned sample can be considered validated, and the know-how gained can be safely transferred to the residual stresses evaluation in the BDF prototypes.

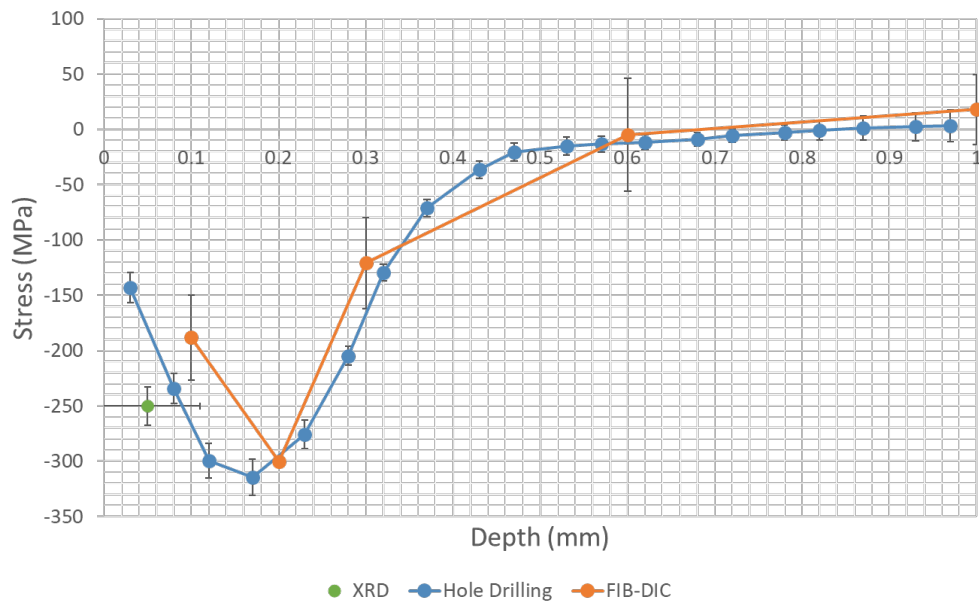


Figure 3.10: Residual stresses as determined by macroscopic hole drilling (blue), XRD analysis (green) and FIB-DIC analysis (orange). The vertical error bar is determined by the standard deviation between the measurements. The horizontal error bar in the XRD measurement determine the gauged volume by the technique.

Residual stresses analysis in BDF prototypes

This section presents the residual stress measurements on Ta and Ta2.5W clad fabricated for the BDF target prototype.

4.1 Prototype description

As mentioned in the introduction, section 1.1.4, the beam target design proposed for the new BDF facility consist of 18 co-linear plates of cylindrical shape of 250 mm in diameter and variable thickness aligned to form an assembly of 1.3 m of length. The first plates are constituted of TZM alloy, whereas the last are constituted of Tungsten. All the plates are clad with an uniform layer of 1.5 mm of tantalum or Ta2.5W alloy to better cope with erosion-corrosion phenomena.

As part of the preliminary studies for the BDF target design, a scale replica of the target has been manufactured to test production methods and behaviour of the materials, also under irradiation conditions.

The produced prototype has the same length as the suggested design but reduced diameter of 80 mm. Some of the 80 mm blocks produced have been allotted for residual stresses evaluation. The blocks selected for the residual stresses analysis are the #14 and #18. The #14 is constituted by a TZM core clad with Ta2.5W. The #18 is constituted by a W core clad with Ta, as illustrated in table 4.1. Technical drawings as supplied to the contractor are provided in appendix E.

ID	Core material	Clad material	Diameter	Length	Weight
#14	TZM	Ta2.5W	80 mm	25 mm	1.5 kg
#18	W	Ta	80 mm	50 mm	3.8 kg

Table 4.1: Sample id, dimensions and constituent material of the prototypes utilized in the presented analysis

4.1.1 Materials properties

The materials selected for the BDF target are high density refractory metals, selected for their high melting point, high radiation resistance and low coefficient of thermal expansion.

The CTE of Ta, Mo and W is plotted in function of temperature in figure 4.1a, whereas in figure 4.1b the elastic modulus of the same materials plotted against the temperature.

For the cladding, Tantalum was selected due to its outstanding corrosion resistance, also in presence of radiation and for its complete compatibility with W and Mo, as can be seen in the corresponding phase diagrams in figure 4.5.

Recrystallization temperature and yield strength of Ta with the temperature, important for the determination of the HIP cycle parameters, is reported in figure 4.2 and 4.3 respectively.

All the materials involved in the construction of the BDF prototypes are undergoing extended chemical, mechanical and thermo-physical characterization by Fraunhofer and Branch Lab Dresden in Germany, as well as internally at CERN labs. Detailed materials characterization campaign is ongoing, and will be published as part of the output of the Comprehensive Design Phase of the BDF.

	Sample #14		Sample #18	
	Ta2.5W	TZM	Ta	W
E [<i>GPa</i>]	186	310	182	400
ν	0.28	0.33	0.28	0.28
CTE [μK^{-1}]	6.5	5	6.6	4.4
Yield [<i>MPa</i>]	270	480	200	-
UTS [<i>MPa</i>]	-	-	-	560

Table 4.2: Relevant materials properties of the tested prototypes. Data at 22°C.

The density of Ta, relevant for the determination of X-ray penetration and influencing the FIB milling rate, is $16.7 \frac{g}{cm^3}$.

The penetration depth of the X-rays into tantalum was calculated with the software AdsorbX for the beam and material combination. Absorption rate in function of the depth is presented in figure 4.4, where is shown that 90% of the signal is coming from the first 1.589 μm .

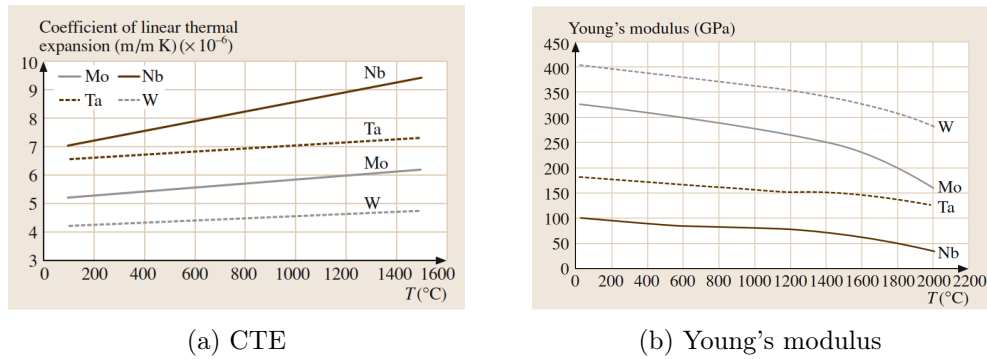


Figure 4.1: Variation with the temperature of coefficient of linear thermal expansion (a) and Young's modulus (b) for molybdenum, tungsten, niobium and tantalum materials, as reported in [37]

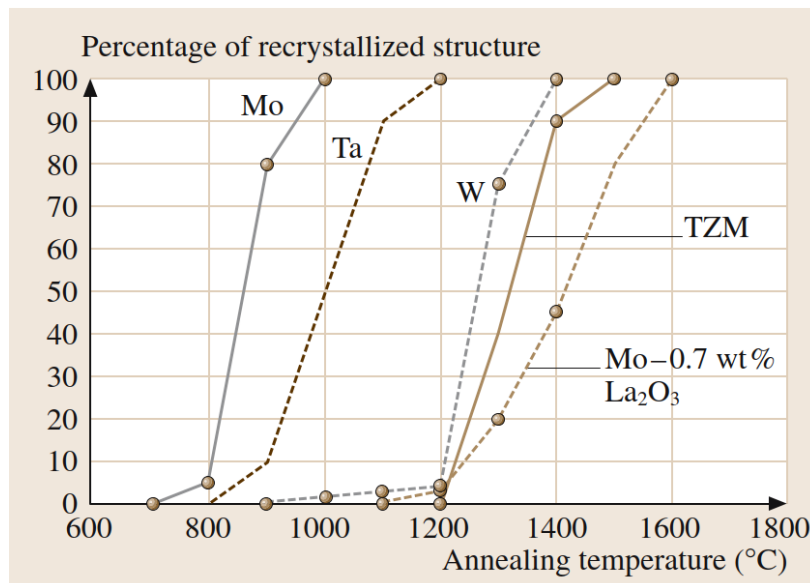


Figure 4.2: Fraction of recrystallized structure versus annealing temperature, setting an annealing time of 1h for metal sheets of 1 mm of thickness. Data as reported in [37]

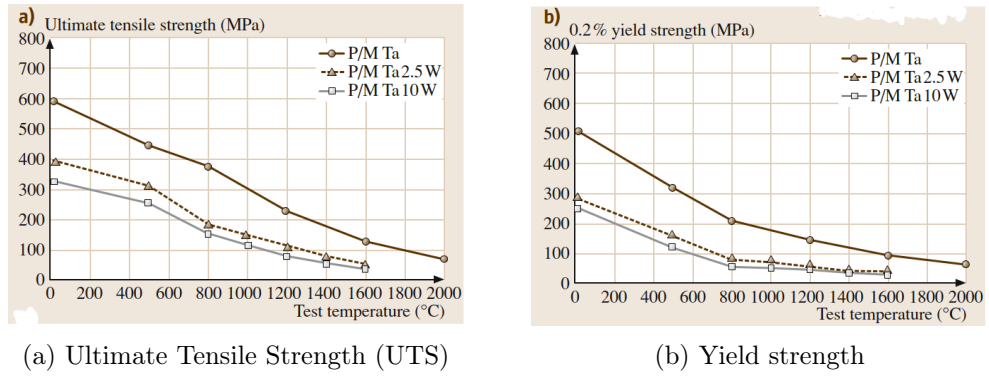


Figure 4.3: Ultimate Tensile Strength (a) and Yield strength (b) in function of temperature for various Ta alloys, as reported in [37]

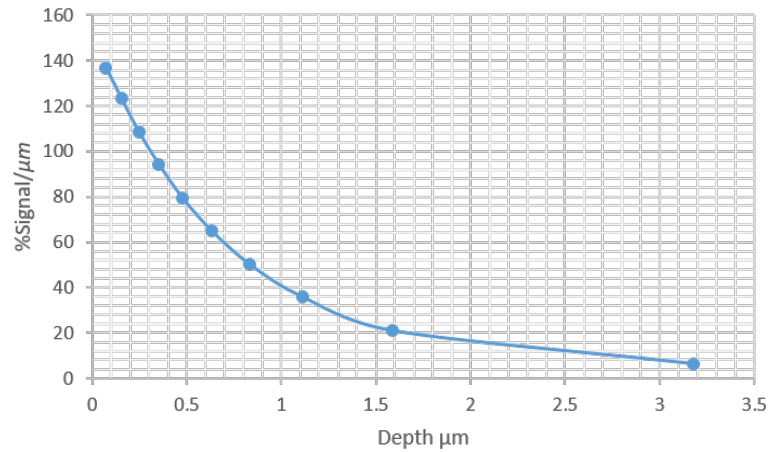
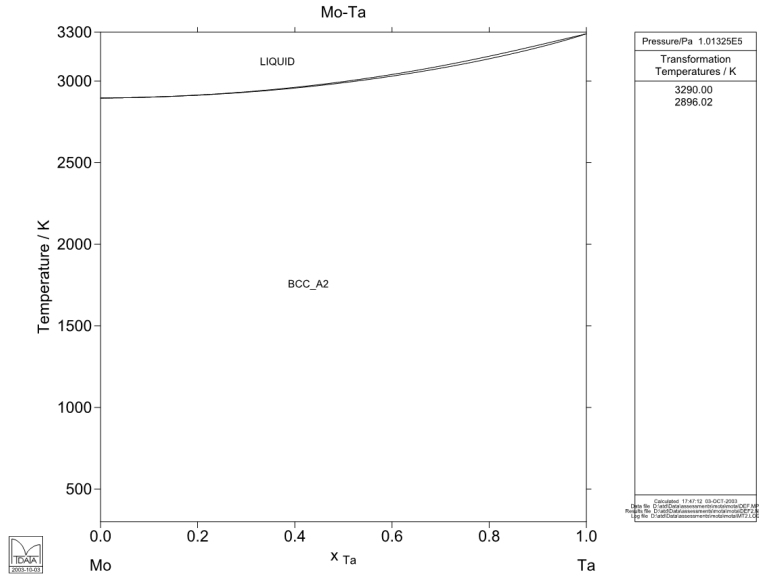
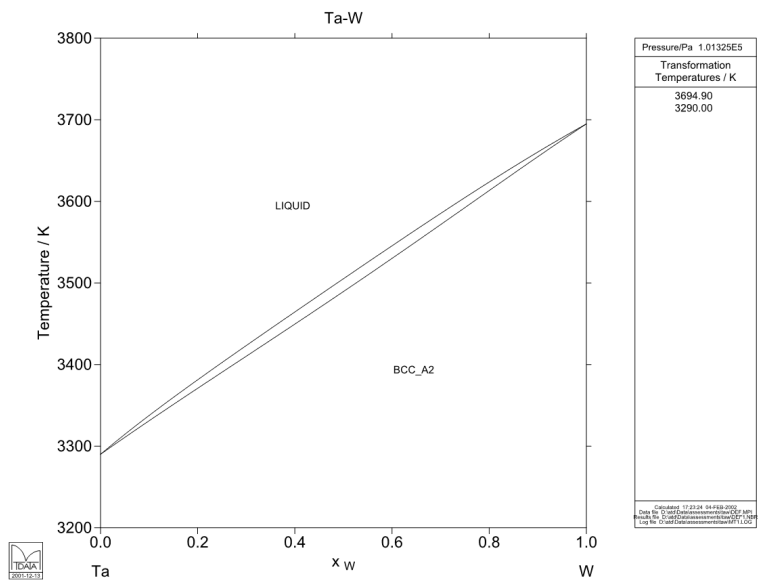


Figure 4.4: X-rays penetration in tantalum as calculated for the used X-ray source and angle combination. 90% of the signal is coming from the first 1.589 μm



(a) Mo-Ta



(b) Ta-W

Figure 4.5: Phase diagram of binary alloys Mo-Ta (a) and Ta-W (b) as calculated by MTDATA [38, 39]

4.1.2 Production process (HIP)

The HIP process of the BDF target prototypes was performed by HIP PM Volker in Germany.

Temperature of 1200°C and pressure of 150 MPa have been maintained for 180 min. The heating rate applied was 3-5 K/min and the cooling rate is reported to be lower than 3 K/min. Temperature and pressure measured during HIP process of the analyzed prototypes are provided in figure 4.6.

Tantalum is reported to fully recrystallize after 1h at 1200°C [37].

As the HIP temperature is higher than the recrystallization temperature of Ta, all the stresses present in the material prior to the HIP process are considered fully relieved by the thermo-mechanical process.

Ta has high solubility and affinity for nitrogen and oxygen at high temperature. To avoid absorption of those gasses, the HIP process was performed in Ar atmosphere. Samples are covered by a zirconium foil getter, added to absorb the residual oxygen in the argon atmosphere at HIP temperature, and are placed in alumina crucibles, as visible in figure 4.7. A molybdenum heater has been employed to prevent any carbon contamination of the atmosphere.

During HIP, the core material is encapsulated in a continuous hermetic cladding capsule obtained by electric welding in void two plates and a tube built with tight tolerances (zero-gap between core and clad between $100\ \mu\text{m}$ and $200\ \mu\text{m}$, as indicated in the drawings presented in appendix E). An example of the components prior to assembly and welding is provided in figure 4.8.

The continuity of the cladding is crucial, as any infiltration of gas between between the cladding material and the target cylinder would equalise pressure in both sides of the cladding material and cancel the applied pressure towards the target. To improve the reliability of the welding process, welding lips have been introduced to the design by the company .

After HIP process, the welding lips are removed by machining, and the overall dimensional accuracy of the sample is ensured by light turning operation. An example of a sample prior and after turning operation is provided in figure 4.9.

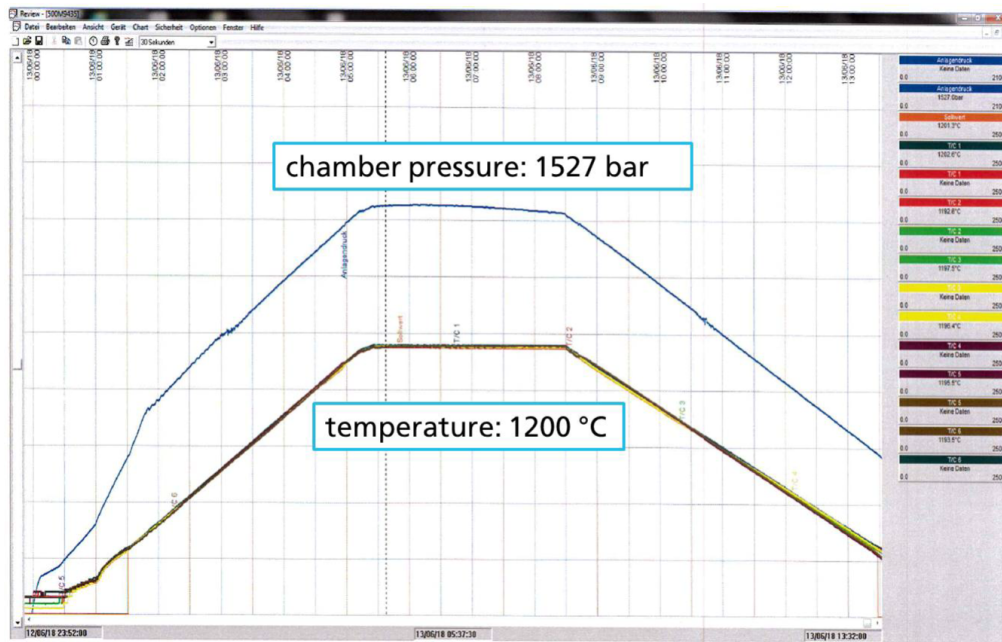


Figure 4.6: Pressure and temperature recorded during HIP production cycle of the BVF targhet prototypes. Heating rate of 3-5 K/min. The temperature of 1200°C and pressure of 150 MPa have been maintained for 180 min, cooling rate < 3 K/min.

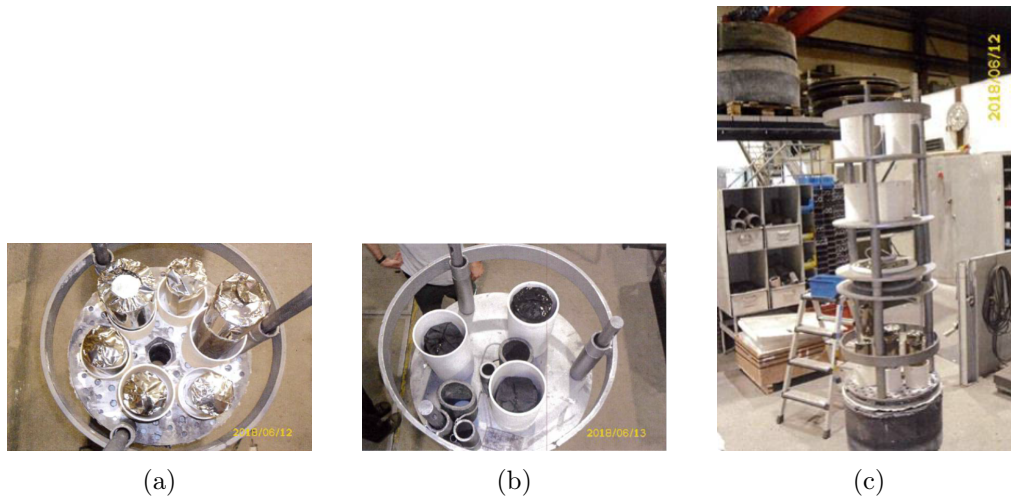


Figure 4.7: Different capsules enveloped in zirconium foils and placed in alumina crucibles prior (a) and after (b) HIP process and support frame filled with all capsules and plates at the HIP PM Volker facility (c)

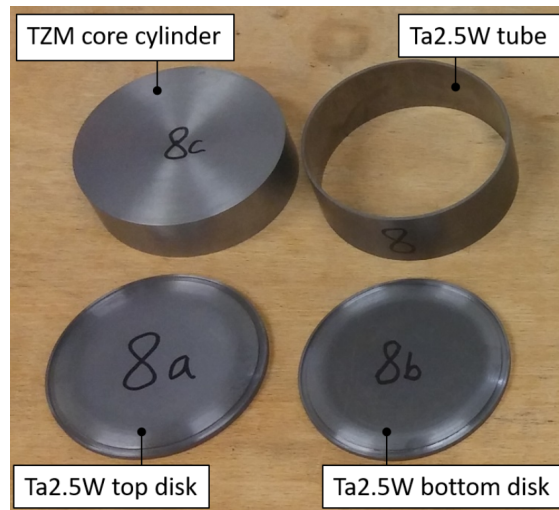


Figure 4.8: Refractory metal parts required for the production of an 80 mm diameter, 25 mm thick Ta2.5W-clad TZM target block for the BDF target prototype



(a) After HIP



(b) After machining

Figure 4.9: Example of BDF prototype samples after HIP process and after machining performed by HIP PM Volker prior to shipping

4.1.3 Sample extraction and workplan

As with the aluminium samples, residual stresses are evaluated using macroscopic hole drilling, XRD analysis and micro-ring-core-milling.

Prior to any other analysis or sectioning on the prototype, a macroscopic hole have been drilled 8 mm from the centre of the pristine sample.

To respect the size and weight limitations for XRD and FIB analysis, the prototypes have then been sectioned as illustrated in figure 4.10.

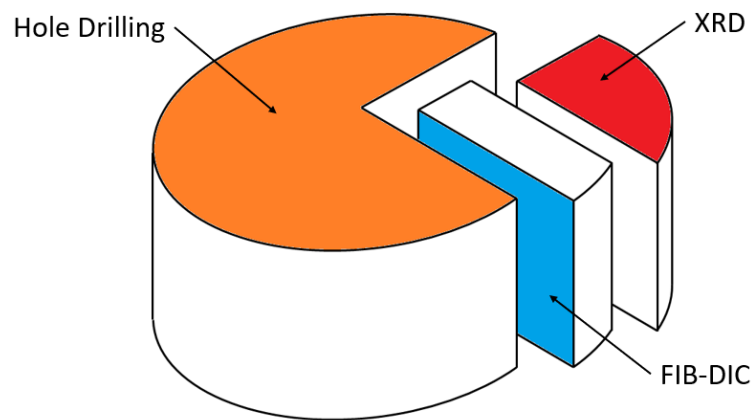


Figure 4.10: Sectioning plan for the BDF target prototypes

First, electrical Discharge Machining (EDM) have been employed to cut a quarter of the sample (red lines in figure 4.11). Then, faster high-speed SiC machining method have been employed to release the cross-section to be used in the FIB and to obtain the part to be fitted in the XRD sample holder (blue lines in figure 4.11).

EDM technique have been selected to minimize residual stresses induced by machining and sample preparation operations on the cross-section to be analyzed by FIB-DIC technique. Where induced residual stresses are not of concern, more conventional and fast SiC disk cutting have been employed. Picture of the samples after sectioning are presented in figure 4.11. The EDM cutting path have been selected to cross the blind hole produced during the macroscopic hole drilling determination of the residual stresses, to check for dimensional accuracy.

4.1.4 Mechanical and chemical polishing

To be able to correctly perform the FIB milling and XRD analysis, the surface of the sample must be flat with low roughness.

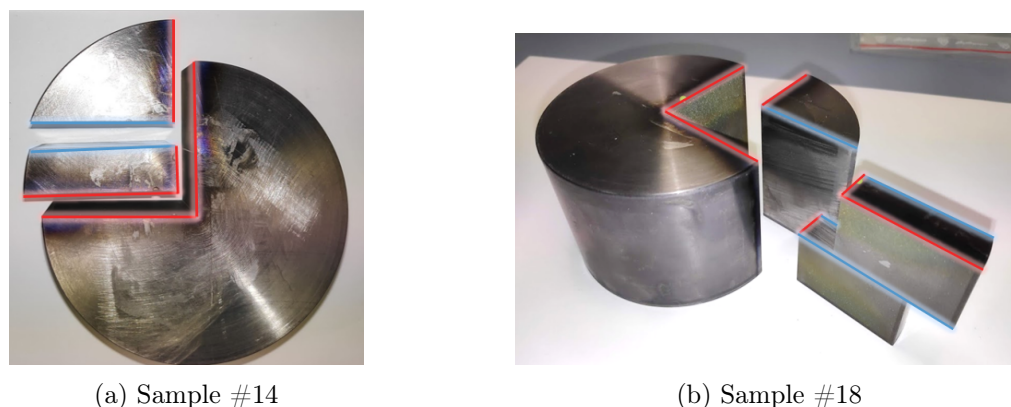


Figure 4.11: Sample #14 and #18 after sectioning. Red lined highlight surfaces cut through EDM, blue lines represent surfaces cut with SiC blade.

Surface preparation might significantly change the residual stress state of the surface due to the combined effect of the removal of the surface layer and the building up of eigenstrain due to the mechanical operation.

To minimize sample preparation effect, the chemical-mechanical preparation applied recipe illustrated in table 4.3 have been followed.

Very fine 1200 GRT grinding paper has been chosen as starting point, and intermediate etching steps are introduced following a recipe known to produce good results in EBSD analysis of Ta.

Purely chemical polishing has been adopted starting from the 8th step. The acid mixture adopted for the scope follows the recommendations from standard ASTM E407 [40] and consists in a mixture of 30 ml HNO_3 , 30 ml HCl and 15 ml HF . Handling concentrated HF acid is dangerous and requires special training as it can be adsorbed through the skin and cause cardiac arrest [41]. Moreover concentrated HF can chemically attach glass, and therefore plastic equipment has to be used. A picture of the setup used during the etching is visible in figure 4.13a.

By microscopy imaging, the amount of material removed only during the last chemical polishing step #9 to #11 is estimated to be approximately $50 \mu m$.

The chemical polishing step is considered enough to remove the affected layer by the mechanical preparation¹.

XRD analysis has been conducted on the surface of the cladding of the sample

¹. The affected layer from mechanical polishing is normally estimated to be in the order of 3 times the polishing particle size. The coarser of the polishing steps adopted is 1200 GRT, corresponding to a particle size of about $15 \mu m$, therefore the affected layer should not exceed $45 \mu m$. Considering the subsequent mechanical steps adopted, this estimation is a very conservative estimation.

Step	Size	Time	# Rep.	Total time	Force	Lubricant
1	1200 grt SiC paper	5 min	20	100 min	50 N	Water
2	1 min etching with HNO ₃ -HCl-HF solution (60-40-10)					
3	3 um honeycomb	10 min	5	50 min	60 N	Water
4	1 min etching with HNO ₃ -HCl-HF solution (60-40-10)					
5	3 um diamond suspension	5 min	5	25 min	60 N	Specific
6	1 min etching with HNO ₃ -HCl-HF solution (60-40-10)					
7	Colloidal silica + 5% H ₂ O ₂	15 min	1	15 min	60 N	none
8	3 min etching with HNO ₃ -HCl-HF solution (60-40-10)					
9	5 min etching with HNO ₃ -HCl-HF solution (30-30-15)					
10	30 min etching with HNO ₃ -HCl-HF solution (30-30-15)					
11	30 min etching with HNO ₃ -HCl-HF solution (30-30-15)					

Table 4.3: Polishing recipe adopted for the surface preparation for FIB-DIC and XRD analysis.



(a) Before



(b) After

Figure 4.12: Cross-section of the sample #18 prior (a) and after (b) the chemical-mechanical preparation reported in table 4.3.

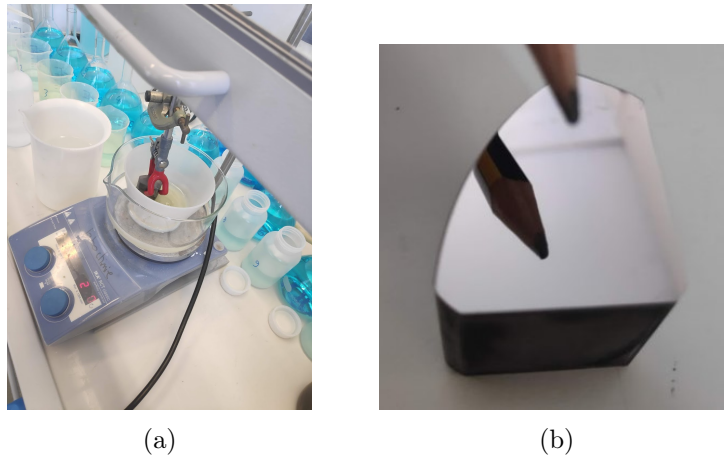


Figure 4.13: Setup used for the steps #9, #10 and #11 of the final chemical attach reported in table 4.3 (a) and shining mirror-like surface obtained on the XRD surface of the sample #18 (b)

BDF #14 and BDF #18 in the as-received state and after step #7, #8, #9, #10 and #11 of the chemical-mechanical preparation in table 4.3.

FIB-DIC analysis has been performed after step #7, #10 and #11 of the chemical-mechanical preparation in table 4.3 for the cross-section of the sample BDF #14 and after step #10 and #11 in the cross-section of the sample BDF #18. FIB-DIC analysis has also been performed on the same plane used for the XRD analysis in the sample BDF #14 after polishing step #10 and #11.

4.2 Residual stresses analysis

Results of the residual stresses analysis performed are presented in the following sections.

4.2.1 Preliminary FEM simulations

Before proceeding with the experimental analysis, FEM simulations of the residual stresses due to CTE mismatch have been run.

In the simulation, the two examined prototypes have been modelled with ANSYS software. The modelled geometry is the one presented in appendix E, and the material properties applied are the ones presented in table 4.2.

Clad and core material are assumed to lock-in at $500\text{ }^{\circ}\text{C}$. The temperature is then lowered to $22\text{ }^{\circ}\text{C}$ and the stresses generated by the different CTE and elastic modulus of the joined materials is evaluated. The lock-in temperature of $500\text{ }^{\circ}\text{C}$

has been chosen in accordance with what has been determined experimentally in a similar setup involving the same material and similar HIP cycle by Wilcox et al. for the ISIS palliation target [23].

From the simulations, the expected stresses in the clad are in the order of 100 MPa tensile in the sample #14 and 250 MPa tensile in the sample #18. The obtained stress field is presented in figure 4.15 and 4.16 .

Distant from edge effects, stresses are expected to be uniform among the depth of the clad and reach a stable maximum value after 15 mm of distance from the edge of the sample. The computed stress on the surface of the clad are plotted in figure 4.15c and 4.16c for the sample #14 and #18 respectively.

As the samples are axial-symmetric, the stresses in figure 4.15 and 4.16 have been calculated on a 2-D model with the appropriate constrains applied.

A proper 3-D simulation with a lower number of polygons have been run to check the influence of the cross-sectioning on the distribution of residual stresses, and is shown in figure 4.14. The obtained results are consistent with the theoretical expression derived in section 2.3.5.

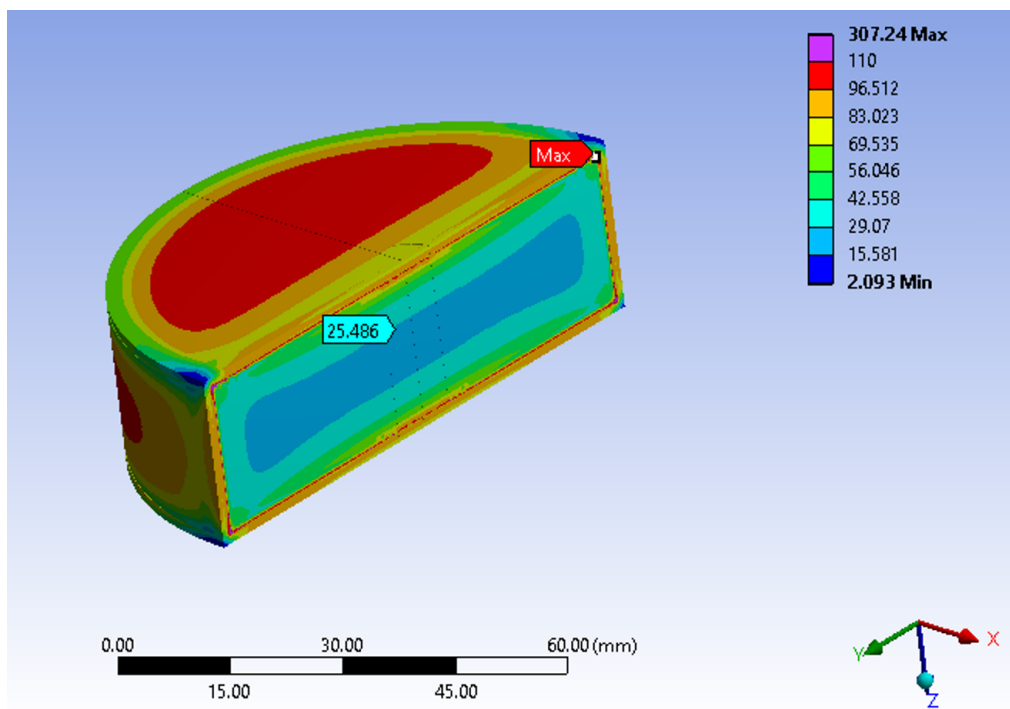
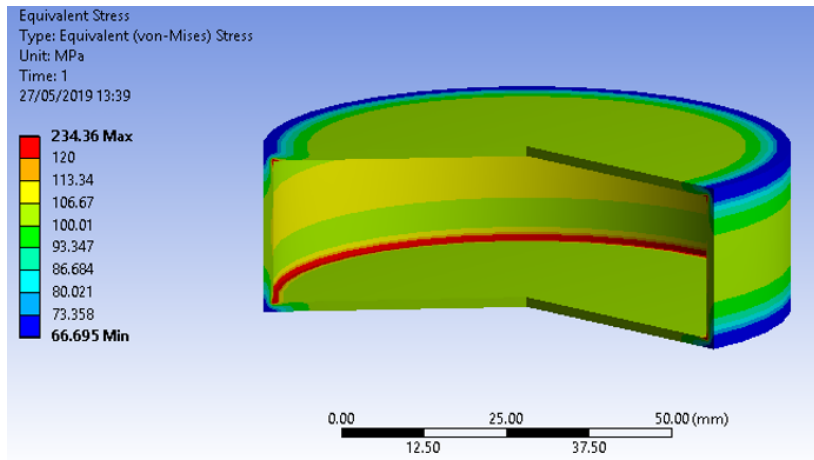
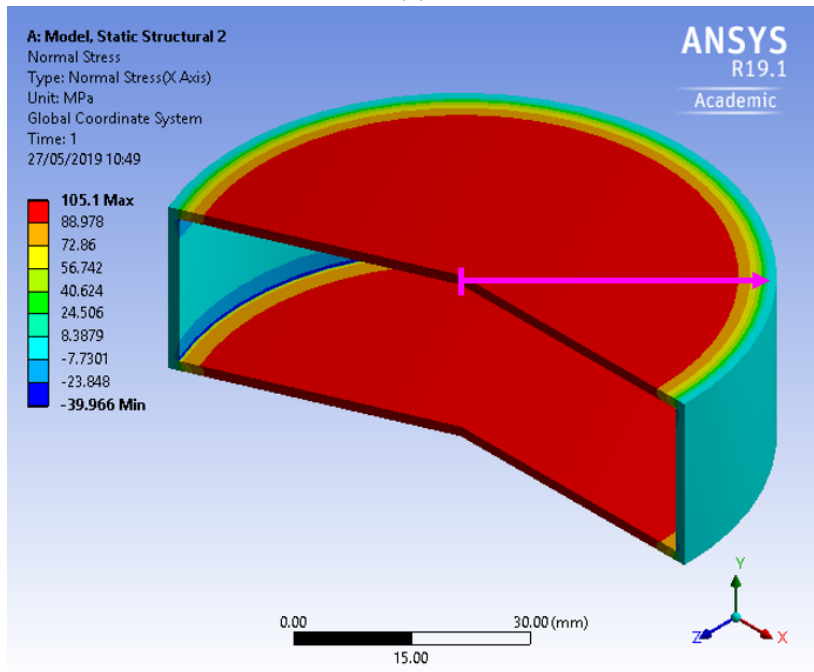


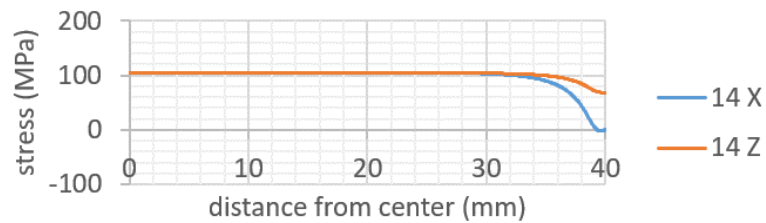
Figure 4.14: Effect of cross-sectioning on the distribution of residual stresses simulated with ANSYS. In this example, BDF prototype #14, which will be presented in chapter 4, has been used.



(a)

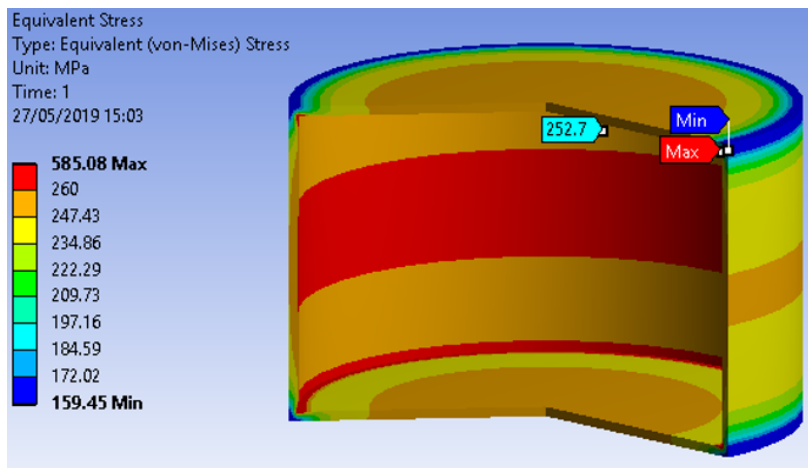


(b)

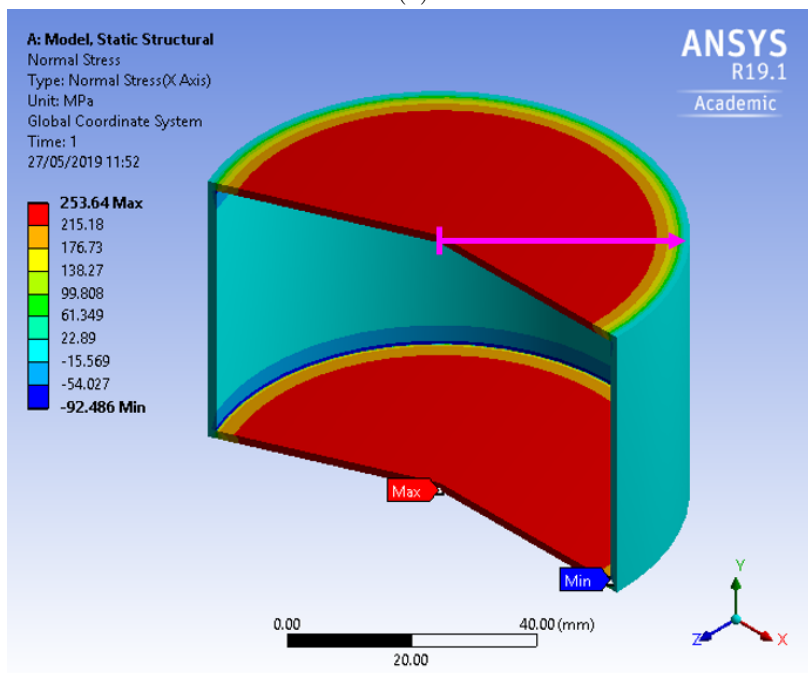


(c)

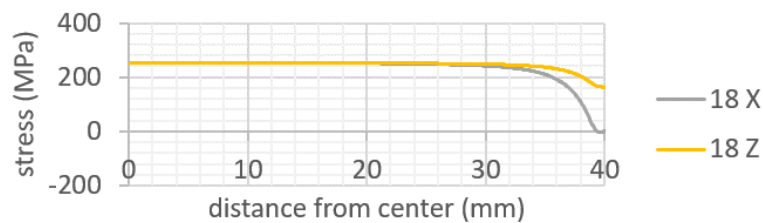
Figure 4.15: Von Mises (a) and radial (b) stresses in the clad material of the sample BDF #14 obtained by FEM simulation. In figure (c) the stresses in the x (radial) and z (circumferential) directions present on the top surface of the clad are plotted.



(a)



(b)



(c)

Figure 4.16: Von Mises (a) and radial (b) stresses in the clad material of the sample BDF #18 obtained by FEM simulation. In figure (c) the stresses in the x (radial) and z (circumferential) directions present on the top surface of the clad are plotted.

4.2.2 Macroscopic hole drilling

Hole drilling was performed at 8 mm from the geometric center on the top surface of the BDF prototypes #14 and #18 prior to sample sectioning or any other surface preparation.

The same parameter used for the hole drilling on aluminium sample were employed. However, it was not possible to obtain the same dimensional accuracy, as already shown in the methodology chapter 2.1, figure 2.2c and 2.2b.

Results from macroscopic hole drilling for the sample #14 and #18 are presented in figure 4.17a and 4.17a respectively. The measured residual stresses are in the order of 0 MPa,-200 MPa for the BDF prototype #14 and 0 MPa,-100 MPa for the BDF prototype #18 at 50 μm from the top surface of the clad.

For higher depths the residual stresses tend to move towards the tensile region, but seen the difficulty encountered in the drilling and the poor geometric consistency obtained, the results can only be considered qualitatively.

4.2.3 XRD

XRD analysis have been conducted on the cladding area indicated in figure 4.10. A picture of the setup is provided in figure 2.7 in the methodology section .

Tantalum has body-centered cubic (BCC) structure and lattice constant of 0.33058 Å. Similar to aluminium, Tantalum also presents a peak at around $2\theta = 138^\circ$, compatible with the requirements discussed in section 4.2.3.

As tested with the aluminium, multiple scans have been performed at the angles indicated in section 4.2.3 table 2.1, in the 2θ range of 136° to 141° .

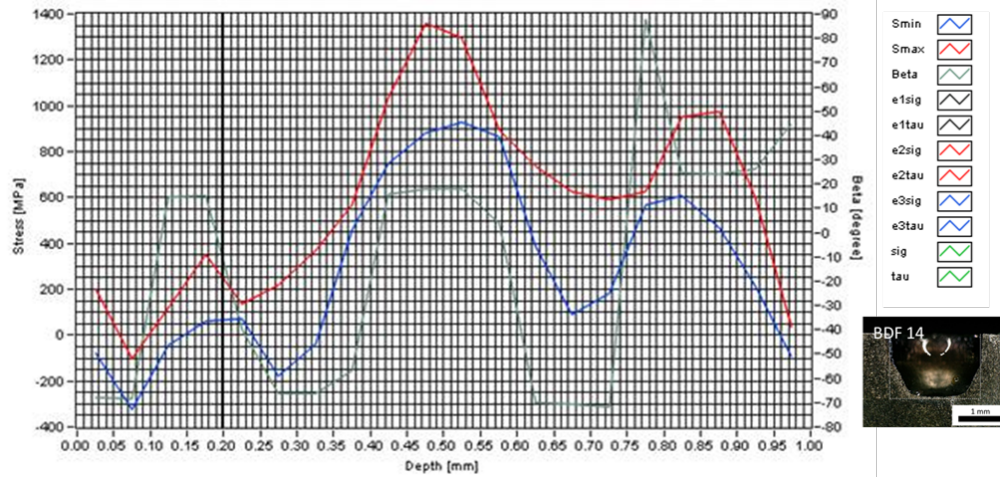
As tested with the aluminium, 27 scans have then been performed for each measurement at the angles indicated in table 2.1 section 4.2.3, in the 2θ range of 136° to 141° . An example of the recorded peaks is presented in figure 4.18.

Data have been acquired at different stages of the surface preparation.

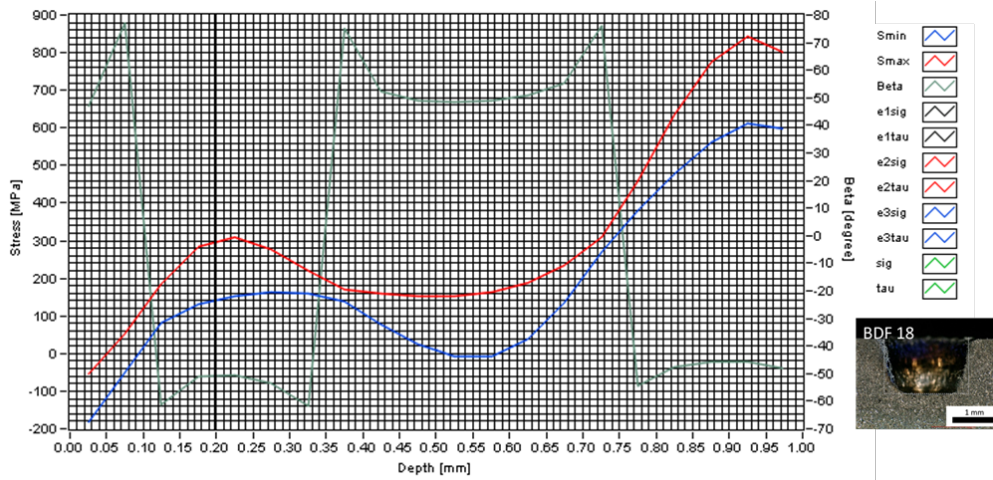
The residual stresses are calculated from the shift in peak with the " $\sin^2 \psi$ " method reported in section 4.2.3.

Acquired data is presented in figure 4.20 and figure 4.21 for the BDF prototype sample #14 and #18 respectively.

Results obtained from the analysis are very inconsistent, but overall the residual stresses found by the technique seems to be the compressive region, approximately oriented in radial direction and with magnitude between 50 MPa and 200 MPa.



(a) BDF #14



(b) BDF #18

Figure 4.17: Residual stresses calculated from with hole drilling technique for the BDF prototype #14 (a) and #18 (b). Due to the poor dimensional accuracy the results can only be trusted qualitatively and only for smaller depths.

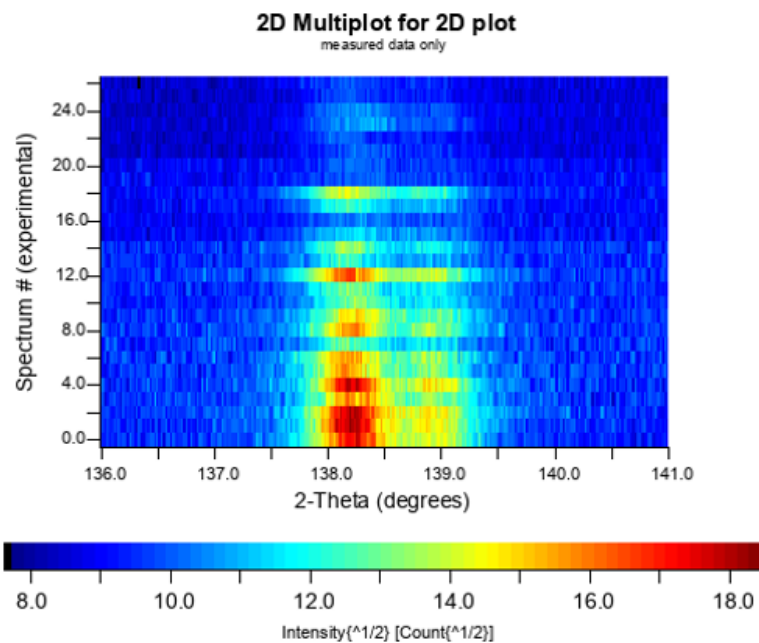


Figure 4.18: Example of XRD scan in the 2theta range 136° to 141° and incidence angles as described in table 2.1, section 4.2.3 (BDF #14 after 30 minutes chemical etching).

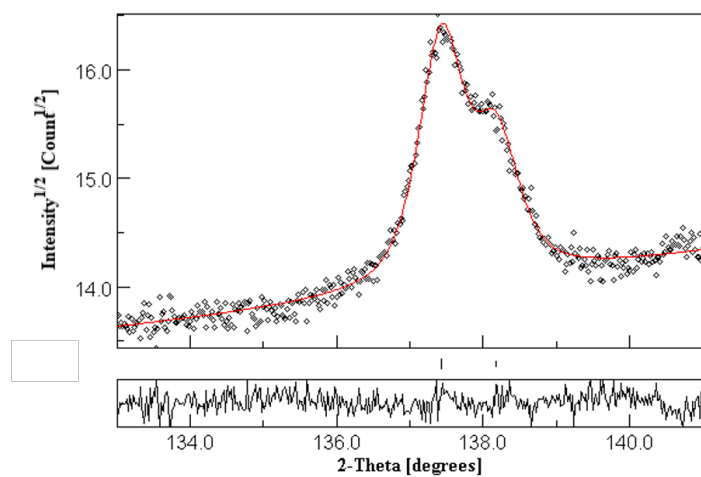
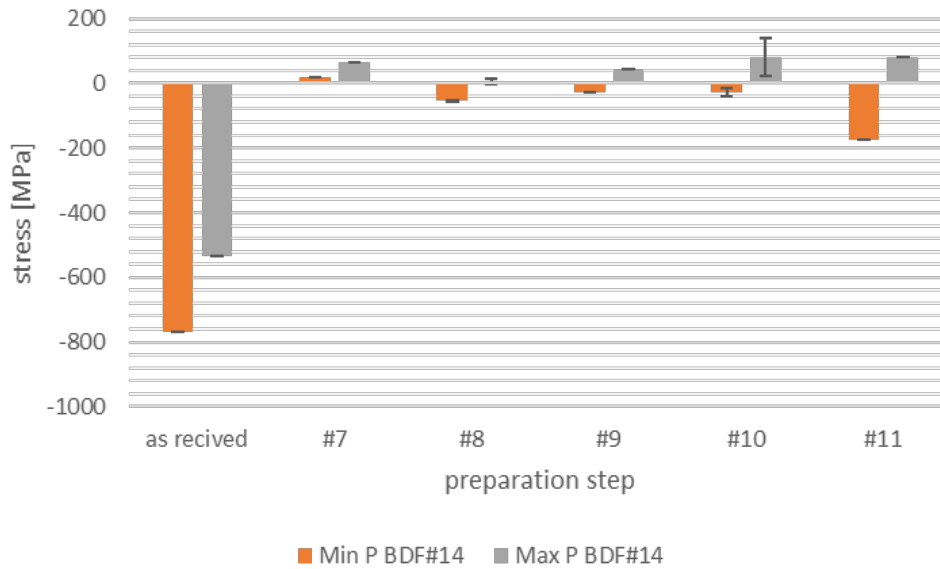


Figure 4.19: Example of one of the XRD scans on tantalum.

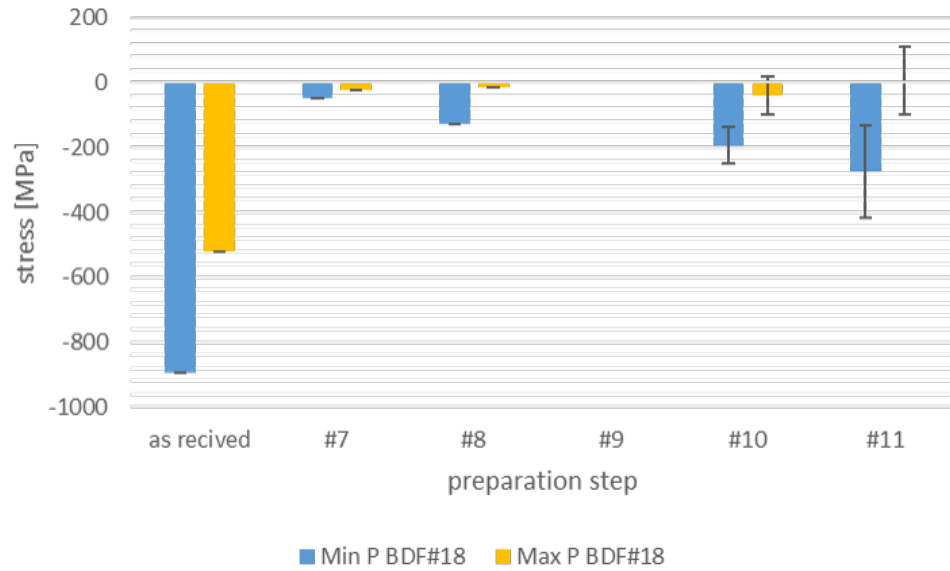


(a) BDF #14

Prep. Step	Min P [MPa]	Max P [MPa]	St dev Min P	St dev Max P	n meas
as recived	-769.4	-532.8	-	-	1
#7	17.4	63.8	-	-	1
#8	-54.6	5.8	2.2	8.5	2
#9	-26.4	43.7	-	-	1
#10	-27.7	80.6	12.5	58.1	3
#11	-175.1	79.1	-	-	1
#7 to #11	-47.0	55.0	53.3	47.2	8

(b) BDF #14

Figure 4.20: XRD measurement of Min and Max principal stresses in the BDF prototype #14 at different stages of surface preparation. Preparation step in reference to table 4.3. "n meas" indicate how many times the measurement has been repeated. Standard deviation is provided when applicable.



(a) BDF #18

Prep. Step	Min P [MPa]	Max P [MPa]	St dev Min P	St dev Max P	n meas
as received	-891.7	-523.3	-	-	1
#7	-50.6	-24.3	-	-	1
#8	-129.6	-16.1	-	-	1
#10	-193.9	-39.1	55.6	59.0	2
#11	-274.8	4.7	142.8	103.4	11
#7 to #11	-190.9	-4.5	110.2	76.0	15

(b) BDF #18

Figure 4.21: XRD measurement of Min and Max principal stresses in the BDF prototype #18 at different stages of surface preparation. Preparation step in reference to table 4.3. "n meas" indicate how many times the measurement has been repeated. Standard deviation is provided when applicable.

4.2.4 FIB-DIC analysis

FIB-DIC analysis has been performed on the cross-section of the analyzed BDF target prototypes as indicated in figure 4.10 - section 4.1.3, by applying the methodology described in chapter 2.3.

Ring-cores were milled in the Ta clad at distance of about 750 μm from the clad surface and 15 mm from the center of the target.

An example of the strains obtained by DIC analysis for a single ring core can be seen in figure 3.7, where the measured strain is plotted against the milling depth.

Results are presented in table 4.23b and 4.23c for the BDF prototype #14 and #18 respectively. In the table, "n meas" indicate how many times the measurement has been repeated. The number in brackets indicate the total number ring-core milled, whereas the number outside the brackets indicate the tests where the DIC processing converged to a stable solution.

The analysis has been repeated at different stages of surface preparation, in reference to table 4.3 in section 4.1.3.

The results are highly scattered (standard deviation up to 100 MPa), but an uniaxial compressive state of about -100 MPa seems to be present in both the samples analyzed. No significant tensile values have been recorded. The measured compressive stresses are oriented parallel to the clad (X direction), with the recorded principal angle between $\pm 30^\circ$.

To directly compare the result of micro ring-core milling with the ones from XRD, several measurements have been also performed on the surface of the sample #14 analyzed by X-ray diffraction (Red surface in figure 4.10, section 4.1.3).

The results are presented in table 4.24c, and show once more uniaxial compressive state in radial direction of about $\sim 120 \text{ MPa}$ in magnitude and standard deviation of $\sim 65 \text{ MPa}$.

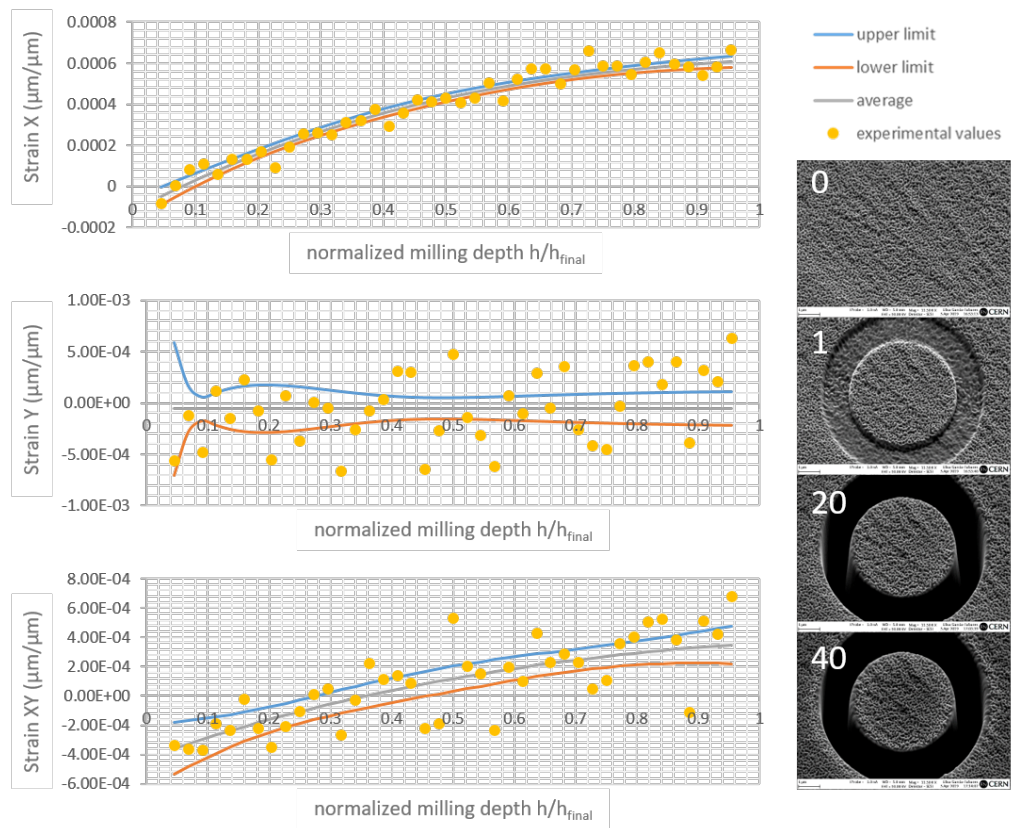
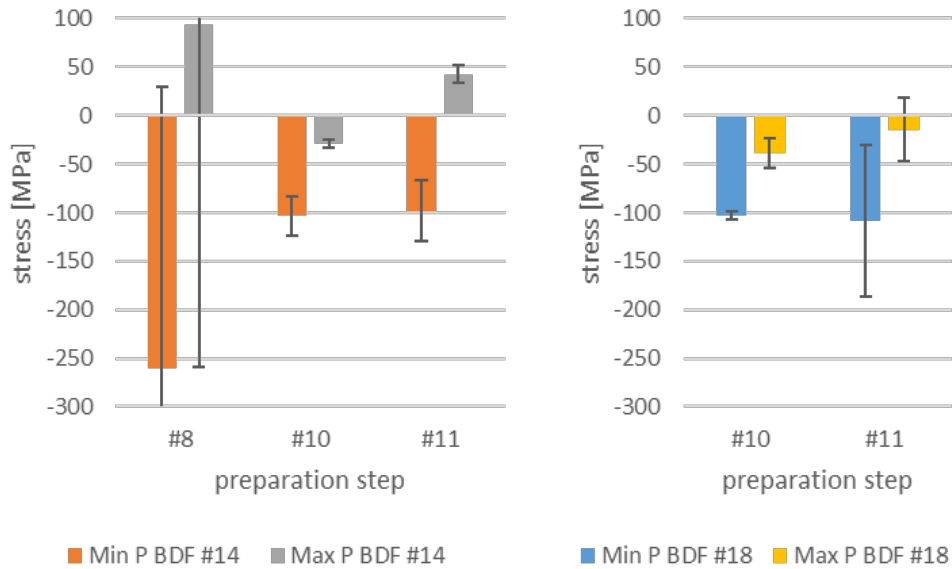


Figure 4.22: Recorded strain from DIC tracking in the 3 in-plane directions. In ring-core analysis, X direction is considered parallel to the cut edge and Y direction is considered orthogonal to the Y positive with the depth in the clad. SEM images of the surface before milling (0), and after 1,20 and 40 corresponding to the indicated relative milling depth h/h_{fin} of 0,0.5 and 1.



(a)

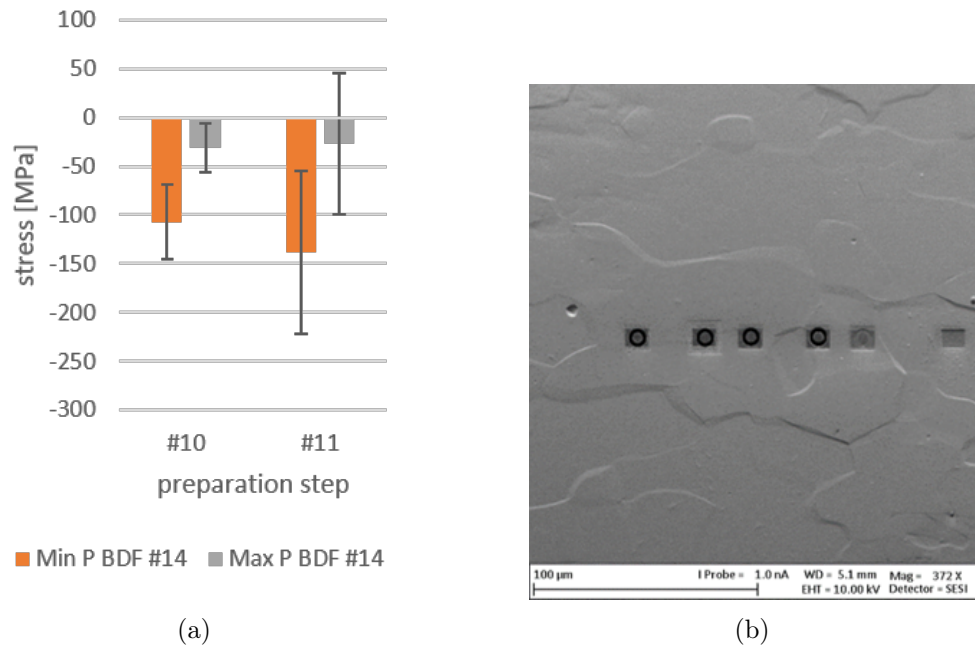
Prep. Step	Min P [MPa]	Max P [MPa]	St dev Min P	St dev Max P	n meas
#8	-206.8	93	290.8	352.8	2(4)
#10	-103.5	-29.1	20.6	4.2	2(3)
#11	-98.3	42.6	101.7	71.9	4(6)
#10 and #11	-100.0	18.7	110.2	67.8	6(9)

(b)

Prep. Step	Min P [MPa]	Max P [MPa]	St dev Min P	St dev Max P	n meas
#10	-102.9	-38.4	3.8	15.2	2(4)
#11	-108.7	-14.6	78.4	32.7	3(4)
#10 and #11	-106.3	-24.1	60.9	29.5	5(8)

(c)

Figure 4.23: FIB-DIC analysis measurement of Min and Max principal stresses in the BDF prototype #14 (table 4.23b) and #18 (table 4.23b) at different stages of surface preparation. Preparation step in reference to table 4.3. Analysis performed on cross-section at $750 \mu\text{m}$ from the outer clad surface. "n meas" indicate how many times the measurement has been repeated. As an example, "2(4)" means 2 measurement out of 4 converged to a stable solution by DIC analysis.



Prep. Step	Min P	Max P	St dev	St dev	n meas
	[MPa]	[MPa]	Min P	Max P	
#10	-107.2	-31.1	38.4	25.5	4(8)
#11	-138.2	-27.0	83.5	72.6	3(5)
#10 and #11	-122.7	-29.0	66.8	54.5	7(13)

(c)

Figure 4.24: FIB-DIC analysis measurement of Min and Max principal stresses in the BDF prototype #14 on the clad external surface at different stages of preparation. Preparation step in reference to table 4.3. Analysis performed on top surface, at 20mm from the center point of the cylinder and 1 mm from the cross-section edge. "n meas" indicate how many times the measurement has been repeated. As an example, "2(4)" means 2 measurement out of 4 converged to a stable solution by DIC analysis. In figure (b) a low-magnification SEM image of the analyzed sample is shown.

4.3 Discussion

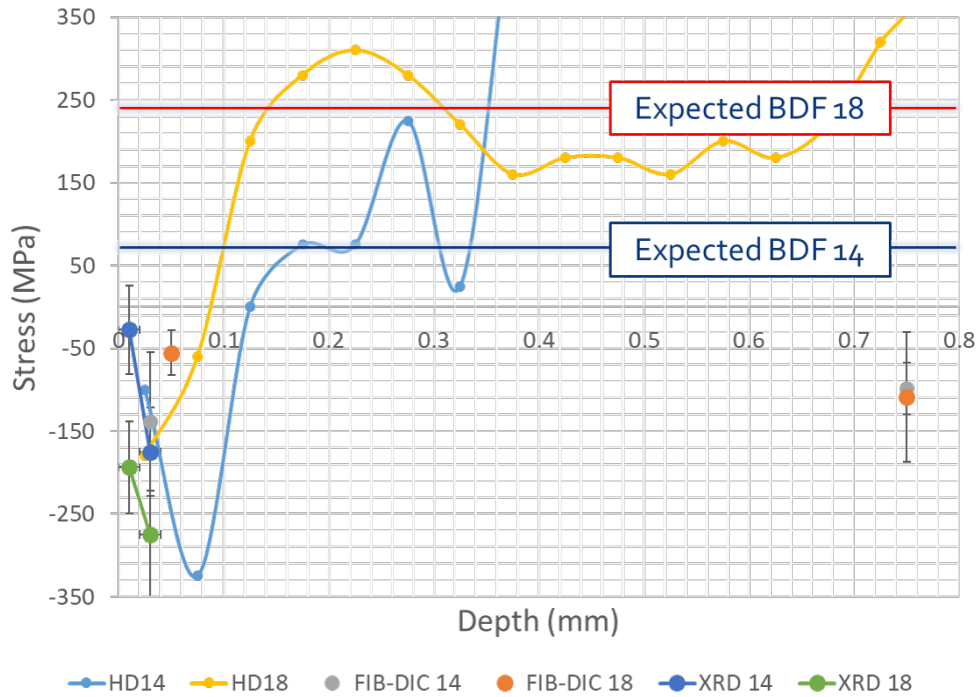


Figure 4.25: Table summarizing the expected residual stress due to the CTE mismatch and the residual stresses measurements obtained with the presented techniques.

The results of the residual stresses analysis on tantalum clad in the analyzed BDF target prototypes presented in figure 4.25.

The expected residual stresses in the clad due to the CTE mismatch is the order of 100 MPa tensile for the Ta-Mo combination and 250 MPa tensile for the Ta-W combination, as calculated by FEM simulation (section 4.2.1).

However, all the experimental analysis conducted indicate the presence of a compressive state in the order of -100 MPa in both the material combinations considered, uniform in the clad thickness.

Several hypothesis have been formulated to explain the observed phenomena:

- Residual stresses induced by sample preparation;
- Residual stresses due to turning operation after HIP;
- Bias due to the crystal orientation;
- Incomplete annealing during HIP.

Each hypothesis is discussed in the following sections.

4.3.1 Residual stresses induced by sample preparation

The measured compressive state could be an artifact induced by the mechanical preparation necessary to conduct the analysis. To test this hypothesis, measurements have been repeated after a prolonged stage of material removal by purely chemical action, as described in section 4.1.4.

The material removed by chemical polishing action did not cause any substantial alteration in the measured residual stresses, as shown in table 4.20b and 4.21b by XRD and in table 4.23b and 4.23c by FIB-DIC analysis.

It is therefore concluded that the surface preparation can not be considered the main cause for the recorded compressive state.

Compressive residual stresses, moreover, have been recorded also by the macroscopic hole drilling prior to any surface preparation further support the hypothesis that the compressive state has not been induced by the sample preparation.

4.3.2 Residual stresses due to turning operation after HIP

A second cause for the measured compressive stresses could be the turning operation performed by HIP PM Volker after the HIP process, as detailed in section 4.1.2.

The chemical attack performed during sample preparation revealed the presence of turning marks in the microstructure of the material, as shown in figure 4.26.

As introduced in section 1.2.3, machining operation such as turning can induce substantial residual stresses in the compressive region, and the induced effect can extend for several micrometers.

This machining effect could explain the compressive residual stress state present on the top surface of the clad (analyzed by XRD and hole drilling and FIB-DIC) but the effect is not believed to extend up to 750 μm below the machined surface (analyzed by FIB-DIC technique).

By directly comparing the FIB-DIC analysis performed on the core and surface of the clad (table 4.23b and 4.24c), the measured compressive residual stress showed no substantial variation (within the standard deviation of the measurements).

As the machining effect is expected to be localized close to the machined surface, the absence of a substantial variation in the measured residual stresses between the machined surface and the core of the clad material allow to exclude the turning as main cause of the measured residual stresses.

4.3.3 Incomplete annealing during HIP

As mentioned in section 4.1.2, during HIP process the samples are subjected to temperature of 1200 °C for 3 h. As shown in figure 4.2 in section 4.1.1, the selected HIP temperature and hold time should therefore be sufficient to guarantee complete annealing of the clad. However, the data found in literature does not take into account the high pressure conditions seen by the sample during HIP and other factors that might influence the annealing mechanism.

After the HIP process a fully recrystallized structure was expected. However, as can be seen in figure 4.27, the chemical attack revealed a strong difference in grain size between the center and the edges of the prototypes.

If complete stress relieve is not reached during the dwell time during HIP process, the measured compressive stresses could be originated for an earlier production stage.

This hypothesis could be tested in future by measuring the stress state of the assembly prior to HIP or by implementing an annealing stage after HIP in normal pressure conditions.

4.3.4 Artifact due to the crystal orientation

The chemical attack used as last polishing step etch preferentially one crystallographic orientation, making ring-core milling and DIC analysis easier on grains with that specific orientation. Tantalum is an isotropic material, and no major effect of grain orientation on the residual stresses is expected. However the possible influence of grain orientation in residual stresses have been checked.

Electron Backscatter Diffraction (EBSD) analysis has been performed on one of the samples, and FIB-DIC analysis has been performed on specific grain orientation.

EBSD mapping is presented in figure 4.28a, whereas an example of ring-cores milling in 111 and 101 crystal direction is presented in figure 4.28.

No trend emerged.

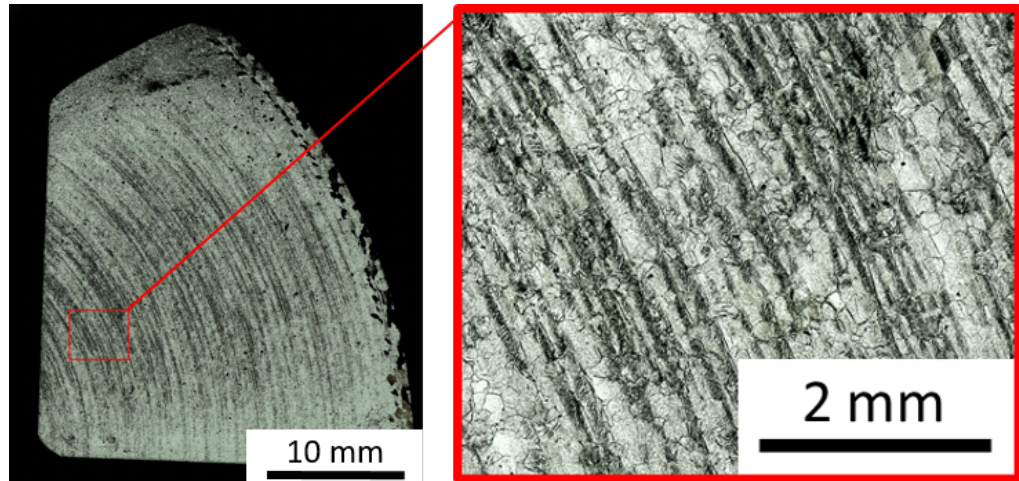


Figure 4.26: Optical microscope image of the turning marks revealed by the chemical attack in the sample #18.

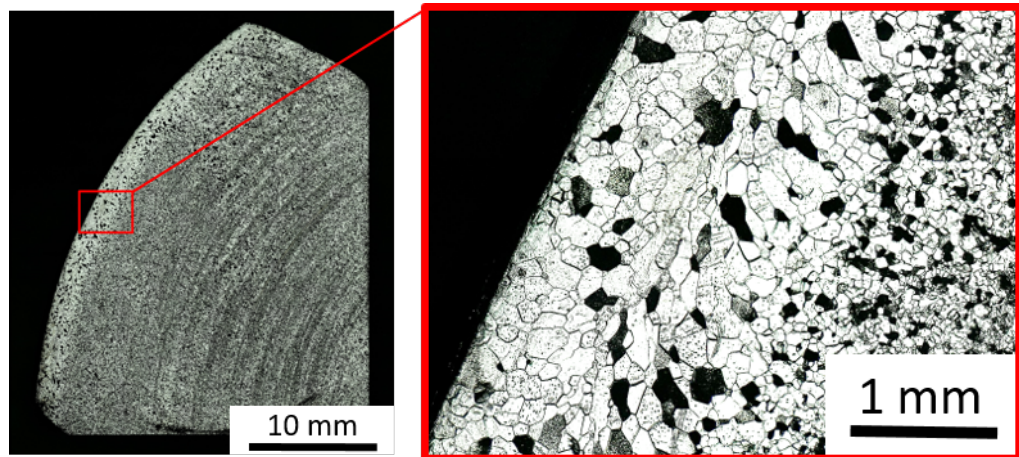
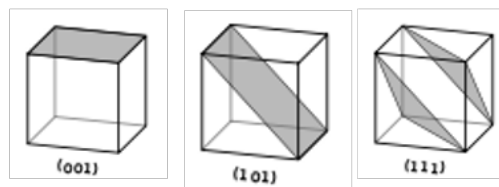
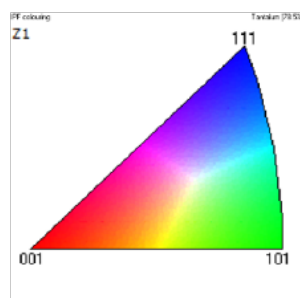
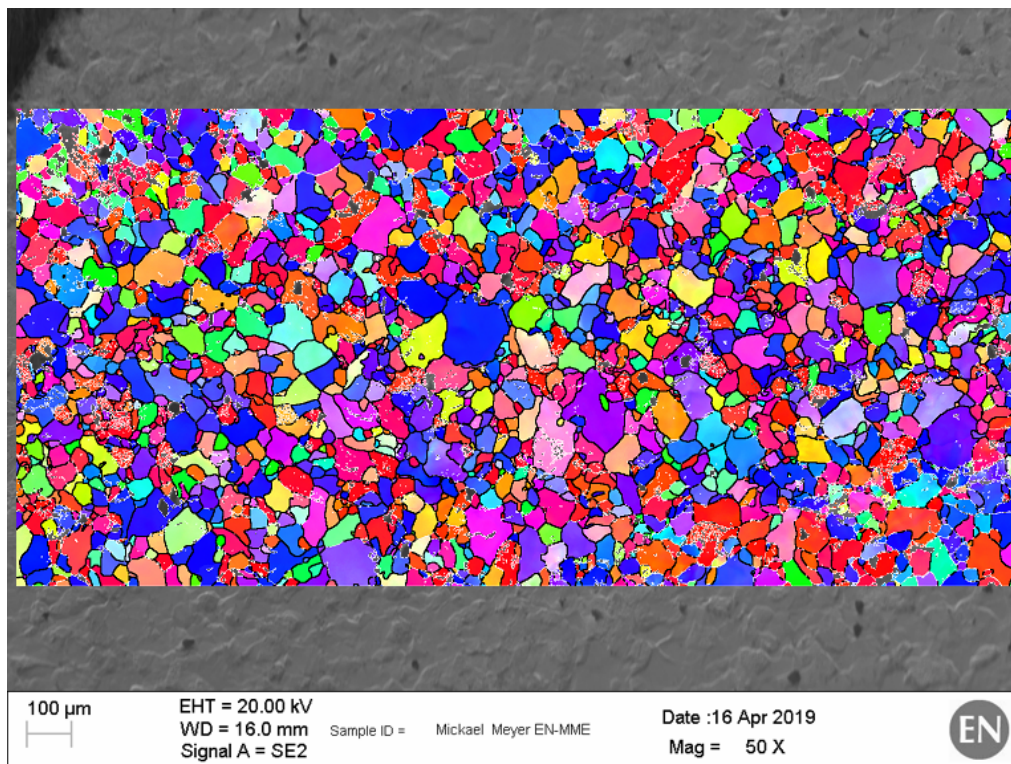
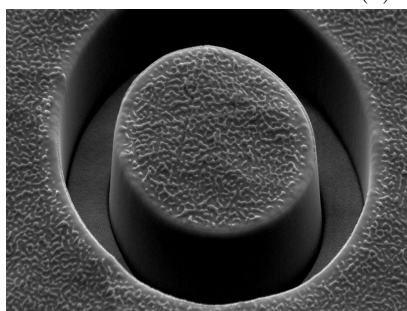


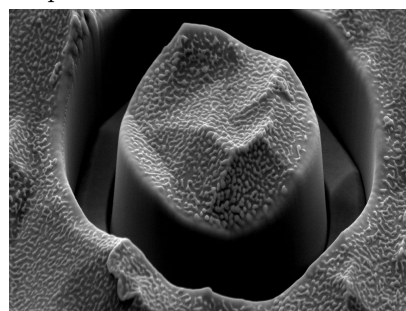
Figure 4.27: Optical microscope image of the not-uniform grain structure revealed by the chemical attack in the sample #14.



(a) EBSD map



(b) 111 orientation



(c) 101 orientation

Figure 4.28: EBSD analysis performed on the surface of the BDF prototype #14 (a) and example of ring-cores milled by FIB on Ta clad on grain in 111 (b) and 101 (c) orientation. The images (b) and (C) are taken after 50 milling steps.

Conclusions

Micro-scale residual stress analysis technique based on FIB milling of ring-core geometry was successfully applied for the first time at CERN labs for the analysis of residual stresses in cross-sections of bulk materials.

The developed methodology was compared against more conventional macroscopic hole-drilling strain gauge method (ASTM E837-13a [17]) and X-ray diffraction method (XRD).

In the first part of the project, residual stresses was evaluated in a sample of shot-peened aluminium sample.

In the second part of the project, the same techniques were applied to the residual stresses evaluation in two BDF target prototypes.

The results produced by the novel FIB-DIC methodology are well aligned with the ones produced by macroscopic blind-hole drilling and XRD, fully validating the FIB-DIC technique, data-processing, and methodology adopted.

The residual stresses analysis of aluminum showed no particular challenges, and the results obtained by the three techniques are within the recorded standard deviation.

The residual stresses analysis on the tantalum clad of the prototypes proved to be more challenging.

Ta is subject to severe work hardening, and reliable measurements were impossible to obtain by blind-hole drilling after the first 50 μm to 100 μm .

Due to the high-density of Ta, XRD measurements of residual stresses are highly superficial ($\sim 1 \mu m$). As a consequence, the recorded standard deviation has been more than 3 times higher than ones recorded with the same equipment and methodology in the aluminium sample.

Nonetheless, the results obtained by both blind hole drilling and XRD showed comparable results to the new FIB-DIC approach when conducted close to the clad surface.

The applied residual stresses analysis techniques indicate the presence of a

compressive stress field in the order of 100 MPa, for both the material combinations and on the surface and at 750 μm of depth.

This result can not be explained as an effect of the CTE mismatch between core and clad material, for which a tensile state was expected in the order of ~ 100 MPa tensile for the Ta2.5W - TZM material combination and ~ 230 MPa tensile for the Ta-W combination.

Compressive residual stresses are cause of major concern, as they might negatively influence the fatigue life of the beam dump¹.

Several hypotheses were formulated and tested to explain the observed residual stress state such as residual stresses due to light machining operation after HIP process, residual stresses induced by sample preparation and bias due to material microstructure. However, none of them proved to fully explain the data collected.

The observed compressive state could also be caused by a pre-existing stress state that did not fully relieve during during HIP process: The adopted dwell time and temperature during HIP process has been chosen to guarantee complete annealing of the clad material. However, the effect of isostatic pressure on recrystallization phenomena is not well understood, and metallographic pictures the clads revealed a not-homogeneous grain structure.

To validate this latter hypothesis, analysis of the residual stresses of the prototypes prior to HIP process is needed.

For the future, the adoption of an annealing step after machining operation could relieve the observed compressive state.

The inclusion during HIP cycle of a witness specimen constituted by an asymmetric clad strip of the material combination of interest is also advised, as it could allow a precise measurement of the residual stresses generated during HIP process by measuring the resulting deflection.

In conclusion, the FIB-DIC methodology has been successfully validated for residual stresses analysis at the micro-scale in aluminum and tantalum materials. The developed know how will remain in the CERN-MME lab, adding the FIB-DIC technique to the analysis that can be performed by the metallurgy team.

The application of FIB-DCI, XRD and blind-hole drilling indicate the presence of a compressive stress field in the BDF target prototypes that can not be explained by the CTE mismatch between the joined materials. The origin of the measured stresses is unclear and need to be further investigated as it might cause premature failure of the component.

¹the thermo-mechanical stresses generated by the beam impact are also in the compressive regime

Bibliography

- [1] “The nobel prize in physics 2013,” Accessed in 12/2018, available at: <https://www.nobelprize.org/prizes/physics/2013/summary/>.
- [2] E. Cartlidge, “Cern gives thumbs up to new sterile-neutrino detector,” *physicsworld*, 2016, visited in 12/2018. Available at: <https://physicsworld.com/a/cern-gives-thumbs-up-to-new-sterile-neutrino-detector/>.
- [3] CERN, “Engineering department - materials and metrology group,” Accessed in 12/2018, available at: <http://en.web.cern.ch/en-mme-group>.
- [4] M. Anelli *et al.*, “A facility to search for hidden particles (ship) at the cern sps,” *CERN Scientific Committee Paper*, no. 016, 2015.
- [5] M. Calviani, “Engineering challenges for beam dump facility,” 2017, notes for CERN NTNU Workshop.
- [6] CERN, “Ship - search for hidden particles,” Accessed in 12/2018, available at: <https://ship.web.cern.ch/ship/>.
- [7] J. Busom, “Beam dump facility production target design,” 2019, preprint not yet published.
- [8] L. Sola, M. Calviani, P. Avigni *et al.*, “Design of a high power production target for the beam dump facility at cern,” *physics.ins-det*, 2019.
- [9] M. Calviani *et al.*, “Conceptual design of the SHiP Target and Target Complex,” 2015, available at: <https://edms.cern.ch/document/1513294/1.0>.
- [10] D. Olson *et al.*, *ASM handbook: Welding, brazing, and soldering*. ASM International, 1993.
- [11] P. J. Withers and H. K. Bhadeshia, “Overview: Residual stress part 1 – measurement techniques,” *Materials Today: Proceedings*, vol. 17, pp. 355–365, 2001.
- [12] J. Lord, D. Cox, A. Ratzke *et al.*, “A good practice guide for measuring residual stresses using fib-dic,” *Good Practice Guide (GPG) by National Physical Laboratory (NPL)*, no. 143, 2018.
- [13] P. J. Withers and H. K. Bhadeshia, “Residual stress part 2 – nature and origins,” *Materials Today: Proceedings*, vol. 17, pp. 355–365, 2001.

- [14] T. Kostilnik, "Shot peening," *ASM Handbook, Surface Engineering*, vol. 5, pp. 126–135, 1994.
- [15] D. Yang, Z. Liu, X. Ren, and P. Zhuang, "Hybrid modeling with finite element and statistical methods for residual stress prediction in peripheral milling of titanium alloy Ti-6Al-4V," *International Journal of Mechanical Sciences*, vol. 2016, no. 108–109, pp. 29–38, 2016.
- [16] T. Gurova, J. R. Teodósio, J. M. A. Rebello, and V. Monin, "Model for the variation of the residual stress state during plastic deformation under uniaxial tension," *The Journal of Strain Analysis for Engineering Design*, vol. 33, no. 5, pp. 367–372, 1998.
- [17] "Standard test method for determining residual stresses by the hole-drilling strain-gage method, designation: E0837-13a," *Book of Standards*, vol. 03.01, 2013.
- [18] G. S. Schajer, "Measurement of non-uniform residual stresses using the hole-drilling method. part i—stress calculation procedures," *Journal of Engineering Materials and Technology*, vol. 110, no. 4, pp. 338–343, 1988.
- [19] Wikipedia, "Bragg's law," Accessed in 05/2019, available at: https://en.wikipedia.org/wiki/Bragg%27s_law.
- [20] S. Keil, "Experimental determination of residual stresses with the ring-core method and an on-line measuring system," *Exp Techniques*, vol. 16, pp. 17–24, 1992.
- [21] A. M. Korsunsky, M. Sebastiani, and E. Bemporad, "Focused ion beam ring drilling for residual stress evaluation," *Materials Letters*, vol. 66, no. 22, pp. 1961–1963, 2009.
- [22] M. Calviani, M. Battistin, R. Betemps *et al.*, "An introduction to the conceptual design of the ship facility production target and of the associated target complex," *SHiP Technical Proposal Annex*, no. 1513294, 2015.
- [23] D. Wilcox, P. Loveridge, T. Davenne, L. Jones, and D. Jenkins, "Stress levels and failure modes of tantalum-clad tungsten targets at isis," *Materials Today: Proceedings*, vol. 2, no. 2, pp. S267–S273, 2015.
- [24] Y. Ma, S. Y. Zhang, D. Jenkins, and S. Kabra, "An experiment using neutron diffraction to investigate residual strain distribution in a hot isostatic pressed (hipped) target plate," *Materials Today: Proceedings*, vol. 2, no. 2, pp. S267–S273, 2015.
- [25] "Pre-standardisation of incremental fib micro-milling for intrinsic stress evaluation at the sub-micron scale," Accessed in 05/2019, available at: <https://cordis.europa.eu/project/rcn/110690/factsheet/en>.

- [26] “Machining of tantalum - technical challenges,” Accessed in 05/2019, available at: <https://x-medics.com/technical-challenges-of-machining-tantalum/>.
- [27] “Standard test method for verifying the alignment of x-ray diffraction instrumentation for residual stress measurement, designation: E915 10,” *ASTM Book of Standards*, 2011.
- [28] M. Fitzpatrick, A. Fry, P. Holdway *et al.*, “Determination of residual stresses by x-ray diffraction - issue 2,” *Measurement Good Practice guide*, no. 52, 2005.
- [29] J. B. Descarrega, “Gold sputter coater “edwards s150a” user manualguide to sample preparation, operation and basic maintenance,” *EMM – Procedures*, vol. 9, no. 1752138, 2017.
- [30] M. A. Sutton and W. Wolters, “Determination of displacement using an improved digital image correlation method,” *Image Vision Computing*, vol. 1, no. 3, pp. 133–139, 1983.
- [31] E. Salvati, T. Sui, S. Ying *et al.*, “On the accuracy of residual stress evaluation from focused ion beam dic (fib-dic) ring-core milling experiments,” *Proc ICNFA*, vol. 15, no. 256, 2014.
- [32] A. Korsunsky, M. Sebastiani, and E. Bemporad, “Residual stress evaluation at the micrometer scale: Analysis of thin coatings by fib milling and digital image correlation,” *Surface and Coatings Technology*, vol. 205, no. 7, pp. 2393–2403, 2010.
- [33] A. J. Lunt, E. Salvati, L. Ma *et al.*, “Full in-plane strain tensor analysis using the microscale ring-core fib milling and dic approach,” *Journal of the Mechanics and Physics of Solids*, vol. 94, pp. 47–67, 2016.
- [34] “Makeitfrom - 3003 (almn1cu, 3.0517, a93003) aluminum,” Accessed in 04/2019, available at: <https://www.makeitfrom.com/material-properties/3003-ALMn1Cu-3.0517-A93003-Aluminum>.
- [35] “metal supermarkets - aluminum 3003,” Accessed in 04/2019, available at: <https://www.metalsupermarkets.com/metals/aluminum/aluminum-3003/>.
- [36] S. I. Lestari, “Residual stress measurements of unblasted and sandblasted mild steel specimens using x-ray diffraction, strain-gage hole drilling, and electronic speckle pattern interferometry (espi) hole drilling methods,” *University of New Orleans, Dissertation and theses*, 2004.
- [37] W. Martienssen and H. Warlimont, *Springer handbook of condensed matter and materials data*. Springer, 2005.

- [38] MTDATA, “Calculated molibdenum-tantalum phase diagram,” Accessed in 05/2019, avilable at: <http://resource.npl.co.uk/mtdata/phdiagrams/mota.htm>.
- [39] MTDATA, “Calculated tantalum-tungsten phase diagram,” Accessed in 05/2019, avilable at: <http://resource.npl.co.uk/mtdata/phdiagrams/taw.htm>.
- [40] G. V. Voort, “Chemical and electrolytic polishing,” *ASM Handbook, Metallography and Microstructures*, vol. 9, pp. 281–293, 2004.
- [41] Wikipedia, “Hydrofluoric acid,” Accessed in 05/2019, avilable at: https://en.wikipedia.org/wiki/Hydrofluoric_acid.
- [42] M. Calviani, M. Casolino, R. Jacobsson, M. Lamont, S. Roesler, H. Vincke, and C. Ahdida, “A beam dump facility (bdf) at cern – the concept and a first radiological assessment,” 2017, notes for AccApp ’17 conference, Quebec, Canada.
- [43] F. Schmidt and H. R. Ogden, “The engineering properties of tantalum and tantalum alloys,” BATTELLE MEMORIAL INST COLUMBUS OH DEFENSE METALS INFORMATION CENTER, Tech. Rep., 1963.
- [44] “Ultra 76 tantalum for corrosive resistant applications,” 2017. [Online]. Available: https://www.hcstarck.com/ultra76_tantalum_alloy
- [45] A. M. Korsunsky, M. Sebastiani, and E. Bemporad, “Residual stress evaluation at the micrometer scale: Analysis of thin coatings by fib milling and digital image correlation,” *Surface and Coatings Technology*, vol. 205, no. 7, pp. 2393–2403, 2010.
- [46] A. J. Lunt and A. M. Korsunsky, “Intragranular residual stress evaluation using the semi-destructive fib-dic ring-core drilling method.” *Advanced Materials Research*, vol. 996, pp. 8–13, 2014.
- [47] E. Salvati, A. J. Lunt, T. Sui, and A. M. Korsunsky, “An investigation of residual stress gradient effects in fib-dic micro-ring-core analysis,” *Proceedings of the International MultiConference of Engineers and Computer Scientists*, vol. 2, 2015.
- [48] X. Song, K. B. Yeap, J. Zhu, J. Belnoue, M. Sebastiani, E. Bemporad, K. Y. Zeng, and A. M. Korsunsky, “Residual stress measurement in thin films using the semi-destructive ring-core drilling method using focused ion beam,” *Procedia Engineering*, vol. 10, pp. 2190–2195, 2011.
- [49] TAMUK, “Strain transformation and rosette gage theory,” Accessed in 12/2018, avilable at: http://users.tamuk.edu/kfldp00/MEIE_Peel_website/Courses/Meen5330/strain-gage-rosette-theory_GA_Tech.pdf.

- [50] A. J. G. Lunt, N. Baimpas, E. Salvati, I. P. Dolbnya, T. Sui, S. Ying, H. Zhang, A. K. Kleppe, J. Dluhoš, and A. M. Korsunsky, “A state-of-the-art review of micron-scale spatially resolved residual stress analysis by fib-dic ring-core milling and other techniques,” *The Journal of Strain Analysis for Engineering Design*, vol. 50, no. 7, pp. 426–444, 2015.
- [51] A. J. G. Lunt, “Focused ion beam cross sectional milling and microscale residual stress analysis of non-evaporable getter coatings,” 2018, cERN internal note.

Used acronyms

Infrastructure and organization:

CERN European Organization for Nuclear Research (Conseil Européen pour la Recherche Nucléaire)

EN Engineering department

MME Materials and Metrology section

STI Sources, Targets and Interactions section

SHiP Search for Hidden Particles

NDT Nondestructive Testing

BDF Beam Dump Facility

CDP Comprehensive Design Phase

Physics:

SM Standard Model

DM Dark Matter

BAU Baryon asymmetry

BSM Beyond the Standard Model

BOT Beam On Target

Accelerator complex:

PSB Proton Synchrotron Booster

PS Proton Synchrotron

SPS Super Proton Synchrotron

LHC Large Hadron Collider

Equipment, process and techniques:

FIB Focused Ion Beam

SEM Scanning Electron Microscope

DIC Digital Image Correlation

XRD X-Ray Diffraction

EBSD Electron Backscatter Diffraction

HIP Hot Isostatic Pressing

Material properties:

CTE Coefficient of Thermal Expansion

UTS Ultimate Tensile Strength

Notes on thermo-mecanical stresses in BDF

The target has been designed to absorb the high energies delivered by the SPS proton beam.

As can be seen in figure 1.6b, most of the power is adsorbed in the first TZM blocks and the target is segmented to have a constant energy delivered to each block.

The resulting temperature distribution during beam spillage is shown in figure 1.6a. The expected maximum temperature in the molybdenum alloy (TZM) was calculated to be 185 C and 160 C on the Ta cladding [42], as can be seen in figure 1.6c.

The shown temperature gradient is result of an optimization that involves the sweep of the beam on on a circular pattern during the pulse, to minimize the localized temperature buildup (beam dilution).

The temperatures reached in both core and cladding materials are around 0.1 T_m , therefore no allotropic transformations are expected.

However, change in material properties due to temperature needs to be taken into account.

The steep temperature difference between the beam impact area and the surrounding zone give rise to temperature-induced stresses that needs to be take into account.

Moreover, the BDF target will face approximately 10^6 beam pulses par year operation, and therefore the same number of thermal cycles. Mechanical stresses and fatigue pehenomenas are expected at the clad interface due to the CTE miss-match.

Finally, the Hot Isostatic Pressing (HIP) procedure adopted to join the tungsten cladding material with the molibdenum and vanadium core give rise to residual stresses also due to their different Coefficient of Thermal Expansion.

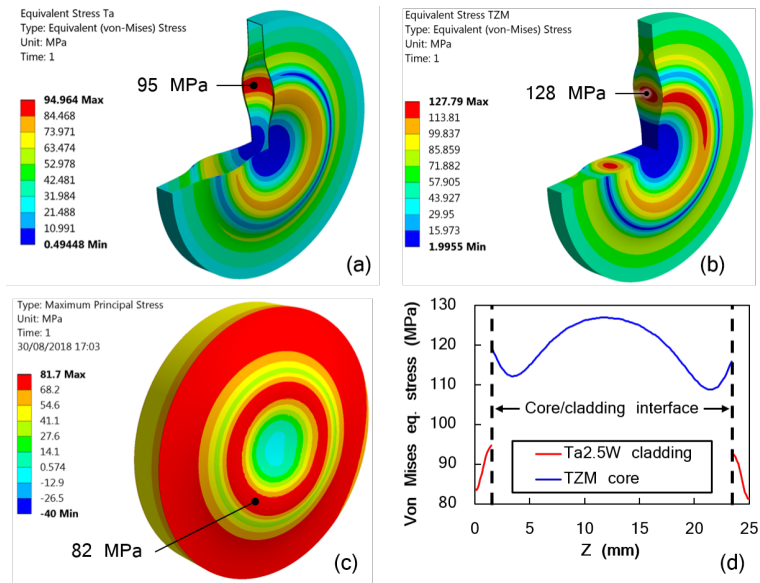


Figure B.1: Von Mises equivalent stress distribution after one beam pulse in the most loaded blocks for each target material: Block 4 for Ta2.5W (a) and TzM (b), Block 14 for W (c). Stress distribution in the longitudinal axis at the beam dilution position ($Y = 50$ mm) for block 4. [7]

Simulations revealed that in some areas of the assembly, temperatures-induced stresses can reach up to 100 MPa at 150°C . Since the yield stress of the unalloyed Ta is approximately 80 MPa at this temperature, the accumulation of cyclic plastic strain could lead to clad premature failure. To avoid the problem, a commercial Ta alloy strengthened with 2.5% of W has been utilized instead.

Ta2.5%W [43] features higher yield and tensile stress at high temperature, with values of 190 MPa and 290 MPa at 200°C [44].

FIB-DIC operator's manual

Dr. Alexander J. G. Lunt in the past years developed and refined a method based on Incremental Focused Ion Beam (FIB) milling of annular trenches combined with high resolution SEM imaging of a previously deposited marker pattern to assess the residual stresses in surfaces. [45, 46, 47, 48, 49, 50, 51]

C.0.1 Milling

The method consist in:

1. deposit a coating - gold works well — see "Electron microscopy and microscopy standard procedure n9 - gold sputter coater user maual"
2. texture the surface by fast ion milling (100-300 pA)
3. drill the trench with FIB

The SEM/FIB operation is at follows:

- Open Smart SEM (user/pw: XB540/XB540);
- Open Fib control;
- Open gun monitor;
- EHT on (emission)
- tilt sample to 54¹ degrees and apply tilt correction;
- Operations with smart fib:
 - Adjust contrast until image is sharp
 - Align FIB with SEM vertically adjusting Z, orizzontaly ajust with SEM beam shift.
 - ion gun settings: 30 KV, 300 pA, 1um steel setting²;

¹the beam angle is 2.6 degrees

²1um Si was first choice but not working

- Set milling region: size according to the stress region need to be evaluated (evaluated stresses in the pillar volume for 0.4D of thickness)³;
- milling movement: spiraling from external to internal diameter;
- 25 to 50 nm of material removed each pass, proceed until the bottom is not visible anymore:
- Save SEM image after each ion milling step with incremental number for DIC interpretation;
- set mouse recorder to mill and save image
- play macro until needed depth is reached⁴

C.0.2 DIC

The post post processing is done by Matlab software using the plugin “Digital Image Correlation and Tracking”, downloadable at <https://www.mathworks.com/matlabcentral/fileexchange/50994-digital-image-correlation-and-tracking>.

1. Copy images in same folder DIC
2. generate file list and process as follows (image C.1 and C.2 as reference):
 - large displacement needed for drift correction;
 - set about 50-100 markers for reference mainly in the area surrounding the trench (for drift correction) - size 20x20;
 - use ellipse tool to highlight the pillar area for fine measurement. Aim at outer edge and then set scale to 0.8 or 0.7 - grid size 10x10;
 - open stand deviation files
 - clean bad data
 - remove badly tracked marks following sequence in C.2 and screen instructions
 - generate output file by strain analysis/principal stains (mechanical properties of material from literature or other in-house mechanical test)

Among the various options, the most effective way to remove outliers proved to be the removal of markers relative to neighbours and the manual removal of outliers from the expected displacement field.

³geometry tested in test run: 2.5um inner r, 4um outer R

⁴about 40x for trial

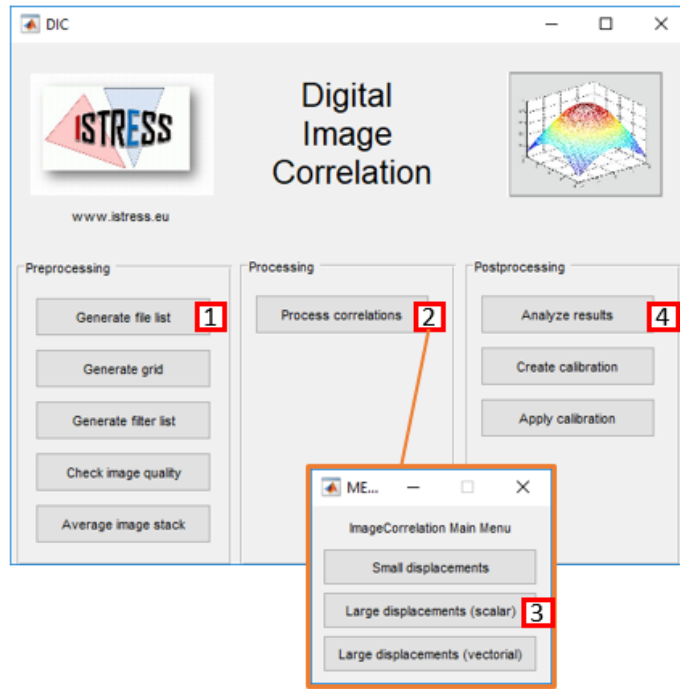


Figure C.1: DIC analysis sequence

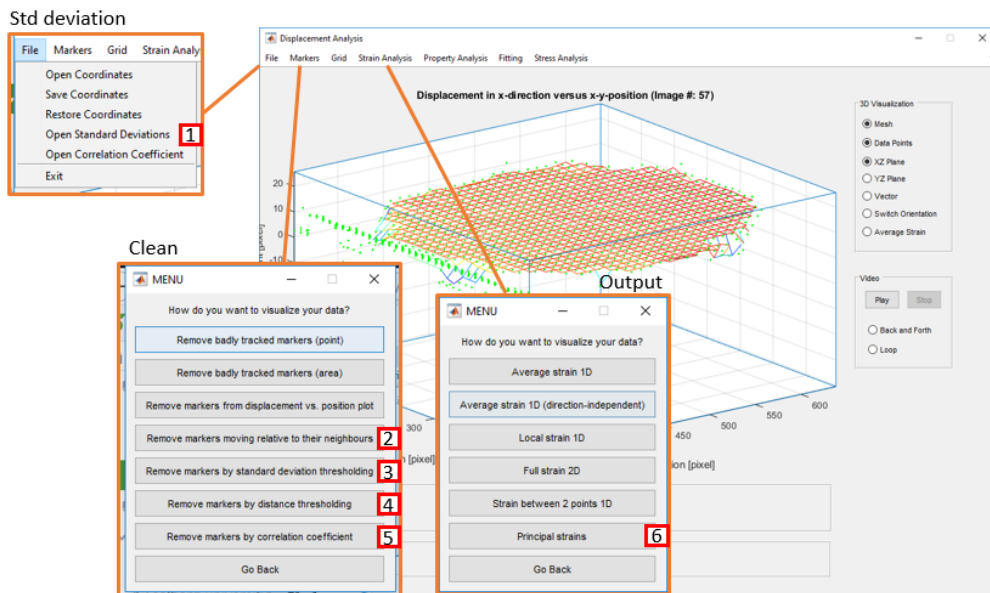


Figure C.2: DIC post-processing sequence

In the markers moving relative to neighbours, the displacement field of every marker is compared with its neighbors.

For ring-core milling geometry, the expected displacement field is uniform. Anomalies are easy to spot and remove.

Outliers can also be removed manually from the displacement.

Care must be taken to ensure that the initial fit is representative of the observed behaviour.

In the case of ring-core milling geometry, as the expected displacement is linear, obvious outliers can be safely removed from the displacement field.

Hardness measurements of Al, Ta and Ta2.5W materials

In an effort to explain the difficulties encountered in applying the macroscopic hole drilling technique on the Ta clad samples, Vickers hardness test have been performed on the surface of the Ta clad samples and in the cross-section and surface of the shot-peened aluminum sample.

Results are summarized in the following picture, and show how the hardness of the analyzed materials is comparable.

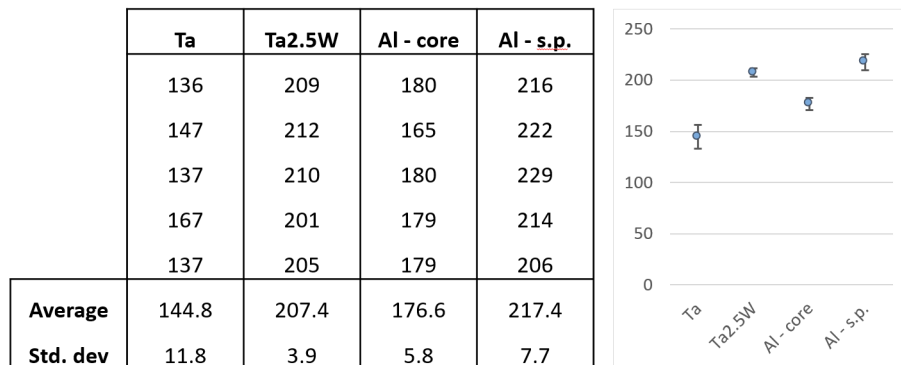


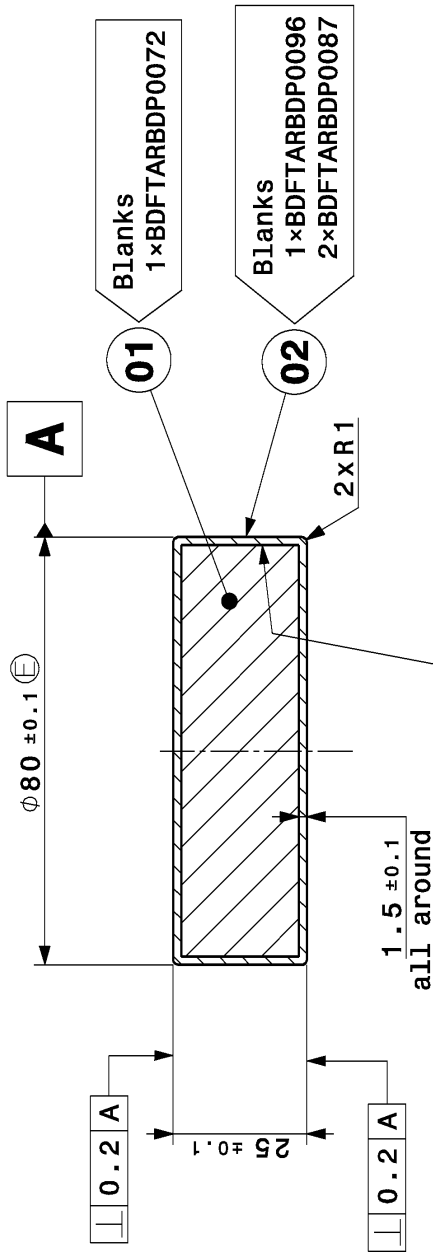
Figure D.1: Experimental results of hardness test performed with WOLPERT 402 MVD micro-hardness tester Vickers indenter and an applied force of 10N

BDF targhet prototypes technical drawings

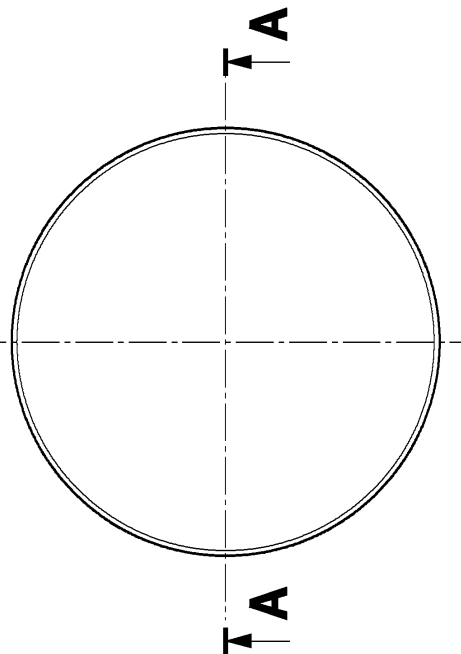
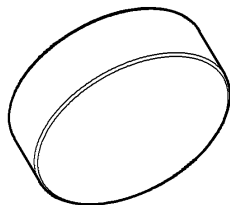
Technical drawing as supplied to the contractor of the BDF targhet prototypes are provided.

- **BDF TARBDP0039-AA**, corresponding to the BDF #14 (Ta2.5W-clad TZM)
- **BDF TARBDP0041-AA**, corresponding to the BDF #18 (Ta-clad W)

A-A



adjust the \emptyset ext. of the blank Disk (01) for a gap(\emptyset) included between 100 μ and 200 μ before insertion and HIPing



Mass: 1.5 kg

UNLESS OTHERWISE MENTIONED, APPLICABLE ISO GPS STANDARDS ARE THOSE PRIOR TO 2010-08-01 REGARDLESS OF THE DRAWING DATE

CLAD	Tantalum-Tungsten 2.5%	ST0902258	REF. CERN
1	CHEMISE (Ta-2.5W)	ST0902258	
1	DISK DISQUE TZM Molybdenum	ST0902257	
QUA	DESCRIPTION	POS	MAT.
ENS/ASS	S. ENS/S.ASS		

ISO 2768-mK	Ra 1.6	ISO 13715	-0.3	+0.3
Target Prototype for Dump Facility				
SCALE				
BDF T6 TARGET TEST				
BLOCK TZM 2-3-4-5-6-7				
BLOC TZM 2-3-4-5-6-7				
1:1				

DES/DRA.	L. ZUCCALLI	2017-10-25
CONTROLLED	B. RIFFAUD	2018-01-19
RELEASED	M. CALVIANT	2018-01-19
APPROVED		
CAD Document Number ST0902254_02		
REPLACES		

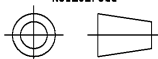
RELEASED BY	FOR	IND.
PROJECT ENGINEER	PRODUCTION	3
BDF TARBDP0039		3

IND.	DATE	NOM/NAME	ZONE	added notes
A	2018-01-16	L. ZUCCALLI		MODIFICATION



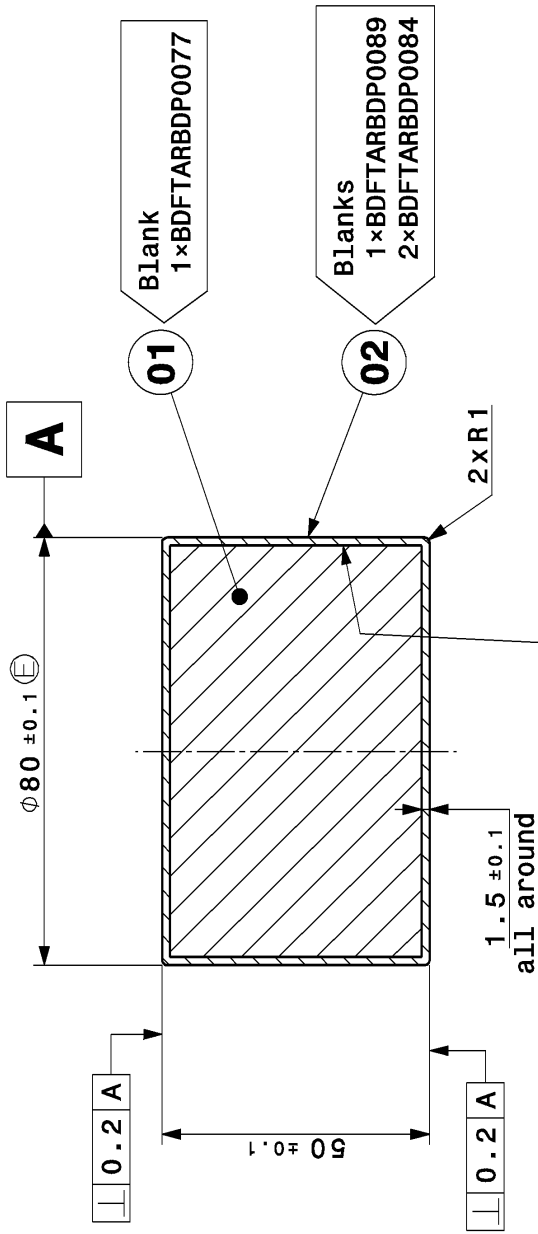
ORGANISATION EUROPEENNE POUR LA RECHERCHE NUCLEAIRE
EUROPEAN ORGANIZATION FOR NUCLEAR RESEARCH
GENEVE

This drawing may not be used for commercial purposes without written authorization
ce dessin ne peut être utilisé à des fins commerciales sans autorisation écrite

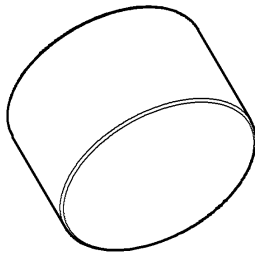


DESSIN, RUGOSITE, TOLERANCES SELON NORMES ISO
DRAWING, RUGOSITY, TOLERANCES ACCORDING TO ISO STANDARDS

A-A



adjust the \emptyset ext. of the blank Disk (01) for a gap(\emptyset) included between 100 μ and 200 μ before insertion and HIPing

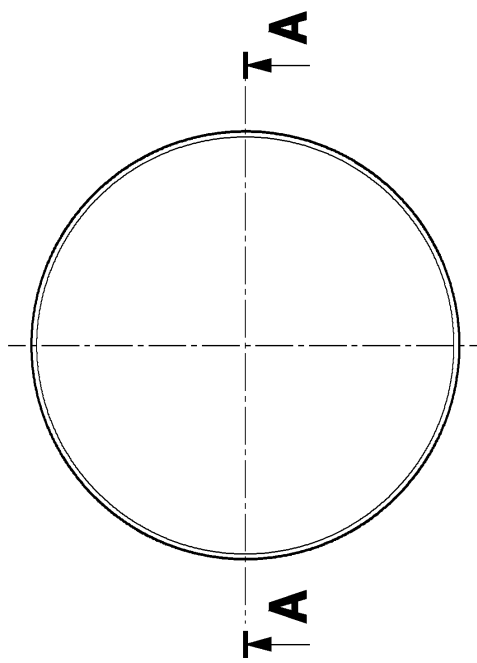


Mass: 3.8 kg

UNLESS OTHERWISE MENTIONED, APPLICABLE ISO GPS STANDARDS ARE THOSE PRIOR TO 2010-08-01 REGARDLESS OF THE DRAWING DATE

CLAD	Tantalum	ST0902307			
1	Tantalum	ST0902307			
2	Tantalum	ST0902307			
DISK	Tungsten				
1	Tungsten	ST0902308			
DISQUE					
1					
QUA	DESCRIPTION	POS	MAT.	OBSERVATIONS	REF. CERN
ENS/ASS	S. ENS/S.ASS				

ISO 2768-mK	ISO 13715	-0.3	+0.3	()
Target Prototype for Dump Facility				
SCALE				
BDF T6 TARGET TEST				
BLOCK TUNGSTEN 14				
1:1				
BLOC TUNGSTEN 14				
DES/DRA. L. ZUCCALLI 2017-10-26				
CONTROLLED B. RIFFAUD 2018-01-19				
RELEASED M. CALVIANT 2018-01-19				
APPROVED				
CAD Document Number ST0902306_02				
REPLACES				

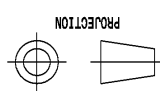


ISO 2768-mK	ISO 13715	-0.3	+0.3	()
Target Prototype for Dump Facility				
SCALE				
BDF T6 TARGET TEST				
BLOCK TUNGSTEN 14				
1:1				
BLOC TUNGSTEN 14				
DES/DRA. L. ZUCCALLI 2017-10-26				
CONTROLLED B. RIFFAUD 2018-01-19				
RELEASED M. CALVIANT 2018-01-19				
APPROVED				
CAD Document Number ST0902306_02				
REPLACES				

IND.	A	DATE	2018-01-16	NOM/NAME	L. ZUCCALLI	ZONE		added notes	
								MODIFICATION	

IND.	3	SIZE	IND.	A
------	---	------	------	---

DESSIN, RUGOSITE, TOLERANCES SELON NORMES ISO
DRAWING, RUGOSITY, TOLERANCES ACCORDING TO ISO STANDARDS



ORGANISATION EUROPEENNE POUR LA RECHERCHE NUCLEAIRE
EUROPEAN ORGANIZATION FOR NUCLEAR RESEARCH
GENEVE
Ce dessin ne peut être utilisé à des fins commerciales sans autorisation écrite
This drawing may not be used for commercial purposes without written authorization